

# Human Whole-Body Dynamics Estimation for Enhancing Physical Human-Robot Interaction

Claudia Latella



ISTITUTO ITALIANO  
DI TECNOLOGIA

Dibris

Dipartimento  
di Informatica,  
Bioingegneria,  
Robotica e  
Ingegneria dei Sistemi

Supervisor: Dott. Francesco Nori

Fondazione Istituto Italiano di Tecnologia  
Dynamic Interaction Control Lab  
Genova, Italy

Dipartimento di Informatica, Bioingegneria, Robotica e Ingegneria dei  
Sistemi, Università di Genova



## Abstract

In the last two decades the scientific community has shown a great interest in understanding and shaping the interaction mechanisms between humans and robots. The *interaction* implies *communication* between two dyadic agents and, if the type of interaction is ‘physical’, the communication is represented by the set of forces exchanged during the interaction. Within this context, the role of quantifying these forces becomes of pivotal importance for understanding the interaction mechanisms. At the current scientific stage, classical robots are built to act *for* humans, but the scientific demand is going towards the direction of robots that will have to collaborate *with* humans. This will be possible by providing the robots with sufficient pieces of information of the agent they are interacting with (i.e., kinematic and dynamic model of the human). In a modern age where humans need the help of robots – apparently in an opposite trend – this thesis attempts to answer the following questions: “*Do robots need humans? Should robots know their human partners?*”. A tentative answer is provided here in the form of a novel framework for the simultaneous human whole-body motion tracking and dynamics estimation, in a real-time scenario. The framework encompasses a set of body-mounted sensors and a probabilistic algorithm able of estimating physical quantities that in humans are not directly measurable (i.e., torques and internal forces). This thesis is mainly focussed on the paramount role in retrieving the human dynamics estimation but straightforwardly it leaves the door open to the next development step: passing the human dynamics feedback to the robot controllers. This step will enable the robot with the capability to observe and understand the human partner by generating an enhanced (intentional) interaction.



# Acknowledgements

First of all, I would like to thank Francesco (Nori) for the opportunity he gave me three years ago: they have been, professionally and personally speaking, very beautiful years. To Francesco (Romans) for helping, supporting and tolerating me and to Daniele for being a great friend of mine before that of a colleague. To Silvio for his constant help and for what he has developed throughout these years: he gave us a solid foundation on which developing our work.

To the new An.Dy group. To Luca (Tagliapietra), he was the last one to arrive but he is already a companion of a thousand misadventures (or 'disagi', as we prefer to call them). To Yeshi, our new control man, for his important contribution to the human-in-the-loop stuff! And to Diego, our technician. But above all, to Marta and Maria, our M&M's: even if they are not currently part of our group, they collaborated in the past to build what the human research line is now. For me, they will be always An.Dy girls!

To all my lab colleagues (of today and of the past): Gabry, Stefano, Aiko, Nuno, Luca (Fiorio), Jorh, Joan, Marie, Francisco, La Strama, Alessia, Boiello e Matte, and to the new comers! To the big purchases with Marianna and Angelica Rosboff.

To Dana for the opportunity she gave me to visit her labs in Waterloo and to meet the Waterloo guys. To those of them that helped me with the setup (Jonathan, Vlad and Kevin) and to those ones that have been subject to the experiments.

To my loved ones for rooting for me: to my parents, my sister Katia and his boyfriend Silvio, my aunt Clelia, my husband's family (Marianrosa, Pierluigi, Giacomo, Sara and Filippo) for their support and all my friends.

And to Paolo, if I am here today I owe it to him, to that extreme fortitude to which he hanged up in a moment of extreme pain and difficulty. Thanks for giving me this, too!

... And to those (non-scientific) filters that allow me to move forward!



# Preliminaries

The following lists represent reference tables for the entire manuscript.

## Nomenclature

---

$p$	Scalar (non-bold small letter)
$\mathbf{p}$	Vector (bold small letter)
$\mathbf{A}$	Matrix, tensor (bold capital letter)
$(\cdot)^T$	Transpose matrix
$\times$	Cross product for 6D motion vectors
$\times^*$	(Dual) cross product for 6D force vectors
$ \cdot $	Matrix determinant
$\mathbf{S}(\cdot)$	Skew-symmetric matrix
$\mathbf{A}$	Matrix, tensor (bold capital letter)
$\mathcal{A}$	Coordinate reference frame (calligraphic letter)
$O_{\mathcal{A}}$	Origin of coordinate frame $\mathcal{A}$
${}^{\mathcal{A}}\mathbf{p}$	Vector expressed in frame $\mathcal{A}$
${}^{\mathcal{A}}(\cdot)_{\mathcal{B}}$	Transformation operator from frame $\mathcal{B}$ to frame $\mathcal{A}$
$\dot{\mathbf{p}}$	First-order time derivative
$\ddot{\mathbf{p}}$	Second-order time derivative
$\underline{\mathbf{p}}$	Spatial vector (underlined bold small letter)
$\mathbf{I}$	Inertia tensor
$\mathbf{J}$	Jacobian matrix
$\bar{\mathbf{S}}$	Motion freedom subspace
$\sum$	Summation operator
$(\cdot)^\dagger$	Pseudoinverse of a matrix
$(\cdot)^{-1}$	Inverse matrix
$rank(\cdot)$	Rank of a matrix
$\mathcal{N}$	Normal distribution
$E[\cdot]$	Expected value
$\mu$	Mean

$\Sigma, cov[\cdot]$	Covariance matrix
$\arg \max(\cdot)$	Maximizing argument
$\arg \min(\cdot)$	Minimizing argument
$diag(\cdot)$	Diagonal matrix
$\ \cdot\ $	Norm
$Tr$	Trace

## Abbreviations and Acronyms

---

HRI	Human-Robot Interaction
pHRI	Physical Human-Robot Interaction
w.r.t.	With respect to
2D	Two-dimensional
DoF	Degree of Freedom
ID	Inverse Dynamics
IMU	Inertial Measurement Unit
3D	Three-dimensional
RGB	Red-Green-Blue
6D	Six-dimensional
CoM	Centre of Mass
RNEA	Recursive Newton-Euler Algorithm
URDF	Unified Robot Description Format
fb	Fixed base
PDF	Probability Density Function
MAP	Maximum-A-Posteriori
MSE	Mean Square Error
MMSE	Minimum Mean Square Error
LMMSE	Linear Minimum Mean Square Error
GLS	Generalized Least-Squares
IK	Inverse Kinematics
F/T	Force/Torque
RMSE	Root Mean Square Error
API	Application Programming Interface
YARP	Yet Another Robot Platform
EM	Expectation-Maximization
EKF	Extended Kalman Filter

# Contents

<b>1</b>	<b>Introduction</b>	<b>1</b>
1.1	Rationale . . . . .	1
1.2	State of the Art . . . . .	4
1.2.1	Human Body Dynamics Estimation . . . . .	5
1.2.2	Sensors Technology . . . . .	6
1.2.3	Physical Human-Robot Interaction . . . . .	7
1.3	Contribution . . . . .	8
1.3.1	Publications . . . . .	9
1.4	Technological Outcome . . . . .	9
1.5	Thesis Outline . . . . .	10
<b>2</b>	<b>Rigid Multi-Body System</b>	<b>11</b>
2.1	Notation . . . . .	11
2.2	The Non-Deformability Assumption . . . . .	12
2.3	Rigid Body Kinematics . . . . .	12
2.3.1	Pose Representation . . . . .	13
2.3.2	The Derivative of a Rotation Matrix . . . . .	14
2.3.3	6D Motion Vectors . . . . .	16
2.4	Rigid Body Dynamics . . . . .	17
2.4.1	6D Force Vectors . . . . .	17
2.4.2	The Newton-Euler Equations of Motion . . . . .	18
2.5	Rigid Multi-Body System . . . . .	19
2.5.1	Modelling . . . . .	19
2.5.2	Lagrangian Representation . . . . .	19
2.5.3	Newton-Euler Representation . . . . .	21
<b>3</b>	<b>Human Whole-Body Modelling</b>	<b>23</b>
3.1	Human Whole-Body Modelling . . . . .	23
3.1.1	Inertial Properties Modelling . . . . .	24

3.1.2	Link Modelling . . . . .	26
3.1.3	Joint Modelling . . . . .	29
3.2	The Human URDF Model . . . . .	32
3.2.1	Sensor Pose Estimation . . . . .	32
<b>4</b>	<b>The Human Dynamics Estimation Problem: a Probabilistic Solution</b>	<b>37</b>
4.1	The System Constraints Formulation . . . . .	38
4.1.1	Considerations on the Representation . . . . .	40
4.2	The Measurements Equation . . . . .	41
4.2.1	An Illustrative Example . . . . .	41
4.3	The Estimation Problem Formulation . . . . .	44
4.4	Probabilistic Preliminaries . . . . .	44
4.5	The Maximum-A-Posteriori Solution . . . . .	46
4.5.1	The Cholesky Decomposition . . . . .	48
4.6	Considerations on the Estimator Choice . . . . .	50
4.6.1	Linear Estimator for Jointly Gaussian Vectors . . . . .	50
4.6.2	Linear Estimator for Linear Regressors . . . . .	51
4.6.3	Generalized Least-Squares Estimator . . . . .	53
4.6.4	The MAP Estimator . . . . .	54
<b>5</b>	<b>Software Implementation and Algorithm Validation</b>	<b>55</b>
5.1	MAP Software Implementation . . . . .	55
5.2	Experimental Sensor Setup . . . . .	58
5.2.1	Motion Capture . . . . .	58
5.2.2	Ground Reaction Forces Tracking . . . . .	59
5.3	Data Analysis . . . . .	60
5.3.1	<i>ftShoes</i> Validation . . . . .	61
5.3.2	Estimation of Human Variables . . . . .	65
5.3.3	Incremental Sensor Fusion Analysis . . . . .	78
5.4	An Experiment with the iCub . . . . .	80
5.4.1	MAP vs. OpenSim Dynamics Estimation . . . . .	86
<b>6</b>	<b>Towards the Real-Time Human Dynamics Estimation</b>	<b>89</b>
6.1	YARP Middleware for the Human Framework . . . . .	89
6.2	Towards the Online Estimation . . . . .	91
<b>7</b>	<b>The <i>human-in-the-loop</i> Concept</b>	<b>95</b>
7.1	Coupled System Modelling . . . . .	96
7.2	Rigid Constraints . . . . .	96

<b>8</b>	<b>Conclusions and Forthcoming Works</b>	<b>101</b>
8.1	Discussion . . . . .	102
<b>A</b>	<b>Top-Down and Bottom-Up Approaches</b>	<b>107</b>
<b>B</b>	<b>URDF Human Modelling</b>	<b>111</b>
B.1	The Non-Standard URDF Extension . . . . .	118
<b>C</b>	<b>Offline Inverse Kinematics Computation</b>	<b>121</b>
<b>D</b>	<b>Simultaneous Human Dynamics and State Estimation</b>	<b>125</b>



# Chapter 1

## Introduction

*Any sufficiently advanced technology is indistinguishable from magic.*

Arthur C. Clarke

### 1.1 Rationale

Human-Robot Interaction (HRI) is arousing a remarkable interest among the scientific community. The field, emerged in the early years of 2000, addresses the design, the understanding and the evaluation of robotic systems which involve humans and robots interacting through cooperation.

The ever-growing interest of the scientific community in studying coupled human-robot systems is visible in the thriving production of papers related to HRI topics in the last two decades. Figure 1.1 shows the number of papers obtained by searching on the IEEE Explore website the keyword ‘human-robot’ concerning the two main conferences of robotics: IEEE/RSJ International Conference on Intelligent Robots and Systems (IROS) and IEEE International Conference on Robotics and Automation (ICRA). Despite the existence of several fluctuations over the years, the trend has definitely increased straddling the two centuries (see also [Demircan et al., 2015]).

The HRI problem is well-defined as the problem “*to understand and shape the interactions between one or more humans and one or more robots. [...] evaluating the capabilities of humans and robots, and designing the technologies and training that produce desirable interactions are essential components of HRI. Such work is inherently interdisciplinary in nature, requiring contributions from cognitive science, linguistics, and psychology; from engineering, mathematics, and computer science; and from human factors engineering and design*” [Goodrich and Schultz,

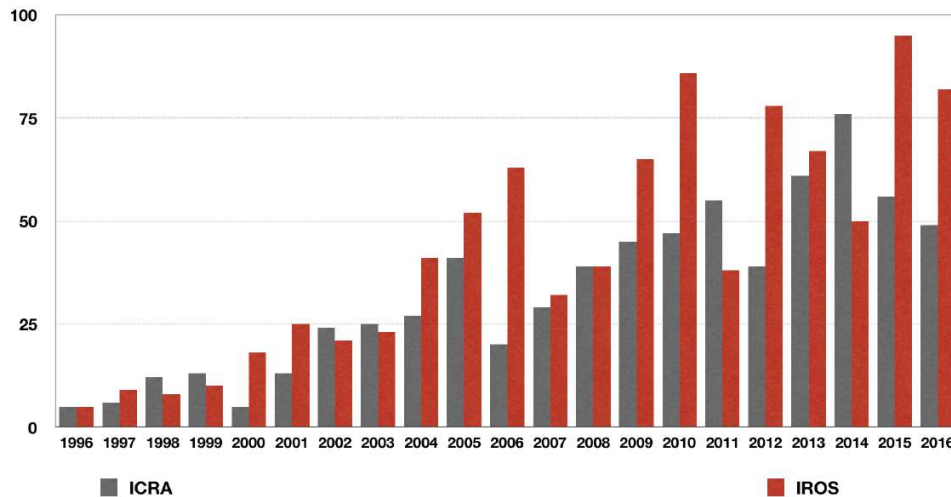


Fig. 1.1 Number of papers on HRI topics published in the 1996-2016 decades, on the proceedings of the two major robotics conferences.

2007]. This definition clearly highlights the multidisciplinary nature of the field and justifies the ever-increasing interest of the scientific community in dealing with it.

The word *interaction* is synonym of *communication*. The taxonomy of an interaction is highly vast and therefore the concept of communication is different depending on whether it is a remotely-controlled or a proximate interaction. If we consider those applications that require physical HRI (pHRI), this communication is not intended to be verbal (or visual) but it is the result of a set of forces exchanged between the interacting agents.

Nowadays, the demand for physical robotic assistance to humans is a widening practice. Robotic devices are largely widespread in many fields for fulfilling practical, and very different, daily applications such as industrial manipulators for the assembly-lines context, assistive and rehabilitative technology in clinical scenarios. By googling the keywords ‘human-robot physical interaction’, it is easy to find on the web a huge amount of pictures where humans and robots are asked to share a common working space and to cooperate in order to accomplish a required task (Figure 1.2).

The modern and advanced robots are equipped with force and tactile sensors to measure contact forces and actuators to control them with reactive strategies. But physical collaboration also requires anticipatory strategies for predicting the posture (i.e., where the human is located with respect to (w.r.t.) the robot peripersonal space) and the forces applied by the collaborative partner. At the current scientific stage, classical robots are built to act *for* humans, but in order to adapt their



(a)



(b)



(c)

Fig. 1.2 (a) Human-KUKA cooperation. (b) Human-robot cooperation in an automotive assembly line. (c) An example of pHRI in a lab environment.

[Source: Websites of (a) IIT-ADVR, (b) beautomotive.be, (c) Universitat Bayreuth.]

functionality to the current technological demand, the new generation of robots will have to collaborate *with* humans. The new frontiers in the pHRI field will deal with the development of robotic systems that will be able to react, interact and collaborate with people. This implies that the robots will be endowed with the capability to control physical collaboration through intentional interaction with humans. To achieve an effective collaboration, the robots have to be aware of who the human partner is (in terms of modelling), both in terms of positions (motion) and in terms of dynamics (contacts and exchanged forces, internal forces, joint torques). However the current state of the robot knowledge in observing human whole-body dynamics yields to non-proficient and unadaptive interactions.

To overcome this drawback, it is fundamental to understand what the response of the human body is while a physical interaction is occurring. The importance in retrieving this information is exemplified in Figure 1.3: once the human dynamics is completely known, the human feedback may be provided to the robot controllers. As a straightforward consequence, the robot may accordingly adjust the strategy

of the interaction to enhance in this way the common aim of the task. This kind of *online* awareness in the robot controllers will be the key to bridge the current limitation of robots in observing the human dynamics.

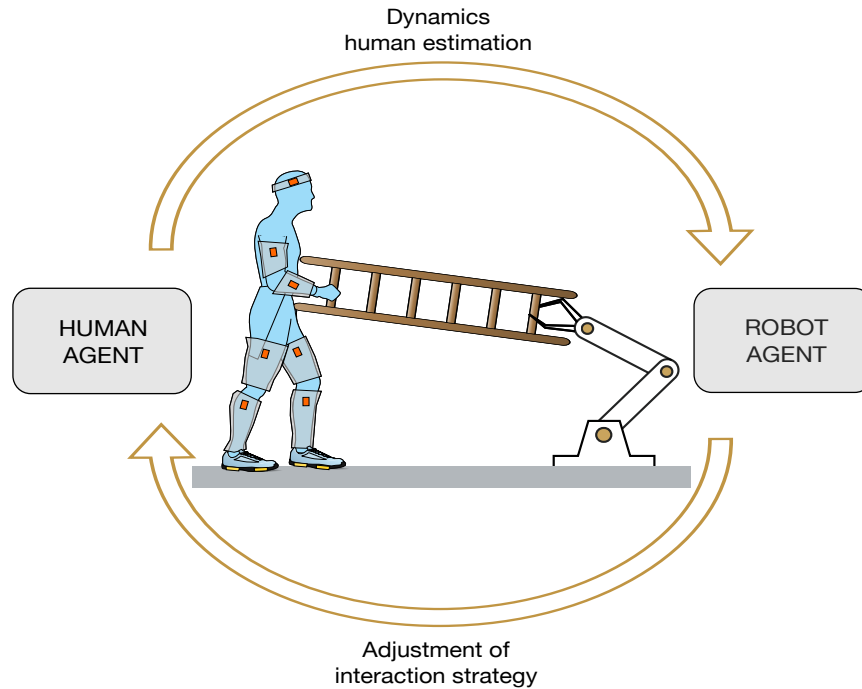


Fig. 1.3 A possible pMRI scenario: the human agent is provided with a wearable technology and an estimation algorithm allows to retrieve information about his dynamics. By properly passing his dynamics feedback to the robot, the controller renders the robot compliant to the human-robot collaboration.

## 1.2 State of the Art

The aim of this Section is to provide an overview of what is the current state and the direction of the scientific community on the topics covered by this thesis. To this purpose, it was necessary to split it into three main macro-areas concerning the state of the art on 1) the methodologies for estimating the human dynamics, 2) the current state of the sensor technology available on the market and 3) the research status on the pMRI topic.

### 1.2.1 Human Body Dynamics Estimation

The knowledge of the human body internal forces and joint torques is of pivotal importance in understanding the human dynamics. The procedure for retrieving these variables starting from the measured motion quantities is referred to as the Inverse Dynamics (ID) estimation problem.

Given a human body model composed by interconnected segments, the common mathematical approach iteratively solves the Newton-Euler equations for each model segment. The approach differs depending on the available input data, following two different paths [Winter, 1990] (see Appendix A).

- A version that solves iteratively the Newtonian physics from the top-most to the bottom-most segment (i.e., *top-down* approach) by the means of only angular acceleration measurements. However, the joint torques estimation is highly sensitive to uncertainties in acceleration data since they are retrieved by a double differentiation of the positions and, therefore, this method tends to produce noisy and non-reliable estimations [Cappozzo et al., 1975].
- A modified version that encompasses additional measurements in the form of ground reaction forces. The method, also called *bottom-up*, starts at the bottom-most segment where further boundary conditions are provided (typically ground reaction forces from force plates) and proceeds towards the top-most segment. Typically it produces more precise estimations but the introduction of additional data provides more equilibrium conditions to be satisfied: the problem arises at the top-most segment where the physics conditions are not satisfied anymore.

In general, when an additional measurement is introduced into the computation, a further constraint has to be defined at the final segment (both for top-down or bottom-up methods) in order to satisfy the equations of motion. This is due to the fact that the system of equations becomes overdetermined. The solution is retrieved by discarding 6 equations and it is strongly dependent on which equations are discarded, as recognized by [Kuo, 1998] that treats the problem of finding the joint torques as a least-squares problem. The idea here is to find a set of joint torques that best agrees with the available data and to exploit the redundancy of the system when some measurements are missing or unreliable. The main drawback is that it is applicable only to a 2D fixed-base system. In a subsequent study [van den Bogert and Su, 2008], a further development of [Kuo, 1998] is presented, not restricted to 2D fixed-base system but particularly tailored for gait analysis. The method solves ID problems where the number of the unknown variables does not exceed the degrees of freedom (DoFs) of the system by employing a weighting covariance matrix derived via Monte Carlo simulation of measurement errors.

The least-squares approach became very popular for solving the human ID estimation since it is a versatile tool for addressing optimization problems solution. Since it is historically well-known that ID accuracy is closely related to the reliability of the accelerations data [Challis and Kerwin, 1996], a weighted least-squares optimization approach is adopted in [Cahouët et al., 2002] to retrieve optimum acceleration estimates from all the available imperfect and redundant measurements (positions by markers and forces by force plates). Since the considered cost function does not contain information on the joint torques, the method is not so robust to errors in the joint torque estimation. In [Riemer and Hsiao-Wecksler, 2008], a similar methodology is used but combining two important factors: *i*) a cost function that minimizes the difference between the measured ground reaction forces and the forces estimated via a top-down approach; *ii*) an optimization criterion for the measured joint angles.

### 1.2.2 Sensors Technology

Several commercial solutions for the whole-body motion tracking are available on the market. The standard approach for motion detecting is a marker-based technology for in-lab applications produced by Vicon or MotionAnalysis. A more recent approach is to supplement or even replace marker-based technologies in several applications with wearable markerless technologies suitable for outdoor motion capturing produced by Xsens or Noraxon, where markers are replaced by body-mounted Inertial Measurement Units (IMUs). Another kind of solution is provided by the Microsoft Kinect depth camera system which allows markerless low-cost whole-body motion tracking for indoor applications [Zhang, 2012].

In biomechanics, soft wearable and stretchable systems have been proposed for measuring human body motion [Mengüç et al., 2013] [Mengüç et al., 2014], as well as in health activity monitoring [Paradiso and Rossi, 2006] [Gallego et al., 2011]. Combinations of different technologies have also been used for detecting human motion: in [Wei and Chai, 2010], a video-based motion technique has been adopted for capturing realistic human motion from video sequences.

Although these existing technologies provide a high level of accuracy in computing motion quantities, they have several limitations in measuring real-time dynamics quantities (i.e., forces and torques). A key problem lies in the fact that motion capture methods typically employ only kinematic measurement modalities (positions, velocities and accelerations) [Bonnet et al., 2013] and do not include sufficient information on the dynamics of the human movements.

The importance of including and exploiting dynamics information is a crucial point in several research areas such as ergonomics for industrial scenarios, rehabilitation monitoring, for developing prosthetic devices and exoskeleton systems or

in pHRI scenarios. For these reasons, the whole-body force tracking is not a new challenge for the scientific community, but the topic has been seldom explored *in situ* and even more rarely analyzed in real-time modality (this step requires the development of estimation algorithms to be coupled to the sensors).

To overcome the drawbacks related to the in-lab force tracking acquisitions (usually attained through the combination of a motion capture system with commercial force plates), several solutions of pressure sensing insoles are available on the market, such as Moticon or Tekscan used in [Zhang et al., 2014]. However, prototypes of sensing shoes have been proposed in the recent scientific scenario: a prototype of wearable shoes developed by Xsens [Schepers et al., 2007] and a sensory system for the foot pressure evaluation tailored for exoskeletons applications [Mateos et al., 2016].

### 1.2.3 Physical Human-Robot Interaction

Most of the pHRI studies take inspiration from the intrinsic behaviour of the human nature: the *mutual adaptive nature* that automatically occurs when two humans are cooperating together to accomplish a common task. To this purpose, the importance of understanding the human dynamics goes without saying and it is a crucial aspect of current scientific research.

Based on the pioneering study on the minimum-jerk model in human manipulation tasks [Flash and Hogan, 1985], a method based on the minimization of the jerk is used as a suitable approximation for estimating the human partner motions in [Maeda et al., 2001] during a human-robot cooperative manipulation. Here the authors' attempt is to incorporate human characteristics into the control strategy of the robot. The weakness in this type of approach lies in the pre-determination of the task and in the role that the robot has to play in the task execution. Furthermore, the minimum-jerk model reliability decreases considerably if the human partner decides to apply non-scheduled trajectory changes during the task [Miossec and Kheddar, 2009].

Another suitable route for pHRI is the *imitation learning* approach, justified by a wide variety of computational algorithms that have been developed by the scientific community in the past decades (see an exhaustive overview in [Schaal et al., 2003]). This approach yields to the *teacher-student* (or more pragmatic master-slave) interaction concept and consists in the following steps:

- *Collection of human motions*: movements of a human agent (i.e., the teacher in the imitation process) are retrieved with motion capture techniques and clustered in motion databases. Some publicly available examples are [Guerra-Filho and Biswas, 2011] [Kuehne et al., 2011] [Wojtusich and von Stryk, 2015] [C. Mandery and Asfour, 2015].

- *Classification for model abstraction*: human motions are classified via motion segmentation in order to abstract motion models. The model abstraction is feasible by postulating that the human movements can be decomposed into a set of primitive actions, termed *motion primitives*.
- *Models retargeting*: human motion models are mapped into a robot platforms, i.e., the student in the imitation process. The retargeting implies the development of robot control algorithms capable of learning motion models from these primitives [Amor et al., 2014] [Terlemez et al., 2014], [Mandery et al., 2016] in order to emulate human-like movements.

Since the primitives have to be perceived and interpreted by a robot, a common ‘language’ has to be mandatorily adopted. The abstraction implies, therefore, to define the primitives in terms of positions, velocities and accelerations. In a recent work [Borràs et al., 2017], the collection of human motions is performed when the human is interacting with the external environment and exploiting multi-contact support to enhance his stability. Here, the classical characterization of a primitive (through the kinematic above-mentioned variables) is coupled with the important information on how the human is maintaining his stability.

In general, although in the imitation approach the task pre-determination does not represent a drawback anymore, a relevant problem (termed *correspondence problem*) concerns the comparability of the models (teacher vs. student). Human motion primitives are exploitable only if their knowledge could be properly mapped into a compatible robot kinematic/dynamic model. This inevitably narrows down the potential student-role candidate to anthropomorphic robots and it requires an accurate analysis on the imitation mechanism assumptions.

### 1.3 Contribution

The thesis contribution lies in the development of a novel wearable technology for the simultaneous force and motion human tracking. The attempt of this work is to bridge the current state-of-the-art gap on human dynamics analysis thanks to

- a combination of different sensors (body-mounted IMUs, force sensing)
- a whole-body force estimation algorithm, originally developed for the humanoid iCub robot [Nori et al., 2015] and tailored here for the human body.

The novelty of the approach consists in framing the dynamics computation in a probabilistic Gaussian framework when redundant measurements occur. In this way, sensors play an *active* role in the computation since the classical boundary

conditions in the recursive Newton-Euler algorithm are replaced with the sensors readings. The estimation algorithm solves a sort of weighted least-squares problem where the weights are given by the dynamic model and the sensors.

### 1.3.1 Publications

Here following the list of the related publications (at the time of writing) produced during my Ph.D. course period:

- Romano, F.; Nava, G.; Azad, M.; Camernik, J.; Dafarra, S.; Dermly, O.; Latella, C.; Lazzaroni, M.; Lober, R.; Lorenzini, M.; Pucci, D.; Sigaud, O.; Traversaro, S.; Babic, J.; Ivaldi, S.; Mistry, M.; Padois, V.; Nori, F. “The CoDyCo Project achievements and beyond: Towards Human Aware Whole-body Controllers for Physical Human Robot Interaction”, Special issue on Human Cooperative Wearable Robotic Systems in IEEE Robotics and Automation Letters, 3:516-523, November 2017. (RA-L), 2017, PP, 99. doi: 10.1109/LRA.2017.2768126, <http://ieeexplore.ieee.org/document/8093992>.
- Latella, C.; Kuppuswamy, N.; Romano, F.; Traversaro, S.; Nori, F. “Whole-Body Human Inverse Dynamics with Distributed Micro-Accelerometers, Gyros and Force Sensing”, Sensors 2016, 16, 727. doi: 10.3390/s16050727, <http://www.mdpi.com/1424-8220/16/5/727>.
- Latella, C.; Kuppuswamy, N.; Nori, F. “WearDY: Wearable dynamics. A prototype for human whole-body force and motion estimation”, AIP Conference Proceedings 1749, 020011 (2016). doi: <http://dx.doi.org/10.1063/1.4954494>.

## 1.4 Technological Outcome

The framework proposed in this thesis is the core of the Horizon-2020 European project named An.Dy - Advancing Anticipatory Behaviors in Dyadic Human-Robot Collaboration (H2020-ICT-2016-2017, No.731540) [An.Dy, 2017]. The project aims at advancing the current state of the art in the pHRI field by providing a novel wearable technology that measures human whole-body dynamics and, in turns, endows robots with the ability to be more aware of the human partner they are interacting with. An.Dy will enhance the intentional cooperation between humans and robots. The results achieved in this thesis represent the entry point and the basis on which An.Dy will lay its foundations in the next years.

## 1.5 Thesis Outline

Hereafter, a brief summary of the topics of the thesis is provided. Each chapter briefly introduces the topic and starts (if needed) with the notation useful for guiding the reader into its comprehension.

Chapter 2 introduces a complete overview of the kinematics and the dynamics of a rigid body and, then, of a system of rigid bodies.

Given the notions from the previous chapter, Chapter 3 describes the human whole-body modelling as a system of articulated rigid bodies.

In Chapter 4, the human dynamics estimation problem is presented and it is provided a solution in a probabilistic domain.

Chapter 5 describes the Matlab software implementation for the offline validation of the framework. It shows the sensing technologies used for the algorithm and introduces also a new wearable prototype developed at Istituto Italiano di Tecnologia for measuring ground reaction forces.

The main contribution of Chapter 6 is the design of a YARP tool for the real-time monitoring of the human dynamics.

Chapter 7 discusses the possibility to extend the human dynamics estimation framework to a new framework where a physical interaction with the iCub robot is encompassed.

Chapter 8 concludes the thesis with a general overview on the obtained preliminary results and analyzes possible improvements as forthcoming works.

## Chapter 2

# Rigid Multi-Body System

*Nothing happens until something moves.*

Albert Einstein

In this Chapter a complete overview of the kinematics and the dynamics of a rigid multi-body system is introduced. For achieving this objective, a detailed description of the ‘sub-units’ that describe a multi-body system is mandatorily needed. The sub-units are the bodies and the joints which a system is made of. The reader will be provided with some tools that describe the kinematics and the dynamics of a rigid body and, only then, with the multi-body system notions.

### 2.1 Notation

Hereafter some important math preliminaries adopted through the thesis.

- Let  $\mathbb{R}$  be the set of real numbers.  $\mathbf{p} \in \mathbb{R}^n$  is a  $n$ -dimensional column vector of real numbers. Let  $p$  denote a scalar quantity.
- A matrix of dimensions  $m \times n \in \mathbb{R}^{m \times n}$ .
- Let  $\mathbf{1}_n$  be the identity matrix of dimension  $n \in \mathbb{R}^{n \times n}$ .
- Let  $\mathbf{0}_n$  be the zero matrix  $\in \mathbb{R}^{n \times n}$  and  $\mathbf{0}_{m \times n} \in \mathbb{R}^{m \times n}$ .
- Given two generic vectors  $\mathbf{p}, \mathbf{u} \in \mathbb{R}^3$ , their inner product is denoted with  $\mathbf{p}^T \mathbf{u}$ . The cross product  $\in \mathbb{R}^3$  is denoted as  $\mathbf{p} \times \mathbf{u}$ , where

$$\mathbf{p} \times := \begin{bmatrix} 0 & -p_z & p_y \\ p_z & 0 & -p_x \\ -p_y & p_x & 0 \end{bmatrix} \in \mathbb{R}^{3 \times 3}. \quad (2.1)$$

- Given a vector  $\mathbf{p}$  and a reference frame  $\mathcal{B}$ , the notation  ${}^{\mathcal{B}}\mathbf{p}$  denotes the vector  $\mathbf{p}$  expressed in  $\mathcal{B}$ .
- Let  $SO(3)$  be the set of  $\mathbb{R}^{3 \times 3}$  orthogonal matrices with determinant equal to one, such that

$$SO(3) := \{ \mathbf{R} \in \mathbb{R}^{3 \times 3} \mid \mathbf{R}^T \mathbf{R} = \mathbf{1}_3, \quad |\mathbf{R}| = 1 \}. \quad (2.2)$$

- Let  $so(3)$  be the set of the skew-symmetric matrices  $\in \mathbb{R}^{3 \times 3}$ , such that

$$so(3) := \{ \mathbf{S} \in \mathbb{R}^{3 \times 3} \mid \mathbf{S}^T = -\mathbf{S} \}. \quad (2.3)$$

- Let the set  $SE(3)$  be defined as

$$SE(3) := \left\{ \begin{bmatrix} \mathbf{R} & \mathbf{p} \\ \mathbf{0}_{1 \times 3} & 1 \end{bmatrix} \in \mathbb{R}^{4 \times 4} \mid \mathbf{R} \in SO(3), \quad \mathbf{p} \in \mathbb{R}^3 \right\}. \quad (2.4)$$

## 2.2 The Non-Deformability Assumption

In the physics formalism, a rigid body is represented as a body which does not deform under the application of an external force. This means that the distance between two generic points in the body does not vary when a force is exerted on it, i.e., the body is *non-deformable*. In real life, this utopian condition does not exist. There are situations in which the body deforms depending, for example, on the magnitude or the point of application of a force. However, under the hypothesis that the deformation is small, i.e., *negligible*, the rigid body assumption allows to describe the dynamics of every physical object.

## 2.3 Rigid Body Kinematics

The kinematics of a rigid body concerns the mechanism of its motion without considering the forces and torques that caused it. Among the robotics community, the most influential description of the rigid body kinematics [Siciliano and Khatib, 2007] [Siciliano et al., 2008] is through its *position* and its *orientation* w.r.t. a known coordinate reference frame. The body velocity and acceleration depend on this representation.

### 2.3.1 Pose Representation

The rigid body kinematics can be described by the *pose* representation, i.e., the position and orientation w.r.t. a reference frame. Let the frame  $\mathcal{I}$  (i.e., ‘inertial’) be a reference frame with the origin in a 3D point  $O_{\mathcal{I}}$ . Let  $\mathcal{B}$  (i.e., ‘body’) be another frame with the origin in the 3D point  $O_{\mathcal{B}}$  attached to the rigid body. Consider now that  $\mathcal{B}$  moves w.r.t.  $\mathcal{I}$ . Every type of motion of the body (translation, rotation or a combination of the two) will produce a variation in its pose. This means that the pose representation becomes a powerful tool for describing the entire kinematics of the rigid body.

The coordinates of the point  $O_{\mathcal{B}}$  w.r.t.  $\mathcal{I}$  are clustered in the position vector  ${}^{\mathcal{I}}\mathbf{o}_{\mathcal{B}}$  whose origins in  $O_{\mathcal{I}}$  and points to  $O_{\mathcal{B}}$ , such that

$${}^{\mathcal{I}}\mathbf{o}_{\mathcal{B}} = \begin{bmatrix} {}^{\mathcal{I}}o_x \\ {}^{\mathcal{I}}o_y \\ {}^{\mathcal{I}}o_z \end{bmatrix}_{\mathcal{B}} \in \mathbb{R}^3. \quad (2.5)$$

#### The Rotation Matrix

The orientation of  $\mathcal{B}$  w.r.t.  $\mathcal{I}$  is described by a rotation matrix  $\mathbf{R} \in SO(3)$ , regardless of the positions of the origins  $O_{\mathcal{I}}$  and  $O_{\mathcal{B}}$ . Additionally, the rotation matrix can be seen as a tool for operating coordinates transformation between two frames: given a point  $P$  (in Figure 2.1) and its coordinates vector  $\mathbf{p}$  expressed in  $\mathcal{B}$ , the rotation matrix  ${}^{\mathcal{I}}\mathbf{R}_{\mathcal{B}}$  transforms its coordinates from the frame  $\mathcal{B}$  to the frame  $\mathcal{I}$ , such that

$${}^{\mathcal{I}}\mathbf{p} = {}^{\mathcal{I}}\mathbf{R}_{\mathcal{B}} {}^{\mathcal{B}}\mathbf{p}. \quad (2.6)$$

#### The Homogeneous Transformation

The formalism that best summarizes the pose of a rigid body is the homogeneous transformation matrix  $\mathbf{H} \in SE(3)$ . Let  ${}^{\mathcal{I}}\tilde{\mathbf{p}}, {}^{\mathcal{B}}\tilde{\mathbf{p}}$  be two vectors  $\in \mathbb{R}^4$ , i.e.,  ${}^{\mathcal{I}}\tilde{\mathbf{p}} = [{}^{\mathcal{I}}\mathbf{p} \ 1]^T$ ,  ${}^{\mathcal{B}}\tilde{\mathbf{p}} = [{}^{\mathcal{B}}\mathbf{p} \ 1]^T$ , such that

$${}^{\mathcal{I}}\tilde{\mathbf{p}} = {}^{\mathcal{I}}\mathbf{H}_{\mathcal{B}} {}^{\mathcal{B}}\tilde{\mathbf{p}}, \quad (2.7)$$

being

$${}^{\mathcal{I}}\mathbf{H}_{\mathcal{B}} = \begin{bmatrix} {}^{\mathcal{I}}\mathbf{R}_{\mathcal{B}} & {}^{\mathcal{I}}\mathbf{o}_{\mathcal{B}} \\ \mathbf{0}_{1 \times 3} & 1 \end{bmatrix}. \quad (2.8)$$

The Equation (2.8) is a compact way to represent the position along with the rotational component of the motion. If  $O_{\mathcal{B}} \equiv O_{\mathcal{I}}$  (i.e., null position vector  ${}^{\mathcal{I}}\mathbf{o}_{\mathcal{B}}$ ), (2.7) falls into the pure rotational case (2.6). If the frame  $\mathcal{B}$  is not rotated w.r.t.  $\mathcal{I}$  (i.e., the rotation matrix  ${}^{\mathcal{I}}\mathbf{R}_{\mathcal{B}} = \mathbf{1}_3$ ) thus (2.7) becomes  ${}^{\mathcal{I}}\mathbf{p} = {}^{\mathcal{B}}\mathbf{p} + {}^{\mathcal{I}}\mathbf{o}_{\mathcal{B}}$ .

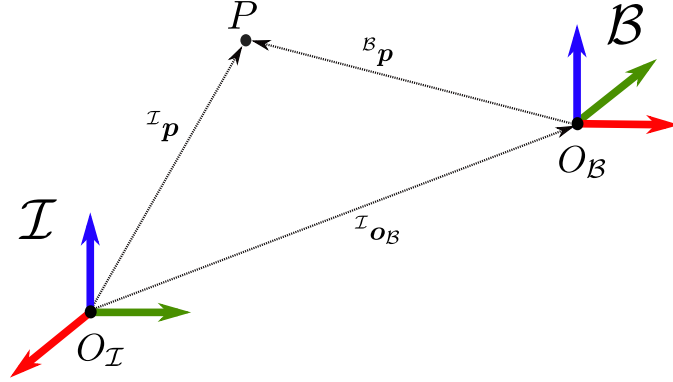


Fig. 2.1 Standard representation of a point  $P$  in two different coordinate frames. The figure introduces the RGB (Red-Green-Blue) convention for  $x$ - $y$ - $z$  axes.

It is worth noting that, throughout the thesis, the reference frames are shown using a RGB (Red-Green-Blue) convention for  $x$ - $y$ - $z$  axes, respectively.

### 2.3.2 The Derivative of a Rotation Matrix

In this framework, the derivative of the rotation matrix raises with particular emphasis since it allows to describe the velocity and the acceleration of a rigid body. Even if not explicitly defined in the text, consider  $\mathbf{R}$  a time-varying matrix. It is shown (and the reader is addressed to [Siciliano et al., 2008], Section 3.1.1, for a detailed description) that there is a straightforward relation between  $\mathbf{R}$  and the skew-symmetric operator  $\mathbf{S} \in so(3)$ , such that

$$\mathbf{S} = \dot{\mathbf{R}}\mathbf{R}^T . \quad (2.9)$$

#### Velocity

Given an inertial frame  $\mathcal{I}$ , a body reference frame  $\mathcal{B}$  and a point  $P$  of the body (Figure 2.2), for (2.7) we can define the following equation

$${}^{\mathcal{I}}\mathbf{p} = {}^{\mathcal{I}}\mathbf{o}_B + {}^{\mathcal{I}}\mathbf{R}_B {}^{\mathcal{B}}\mathbf{p} . \quad (2.10)$$

The velocity of  $P$  w.r.t.  $\mathcal{I}$  can be obtained by using the first-order time derivative of (2.10), such that

$${}^{\mathcal{I}}\dot{\mathbf{p}} = \frac{d}{dt} ({}^{\mathcal{I}}\mathbf{p}) = {}^{\mathcal{I}}\dot{\mathbf{o}}_B + {}^{\mathcal{I}}\dot{\mathbf{R}}_B {}^{\mathcal{B}}\mathbf{p} . \quad (2.11)$$

It is worth noting that  ${}^{\mathcal{B}}\mathbf{p}$  is not a time-varying quantity as a direct consequence of the non-deformability assumption of the body (see Section 2.2). Equation (2.9) yields to  $\dot{\mathbf{R}} = \mathbf{S} \mathbf{R}$ , thus in (2.11)

$${}^{\mathcal{I}}\dot{\mathbf{p}} = {}^{\mathcal{I}}\dot{\mathbf{o}}_{\mathcal{B}} + \mathbf{S} {}^{\mathcal{I}}\mathbf{R}_{\mathcal{B}} {}^{\mathcal{B}}\mathbf{p}. \quad (2.12)$$

If  $\boldsymbol{\omega}_{\mathcal{B}}$  is the angular velocity of the frame  $\mathcal{B}$  w.r.t.  $\mathcal{I}$ , thus the above equation can be written as

$${}^{\mathcal{I}}\dot{\mathbf{p}} = {}^{\mathcal{I}}\dot{\mathbf{o}}_{\mathcal{B}} + \boldsymbol{\omega}_{\mathcal{B}} \times {}^{\mathcal{I}}\mathbf{R}_{\mathcal{B}} {}^{\mathcal{B}}\mathbf{p}. \quad (2.13)$$

This implies that  $\mathbf{S}$  is actually the skew-symmetric matrix for the angular acceleration, such that

$$\mathbf{S}(\boldsymbol{\omega}_{\mathcal{B}}) := \boldsymbol{\omega}_{\mathcal{B}} \times = \begin{bmatrix} 0 & -\omega_z & \omega_y \\ \omega_z & 0 & -\omega_x \\ -\omega_y & \omega_x & 0 \end{bmatrix}_{\mathcal{B}} \in so(3). \quad (2.14)$$

### Acceleration

Similarly, the acceleration of P w.r.t.  $\mathcal{I}$  can be obtained by using the second-order time derivative of (2.10), such that

$$\begin{aligned} {}^{\mathcal{I}}\ddot{\mathbf{p}} &= \frac{d^2}{dt^2}({}^{\mathcal{I}}\mathbf{p}) = {}^{\mathcal{I}}\ddot{\mathbf{o}}_{\mathcal{B}} + \dot{\boldsymbol{\omega}}_{\mathcal{B}} \times {}^{\mathcal{I}}\mathbf{R}_{\mathcal{B}} {}^{\mathcal{B}}\mathbf{p} + \boldsymbol{\omega}_{\mathcal{B}} \times {}^{\mathcal{I}}\dot{\mathbf{R}}_{\mathcal{B}} {}^{\mathcal{B}}\mathbf{p} \\ &= {}^{\mathcal{I}}\ddot{\mathbf{o}}_{\mathcal{B}} + \dot{\boldsymbol{\omega}}_{\mathcal{B}} \times {}^{\mathcal{I}}\mathbf{R}_{\mathcal{B}} {}^{\mathcal{B}}\mathbf{p} + \boldsymbol{\omega}_{\mathcal{B}} \times (\boldsymbol{\omega}_{\mathcal{B}} \times {}^{\mathcal{I}}\mathbf{R}_{\mathcal{B}} {}^{\mathcal{B}}\mathbf{p}). \end{aligned} \quad (2.15)$$

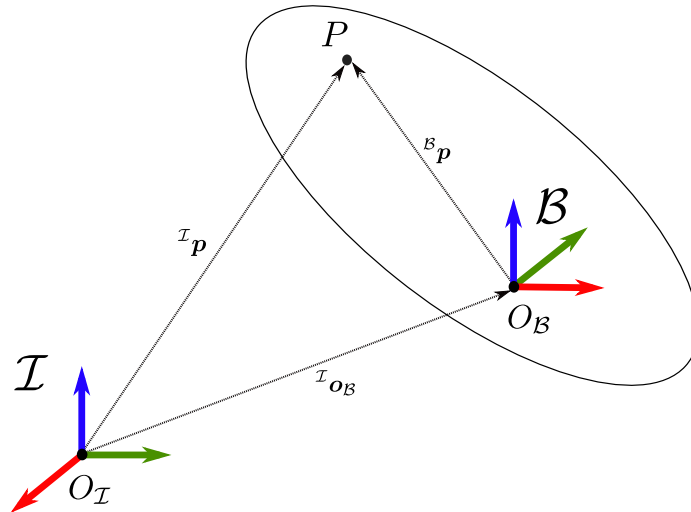


Fig. 2.2 Rigid body with frame  $\mathcal{B}$  and point P that is moving w.r.t. frame  $\mathcal{I}$ .

### 2.3.3 6D Motion Vectors

A 6D motion vector represents a *spatial* vector of a quantity that describes the motion of a body (e.g., the velocity and the acceleration). Given a generic spatial vector  $\underline{\mathbf{p}} \in \mathbb{R}^6$ , the three first entries are the coordinates of its linear part  $\in \mathbb{R}^3$ , and the last three entries represent the angular part  $\in \mathbb{R}^3$  of the same quantity, such that

$$\underline{\mathbf{p}} = \begin{bmatrix} \mathbf{p}^{lin} \\ \mathbf{p}^{ang} \end{bmatrix} \in \mathbb{R}^6. \quad (2.16)$$

Within this new formalism, the velocity (i.e., the *spatial velocity*) of the rigid body expressed w.r.t.  $\mathcal{I}$  can be written as

$$\mathcal{I}\underline{\mathbf{v}}_{\mathcal{B}} = \begin{bmatrix} \mathcal{I}\dot{\mathbf{p}} \\ \boldsymbol{\omega}_{\mathcal{B}} \end{bmatrix} \in \mathbb{R}^6. \quad (2.17)$$

Similarly, the spatial notation for the acceleration (i.e., the *spatial acceleration*) of the rigid body expressed w.r.t.  $\mathcal{I}$  is

$$\mathcal{I}\underline{\mathbf{a}}_{\mathcal{B}} = \begin{bmatrix} \mathcal{I}\ddot{\mathbf{p}} \\ \dot{\boldsymbol{\omega}}_{\mathcal{B}} \end{bmatrix} \in \mathbb{R}^6. \quad (2.18)$$

#### Adjoint Transformation for Motion Vectors

When dealing with spatial vectors, the change of frame can not be performed by using an homogeneous transformation but it has to be introduced a new transformation matrix, i.e., the adjoint matrix  $\mathbf{X} \in \mathbb{R}^{6 \times 6}$  define as follows.

Let  $\mathcal{A}$  and  $\mathcal{B}$  be two generic frames and  ${}^{\mathcal{B}}\mathbf{o}_{\mathcal{A}}$  the position vector of the origin of  $\mathcal{A}$  w.r.t.  $\mathcal{B}$ , thus the adjoint transformation is

$${}^{\mathcal{B}}\mathbf{X}_{\mathcal{A}} = \begin{bmatrix} {}^{\mathcal{B}}\mathbf{R}_{\mathcal{A}} & \mathbf{0}_3 \\ -{}^{\mathcal{B}}\mathbf{R}_{\mathcal{A}}\mathbf{S}({}^{\mathcal{B}}\mathbf{o}_{\mathcal{A}}) & {}^{\mathcal{B}}\mathbf{R}_{\mathcal{A}} \end{bmatrix}, \quad (2.19)$$

such that

$${}^{\mathcal{B}}\underline{\mathbf{v}}_{\mathcal{A}} = {}^{\mathcal{B}}\mathbf{X}_{\mathcal{A}} {}^{\mathcal{A}}\underline{\mathbf{v}}_{\mathcal{A}}. \quad (2.20)$$

#### The Cross Product $\times$ for Motion Vectors

Within the framework of the motion vectors, the cross product operator as previously defined is not useful anymore. In (2.1) it is defined in  $\mathbb{R}^3$  while now we are operating in the new  $\mathbb{R}^6$  formalism. Thus, it has to be properly modified for matching the spatial context.

Consider a rigid body with a body frame  $\mathcal{B}$  that is moving with a spatial velocity  $\underline{v}_{\mathcal{B}}$ , as defined in (2.17). If the generic vector  $\underline{u}$  is a motion vector (e.g., the spatial acceleration of the body), thus their cross product is

$${}^{\mathcal{I}}\underline{v}_{\mathcal{B}} \times \underline{u} \in \mathbb{R}^6 . \quad (2.21)$$

In particular, the cross product operator is such that

$${}^{\mathcal{I}}\underline{v}_{\mathcal{B}} \times := \begin{bmatrix} \boldsymbol{\omega}_{\mathcal{B}} \times & {}^{\mathcal{I}}\dot{\underline{p}} \\ \mathbf{0}_3 & \boldsymbol{\omega}_{\mathcal{B}} \times \end{bmatrix} \in \mathbb{R}^{6 \times 6} , \quad (2.22)$$

where it is easy to identify in the term  $\boldsymbol{\omega}_{\mathcal{B}} \times$  the skew-symmetric matrix defined as in Equation (2.14).

## 2.4 Rigid Body Dynamics

In classical mechanics, the dynamics is that branch concerned with the study of the forces and torques and their effect on the motion of a body. It is worth remarking that although sometimes it is referred to this branch as the *kinetics* of the rigid body [Winter, 1990] [Robertson et al., 2014], we prefer here to address to the *dynamics* (as in [Siciliano and Khatib, 2007] [Featherstone, 2007]). Clearly the reader has to know that the two definitions are completely equivalent.

### 2.4.1 6D Force Vectors

Similarly to the motion vector case, also in the context of dynamics it is possible to define a specific class of 6D vectors related to the force. As previously, a force vector contains a pair of 3D vectors: the first vector represents the resultant of the forces  ${}^{\mathcal{I}}\underline{f}$  acting on the body, the last one is referred to the moments  ${}^{\mathcal{I}}\underline{m}$  produced by the resultant w.r.t. a given point. This yields to the following notation:

$${}^{\mathcal{I}}\underline{f} = \begin{bmatrix} {}^{\mathcal{I}}\underline{f} \\ {}^{\mathcal{I}}\underline{m} \end{bmatrix} \in \mathbb{R}^6 . \quad (2.23)$$

### Adjoint Transformation for Force Vectors

The adjoint transformation for a 6D force vector is

$${}^{\mathcal{B}}\mathbf{X}_{\mathcal{A}}^* = \begin{bmatrix} {}^{\mathcal{B}}\mathbf{R}_{\mathcal{A}} & -{}^{\mathcal{B}}\mathbf{R}_{\mathcal{A}} \mathbf{S} ({}^{\mathcal{B}}\underline{o}_{\mathcal{A}}) \\ \mathbf{0}_3 & {}^{\mathcal{B}}\mathbf{R}_{\mathcal{A}} \end{bmatrix} , \quad (2.24)$$

such that

$${}^B \underline{\mathbf{f}}_{\mathcal{A}} = {}^B \mathbf{X}_{\mathcal{A}}^* {}^A \underline{\mathbf{f}}_{\mathcal{A}}, \quad (2.25)$$

being  $\mathcal{A}$ ,  $\mathcal{B}$  and  ${}^B \mathbf{o}_{\mathcal{A}}$ , two generic frames and the position vector of the origin of  $\mathcal{A}$  w.r.t.  $\mathcal{B}$ , respectively.

### The (Dual) Cross Product $\times^*$ for Force Vectors

Similarly to the cross product for the motion vectors, we have a cross product for the force vectors that is the dual version of (2.22). Within the same framework explained for the motion case, we have

$${}^I \underline{\mathbf{v}}_{\mathcal{B} \times^*} := \begin{bmatrix} \boldsymbol{\omega}_{\mathcal{B} \times} & \mathbf{0}_3 \\ {}^I \dot{\mathbf{p}} & \boldsymbol{\omega}_{\mathcal{B} \times} \end{bmatrix} \in \mathbb{R}^{6 \times 6}, \quad (2.26)$$

such that

$${}^I \underline{\mathbf{v}}_{\mathcal{B} \times^*} \underline{\mathbf{f}} \in \mathbb{R}^6. \quad (2.27)$$

## 2.4.2 The Newton-Euler Equations of Motion

The equations of motion describe the mathematical model for the dynamics of the rigid body. Within the spatial formalism, it is possible to write the equations of motion as

$$\underline{\mathbf{f}} = \frac{d}{dt}(\underline{\mathbf{I}}\underline{\mathbf{v}}) = \underline{\mathbf{I}}\underline{\mathbf{a}} + \underline{\mathbf{v}} \times^* \underline{\mathbf{I}}\underline{\mathbf{v}}, \quad (2.28)$$

where the force of a rigid body that is moving with velocity  $\underline{\mathbf{v}}$  and acceleration  $\underline{\mathbf{a}}$  is equal to the rate of change of its momentum  $\underline{\mathbf{I}}\underline{\mathbf{v}}$ . In Equation (2.28),

- $\underline{\mathbf{f}} \in \mathbb{R}^6$  in the net force acting on the rigid body;
- $\underline{\mathbf{I}}$  is the spatial inertia tensor  $\in \mathbb{R}^{6 \times 6}$ , such that

$$\underline{\mathbf{I}} = \begin{bmatrix} \mathbf{I} + m \mathbf{c} \times \mathbf{c}^\top & m \mathbf{c} \times \\ m \mathbf{c} \times^\top & m \mathbf{1}_3 \end{bmatrix}, \quad (2.29)$$

where  $\mathbf{I}$  is the inertia tensor w.r.t. the link center of mass (CoM),  $m$  is the body mass,  $\mathbf{c}$  is the position vector from the CoM of the body to the origin of the body frame  $\mathcal{B}$ ;

- the term  $\underline{\mathbf{v}} \times^*$  is the operator that maps  $\underline{\mathbf{I}}$  to its derivative  $\dot{\underline{\mathbf{I}}}$ .

## 2.5 Rigid Multi-Body System

A rigid multi-body system is a system composed of two or more interconnected rigid bodies. The resulting motion of a system is obtained by composing elementary motions of each body w.r.t. the coupled one. The mobility of the system is ensured by the presence of the *joints*: each joint interconnects two bodies and constraints their motion. The type of motion is strongly related to the type of joint but the description of the different types of joints is out of the scope of the thesis. Thus, they will be described in detailed only when required for the thesis understanding.

### 2.5.1 Modelling

Within a classical widespread formalism in robotics [Featherstone, 2007] [Siciliano et al., 2008], an articulated rigid multi-body system is represented as a kinematic tree composed of rigid bodies. The topology of the system (i.e., the interconnectivity property) is such that it is often referred to it as a tree system. Under the tree schematization formalism, the bodies are the nodes and the connection between them are the joints. Each rigid body in the system is associated to a unique node in the tree.

Let  $N_B$  be the number of moving rigid bodies of the system whose topological numbering is defined from 1 to  $N_B$  (0 refers to the fixed base). Let  $i$  be the index for a generic body in the tree such that  $1 < i < N_B$ . Node numbers can be always selected in a topological order so that the  $i$ -th node has a higher number than its unique parent  $\lambda(i)$  and a smaller number than all the nodes in the set of its children  $\mu(i)$ .

The  $i$ -th body and its parent  $\lambda(i)$  are coupled with joint  $i$  according to the Denavit-Hartenberg convention for joint numbering [Denavit and Hartenberg, 1955]. The motion freedom subspace of the  $i$ -th joint is modelled with  $\mathcal{S}_i \in \mathbb{R}^{6 \times n_i}$ , being  $n_i$  the DoFs number of the joint  $i$ . Within this notation,  $n = n_1 + \dots + n_{N_B}$  represents the internal DoFs of the system. Figure 2.3 shows a connectivity system representation for the kinematic tree.

### 2.5.2 Lagrangian Representation

A common representation of the dynamics of the system is derived from the Lagrangian formalism. Given a rigid multi-body system with  $n$  internal DoFs, by rearranging the Lagrange formulation (the reader could refer to several robotics textbooks like [Siciliano et al., 2008], Chapter 7), it is possible to define its floating-base dynamics representation<sup>1</sup> as follows:

---

<sup>1</sup>Representation in which none of the links have an a priori constant pose w.r.t. the inertial frame.

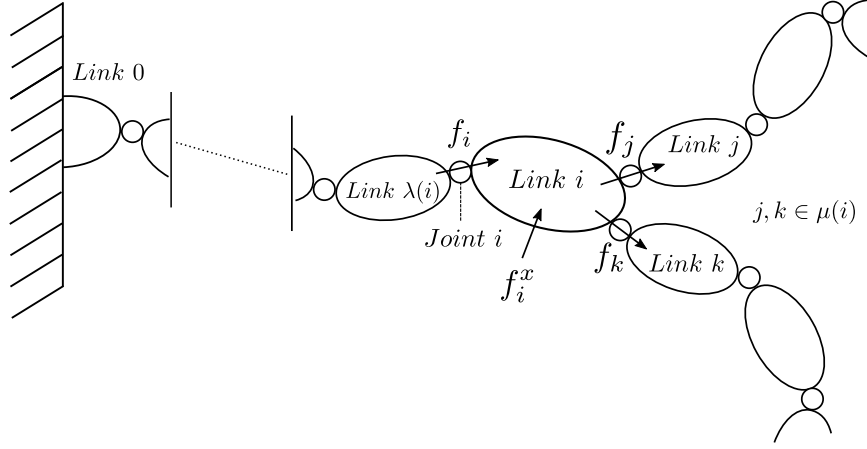


Fig. 2.3 Connectivity representation of an articulated rigid multi-body system as a kinematic tree.

$$\mathbf{M}(\mathbf{q})\dot{\boldsymbol{\nu}} + \mathbf{C}(\mathbf{q}, \boldsymbol{\nu})\boldsymbol{\nu} + \mathbf{G}(\mathbf{q}) = \begin{bmatrix} \mathbf{0} \\ \boldsymbol{\tau} \end{bmatrix} + \mathbf{J}^\top(\mathbf{q})\mathbf{f}, \quad (2.30)$$

where  $\mathbf{M} \in \mathbb{R}^{(n+6) \times (n+6)}$  is the mass matrix,  $\mathbf{C} \in \mathbb{R}^{(n+6) \times (n+6)}$  is the Coriolis effects matrix,  $\mathbf{G} \in \mathbb{R}^{n+6}$  is the gravity bias term.

In general, a floating-base system is defined by its configuration  $\mathbf{q} = (\mathcal{I}\mathbf{H}_B, \mathbf{q}_j) \in SE(3) \times \mathbb{R}^n$  and its velocity  $\boldsymbol{\nu} = (\mathcal{I}\mathbf{v}_B, \dot{\mathbf{q}}_j) \in \mathbb{R}^{n+6}$ , where  $\mathcal{I}$  is the inertial frame and  $\mathcal{B}$  the base frame.  $\mathcal{I}\mathbf{H}_B$  is the homogeneous transformation from  $\mathcal{B}$  to  $\mathcal{I}$  and  $\mathcal{I}\mathbf{v}_B$  is the base velocity w.r.t.  $\mathcal{I}$ . The configuration and the velocity of the internal DoFs are denoted with  $\mathbf{q}_j$  and  $\dot{\mathbf{q}}_j$ , respectively. The system can interact with the external environment and this results in the presence of  $\mathbf{f} \in \mathbb{R}^{6k}$ , where  $k$  is the number of the forces exchanged during the interaction. The Jacobian associated with the forces  $\mathbf{f}$  is denoted by  $\mathbf{J}(\mathbf{q})$  and the vector  $\boldsymbol{\tau} \in \mathbb{R}^n$  represents the joint torques of the system.

Throughout the thesis the human experiments will be performed with the feet fixed to the ground. We limit to consider therefore the human system to be fixed base, i.e.,  $\mathcal{I}\mathbf{H}_B = \text{const}$  and known a priori and  $\mathcal{I}\mathbf{v}_B = \mathbf{0}$ . This choice straightforwardly implies  $\mathbf{q} = \mathbf{q}_j$  and allows to reduce remarkably the framework complexity. These assumptions yield to a simplified version of (2.30), such that

$$\mathbf{M}(\mathbf{q})\ddot{\mathbf{q}} + \mathbf{C}(\mathbf{q}, \dot{\mathbf{q}})\dot{\mathbf{q}} + \mathbf{G}(\mathbf{q}) = \begin{bmatrix} \mathbf{0} \\ \boldsymbol{\tau} \end{bmatrix} + \mathbf{J}^\top(\mathbf{q})\mathbf{f}. \quad (2.31)$$

### 2.5.3 Newton-Euler Representation

The Newton-Euler formulation is an equivalent way to the Lagrangian formalism for representing the dynamics of a multi-body system. It is based on the balance of the forces acting on each body composing the structure of the system and leads to a set of recursive equations for propagating the kinematics and dynamics quantities throughout the system.

Consider a system of  $N_B$  rigid bodies connected by joints. The topology and the body numbering are defined as in Section 2.5.1. Let 0 be the fixed base. If  $1 < i < N_B$ , the velocity of the  $i$ -th link and the velocity through the  $i$ -th joint are defined recursively as follows:

$$\underline{v}_{J_i} = \bar{\mathbf{S}}_i \dot{q}_i, \quad (2.32)$$

$$\underline{v}_i = {}^i \mathbf{X}_{\lambda(i)} \underline{v}_{\lambda(i)} + \underline{v}_{J_i}. \quad (2.33)$$

Given Equations (2.32) and (2.33), the recursive Newton-Euler algorithm (RNEA) consists of the following steps, expressed in body  $i$  coordinates<sup>2</sup>:

$$\underline{a}_i = {}^i \mathbf{X}_{\lambda(i)} \underline{a}_{\lambda(i)} + \bar{\mathbf{S}}_i \ddot{q}_i + \underline{v}_i \times \underline{v}_{J_i}, \quad (2.34)$$

$$\underline{f}_i^B = \mathbf{I}_i \underline{a}_i + \underline{v}_i \times {}^* \mathbf{I}_i \underline{v}_i, \quad (2.35)$$

$$\underline{f}_i = \underline{f}_i^B - {}^i \mathbf{X}_0^* \underline{f}_i^x + \sum_{\mu(i)} {}^i \mathbf{X}_{\mu(i)}^* \underline{f}_{\mu(i)}, \quad (2.36)$$

$$\tau_i = \bar{\mathbf{S}}_i^\top \underline{f}_i. \quad (2.37)$$

Equations (2.32), (2.33) and (2.34) are propagated throughout the kinematic tree with the initial boundary conditions  $\underline{v}_0 = \mathbf{0}$  and  $\underline{a}_0 = -\underline{g}$ , which corresponds to the gravitational spatial acceleration vector expressed in the body frame 0, such that  $\underline{g} = [0 \ 0 \ -9.81 \ 0 \ 0 \ 0]^T$ . Equation (2.35) is exactly the equation of motion for the  $i$ -th body described in (2.28) and represents here the net force acting on the body. Equation (2.36) is the result of a balance of incoming forces (i.e., the internal force  $\underline{f}_i$  transmitted through the  $i$ -th joint, the external force  $\underline{f}_i^x$ ) and outgoing forces (namely, the set of internal forces exchanged with the children bodies) w.r.t. the  $i$ -th link.

---

<sup>2</sup>Except for the external forces that are expressed in the body 0 absolute coordinates.



## Chapter 3

# Human Whole-Body Modelling

*All models are wrong, but some are useful.*

George E. P. Box

In this Chapter a detailed description of the human whole-body modelling is introduced. This is an important step for retrieving the estimation of the human dynamics. The starting point for our analysis is recalled in [Latella et al., 2016] where a simple 2-DoF model was employed for the whole-body modelling. The rough approximation introduced by that model goes without saying and it was useful the ‘upgrade’ to a more complex model able to describe a set of more complex movements.

### 3.1 Human Whole-Body Modelling

By inheriting the robotics-like formalism described in the Section 2.5.1, we propose a human body model as an articulated multi-body system represented by a kinematic tree with  $N_B = 23$  moving links<sup>1</sup> (0 is the fixed base, e.g., the left foot<sup>2</sup>) and  $n = 48$  internal DoFs. The rationale behind the choice of this link number is that we have been guided by the model developed for the Xsens MVN motion capture system [Roetenberg et al., 2009] (Figure 3.1). Since the sensor setup included the Xsens motion capture system, we considered that having two comparable models could be an appropriate choice. This choice is also justified by the fact that the Xsens sensors readings had to be associated to our model.

---

<sup>1</sup>Throughout the thesis, it is often referred to a body as a *link*. The two entities are completely equivalent.

<sup>2</sup>At the current stage, the algorithm used for the human dynamics computation requires a fixed-base model. This motivated our choice to consider the left foot as the fixed base (the human subject performed the experimental tasks with the feet fixed on the ground).



Fig. 3.1 Xsens MVN system representation for the human body model.  
[Source: Xsens, MVN User Manual, 2005.]

Several strong assumptions have been considered in designing our model:

- i)* to represent the human model as a set of rigid links of simple geometric shape (parallelepipeds, cylinders and spheres);
- ii)* to consider density isotropy for each link.

In the following sections, it is provided to the reader a detailed description for each of the above-mentioned assumption by motivating through literature our choice.

### **3.1.1 Inertial Properties Modelling**

Inertial properties of link segments, such as mass, centre of mass or moments of inertia, are important parameters in predicting realistic movement patterns. However, these quantities are not directly measurable. More than a century of literature on this topic proves that the importance in retrieving this information has a pivotal role in studying human dynamics. In [Erdmann, 1999] the author claims that usually in geometric and inertial investigations, three approaches are adopted, by involving living subjects, cadavers and models.

The first investigation (with living subjects) consists in the measurements of the body height and body mass. This type of technique produced over the years well documented anthropometric tables, adopted in the most of inertial studies [Drillis et al., 1964] [Winter, 1990] [Herman, 2007]. These tables correlate the total body mass/height with the mass/height of each link. The second investigation concerns dissections made on cadavers while the model technique is more common in simulation research towards prevention (e.g., car-crash tests).

The author of a more recent study [Robertson, 2013] classifies into two macro-categories the methodologies for estimating body inertial parameters: regression equations models and geometric approximation models. The former technique is based on equations derived from cadaveric measurements, computed radiographs, or magnetic resonance imaging of a finite set of specimens. The author reveals the weakness of this approach since it extrapolates data from an average and has little accuracy for modelling a subject that falls outside the proportions of the initial dataset. The other approach consists of a collection of *in situ* measurements to be mapped into a geometric model to derive mass and properties from certain shape and density assumptions. Here too, the accuracy of the method depends on the complexity of the model and limited to the numbers of measurements. To this purpose, the Hatze model [Hatze, 1980] consists of a 17-segment geometrical model of the body but requires 242 anthropometric measurements, which would imply a relatively substantial amount of time from each subject.

Even if the uniform/non-uniform density assumption is an important part of this analysis (there is an outstanding debate among the scientific community), the complexity and data collection time are the most likely reasons for the lack of the use of Hatze-like model in biomechanical research.

Our approach does not support neither the regression methodology nor the geometrical one. With *i*) we opt for a model of simple shapes and *ii*) offers the possibility of using some analytic formulas to compute the inertial properties of all the segments in the model. Under the assumption of density isotropy [Hanavan, 1964], the inertia tensor  $\mathbf{I}$  has been computed such that

$$\mathbf{I} = \begin{bmatrix} I_{xx} & 0 & 0 \\ 0 & I_{yy} & 0 \\ 0 & 0 & I_{zz} \end{bmatrix}, \quad (3.1)$$

where  $I_{xx}$ ,  $I_{yy}$  and  $I_{zz}$  are the principal moments of inertia. Table 3.1 lists analytical formulas for the principal moments of inertia computation.

Table 3.1 Principal moments of inertia of three different shapes with mass  $m$ : (*on left column*) a rectangular parallelepiped of width  $\alpha$ , height  $\beta$  and depth  $\gamma$ ; (*on middle column*) a circular cylindrical of radius  $r$  and height  $h$ ; (*on right column*) a sphere of radius  $r$ .

Inertia	Parallelepiped	Cylinder	Sphere
$I_{xx}$	$\frac{1}{12}m(\alpha^2 + \beta^2)$	$\frac{1}{12}m(3r^2 + h^2)$	$\frac{2}{5}mr^2$
$I_{yy}$	$\frac{1}{12}m(\beta^2 + \gamma^2)$	$\frac{1}{2}mr^2$	$\frac{2}{5}mr^2$
$I_{zz}$	$\frac{1}{12}m(\gamma^2 + \alpha^2)$	$\frac{1}{12}m(3r^2 + h^2)$	$\frac{2}{5}mr^2$

### 3.1.2 Link Modelling

The labelling of the human model links is inherited by Xsens biomechanical model. For each link, geometry, dimensions, inertial parameters, origin and orientation have to be mandatorily specified. For the *geometry*, the links are modelled as parallelepiped boxes, cylinders and spheres. In order to make the model scalable with the subject proportions, the *dimension* of each shape is obtained via the Xsens IMUs readings<sup>3</sup>. *Inertial parameters* are computed by exploiting the anthropometric table [Winter, 1990] [Herman, 2007]: for retrieving the mass of each link the weight of the subject (and thus  $m_{tot}$ ) is firstly measured and then the mass of each link is obtained by applying tabulated data. Inertia moments are computed as described in Table 3.1. The *origin* and *orientation* of the frame associated to each link are defined in the following way:

<sup>3</sup>Xsens motion capture system provides as inputs 64 bony landmark points distributed all over the model. We exploit the information of their position in the model for delimiting the predominant dimension of the link geometrical shape.

L5	<p><b>origin:</b> midpoint on top-face of the Pelvis parallelepiped  <b>orientation:</b> <math>x</math> pointing forward, <math>z</math> pointing upward (line jL5S1-jL4L3)</p>
L3	<p><b>origin:</b> midpoint on top-face of the L5 parallelepiped  <b>orientation:</b> <math>x</math> pointing forward, <math>z</math> pointing upward (line jL4L3-jL1T12)</p>
T12	<p><b>origin:</b> midpoint on top-face of the L3 parallelepiped  <b>orientation:</b> <math>x</math> pointing forward, <math>z</math> pointing upward (line jL1T12-jT9T8)</p>
T8	<p><b>origin:</b> midpoint on top-face of the T12 parallelepiped  <b>orientation:</b> <math>x</math> pointing forward, <math>z</math> pointing upward (line jT9T8-jT1C7)</p>
Neck	<p><b>origin:</b> midpoint on top-face of the T8 parallelepiped  <b>orientation:</b> <math>x</math> pointing forward, <math>z</math> pointing upward (line jT1C7-jC1Head)</p>
Head	<p><b>origin:</b> midpoint on top-circle of the Neck cylinder  <b>orientation:</b> <math>x</math> pointing forward, <math>z</math> pointing upward (aligned with jT1C7 <math>z</math> axis)</p>
RightUpperLeg	<p><b>origin:</b> midpoint on top-circle of the RightUpperLeg cylinder  <b>orientation:</b> <math>x</math> pointing forward, <math>z</math> pointing upward (line jRightKnee-jRightHip)</p>
RightLowerLeg	<p><b>origin:</b> midpoint on top-circle of the RightLowerLeg cylinder  <b>orientation:</b> <math>x</math> pointing forward, <math>z</math> pointing upward (line jRightAnkle-jRightKnee)</p>
RightFoot	<p><b>origin:</b> point on top-face of the RightFoot parallelepiped  <b>orientation:</b> <math>x</math> pointing forward, <math>z</math> pointing upward (aligned with jRightKnee <math>z</math> axis)</p>
RightToe	<p><b>origin:</b> midpoint on frontal-plane-face (attached to Right-Foot) of the RightToe parallelepiped  <b>orientation:</b> <math>x</math> pointing forward, <math>z</math> pointing upward (aligned with jRightKnee <math>z</math> axis)</p>

LeftUpperLeg	<b>origin:</b> midpoint on top-circle of the LeftUpperLeg cylinder <b>orientation:</b> $x$ pointing forward, $z$ pointing upward (line jLeftKnee-jLeftHip)
LeftLowerLeg	<b>origin:</b> midpoint on top-circle of the LeftLowerLeg cylinder <b>orientation:</b> $x$ pointing forward, $z$ pointing upward (line jLeftAnkle-jLeftKnee)
LeftFoot	<b>origin:</b> point on top-face of the LeftFoot parallelepiped <b>orientation:</b> $x$ pointing forward, $z$ pointing upward (aligned with jLeftKnee $z$ axis)
LeftToe	<b>origin:</b> midpoint on frontal-plane-face (attached to Left-Foot) of the LeftToe parallelepiped <b>orientation:</b> $x$ pointing forward, $z$ pointing upward (aligned with jLeftKnee $z$ axis)
RightShoulder*	<b>origin:</b> midpoint on sagittal-plane-circle (attached to T8) of the RightShoulder cylinder <b>orientation:</b> $x$ pointing forward, $y$ pointing right (line jRightC7Shoulder-jRightShoulder)
RightUpperArm*	<b>origin:</b> midpoint on sagittal-plane-circle (attached to RightShoulder) of the RightUpperArm cylinder <b>orientation:</b> $x$ pointing forward, $y$ pointing right (line jRightShoulder-jRightElbow)
RightForeArm*	<b>origin:</b> midpoint on sagittal-plane-circle (attached to RightUpperArm) of the RightForeArm cylinder <b>orientation:</b> $x$ pointing forward, $y$ pointing right (line jRightElbow-jRightWrist)
RightHand*	<b>origin:</b> midpoint on sagittal-plane-face (attached to Right-ForeArm) of the RightHand parallelepiped <b>orientation:</b> $x$ pointing forward, $y$ pointing right (aligned with jRightElbow $y$ axis)
LeftShoulder*	<b>origin:</b> midpoint on sagittal-plane-circle (attached to T8) of the LeftShoulder cylinder <b>orientation:</b> $x$ pointing forward, $y$ pointing right (line jLeftC7Shoulder-jLeftShoulder)

LeftUpperArm*	<b>origin:</b> midpoint on sagittal-plane-circle (attached to LeftShoulder) of the LeftUpperArm cylinder <b>orientation:</b> $x$ pointing forward, $y$ pointing right (line jLeftShoulder-jLeftElbow)
LeftForeArm*	<b>origin:</b> midpoint on sagittal-plane-circle (attached to LeftUpperArm) of the LeftForeArm cylinder <b>orientation:</b> $x$ pointing forward, $y$ pointing right (line jLeftElbow-jLeftWrist)
LeftHand*	<b>origin:</b> midpoint on sagittal-plane-face (attached to LeftForeArm) of the LeftHand parallelepiped <b>orientation:</b> $x$ pointing forward, $y$ pointing right (aligned with jLeftElbow $y$ axis)

It is worth noting that the frame orientation marked with (\*) is strongly dependent on the choice of the standard initial configuration of the model (T pose, as in Figure B.2). Table 3.3 synthesizes the properties for the link modelling.

### 3.1.3 Joint Modelling

The links are coupled by joints, whose labels are inherited by Xsens joint labelling. Each joint requires information about the motion type (i.e., the joint DoFs), the origin of the frame associated to it and the links connected through it. For the *motion type*, the joints of the model are represented with 1, 2 or 3 DoFs, depending on the anatomy of the relative biological joint. A biological joint is defined as the point where two or more bones articulate. Its functional classification describes the degree of movement allowed between the bones into three anatomical planes: transversal, frontal and sagittal. Thus, the joint motion space is classified as uniaxial (for a movement in one plane), biaxial (for a movement in two planes) or multi-axial joints (for a movement involving three anatomical planes). By classifying the joint motion type, a number of 48 internal DoFs is defined for our modelling. The *origin* of the frame associated to each joint coincides with the origin of the frames associated to the link. Table 3.4 synthesizes the properties for the joint modelling.

Table 3.3 Link properties of the model. The labels reproduce faithfully the Xsens model labels. It is shown for each link the selected shape and the partial mass w.r.t. to the total mass of the subject (extracted from [Winter, 1990]).

<b>Label</b>	<b>Shape</b>	<b>% Mass of <math>m_{tot}</math></b>
Pelvis	parallelepiped	0.08
L5	parallelepiped	0.102
L3	parallelepiped	0.102
T12	parallelepiped	0.102
T8	parallelepiped	0.04
Neck	cylinder	0.012
Head	sphere	0.036
RightShoulder	cylinder	0.031
RightUpperArm	cylinder	0.030
RightForeArm	cylinder	0.020
RightHand	parallelepiped	0.006
LeftShoulder	cylinder	0.031
LeftUpperArm	cylinder	0.030
LeftForeArm	cylinder	0.020
LeftHand	parallelepiped	0.006
RightUpperLeg	cylinder	0.125
RightLowerLeg	cylinder	0.0365
RightFoot	parallelepiped	0.013
RightToe	parallelepiped	0.015
LeftUpperLeg	cylinder	0.125
LeftLowerLeg	cylinder	0.0365
LeftFoot	parallelepiped	0.013
LeftToe	parallelepiped	0.0015

Table 3.4 Joint properties of the model: labels (inherited from Xsens labelling), DoFs per each joint and the links connected through it.

Label	DoF	Connected links
jL5S1	2	Pelvis ↔ L5
jL4L3	2	L5 ↔ L3
jL1T12	2	L3 ↔ T12
jT9T8	3	T12 ↔ T8
jT1C7	3	T8 ↔ Neck
jC1Head	2	Neck ↔ Head
jRightHip	3	Pelvis ↔ RightUpperLeg
jRightKnee	2	RightUpperLeg ↔ RightLowerLeg
jRightAnkle	3	RightLowerLeg ↔ RightFoot
jRightBallFoot	1	RightFoot ↔ RightToe
jLeftHip	3	Pelvis ↔ LeftUpperLeg
jLeftKnee	2	LeftUpperLeg ↔ LeftLowerLeg
jLeftAnkle	3	LeftLowerLeg ↔ LeftFoot
jLeftBallFoot	1	LeftFoot ↔ LeftToe
jRightC7Shoulder	1	T8 ↔ RightShoulder
jRightShoulder	3	RightShoulder ↔ RightUpperArm
jRightElbow	2	RightUpperArm ↔ RightForeArm
jRightWrist	2	RightForeArm ↔ RightHand
jLeftC7Shoulder	1	T8 ↔ LeftShoulder
jLeftShoulder	3	LeftShoulder ↔ LeftUpperArm
jLeftElbow	2	LeftUpperArm ↔ LeftForeArm
jLeftWrist	2	LeftForeArm ↔ LeftHand

## 3.2 The Human URDF Model

The Unified Robot Description Format (URDF) representation is very common among the robotics community but not widespread among that part of community that deals with human modelling. The reason is quite clear: this format is particularly tailored for describing robots (e.g., the typical specification assumes rigid links) and it does not take into account the presence of muscles in the model (no flexible or shape-variable links are supported). However, two main reasons led us to this choice:

- 1) the possibility offered by this format of creating a valid representation for complex tree structures,
- 2) the possibility of handling both the models for the human and for the robot with the same formalism.

See Appendix B for a detailed description on how to build the human URDF model.

### 3.2.1 Sensor Pose Estimation

In order to perform the estimation of the human dynamics, the information about the Xsens IMUs has to be embedded in the URDF model. However, the pose of the sensor w.r.t. the attached link is not provided by Xsens as an output of the system. Therefore, in this Section a procedure for estimating the sensor position by exploiting IMUs linear acceleration and angular velocity is proposed. The procedure is very similar to [Rotella et al., 2016] where it is used for a humanoid robot.

#### Estimation Procedure

Let  $\mathcal{I}$  be an inertial frame and consider a generic rigid body. We define the body reference frame  $\mathcal{B}$  identifying its pose w.r.t.  $\mathcal{I}$  (Figure 3.2). Consider also a sensor rigidly attached to the rigid body and its reference frame  $\mathcal{S}$ . Let  ${}^{\mathcal{I}}\mathbf{g} \in \mathbb{R}^3$  be the gravity acceleration vector expressed in  $\mathcal{I}$ . The estimation problem can be summarized as follows.

#### The problem

*Given the pose  $(\mathbf{p}_{\mathcal{B}}, \mathbf{R}_{\mathcal{B}})$ , the linear acceleration  $\ddot{\mathbf{p}}_{\mathcal{B}}$ , the angular velocity  $\boldsymbol{\omega}$  and acceleration  $\dot{\boldsymbol{\omega}}$  of  $\mathcal{B}$  w.r.t.  $\mathcal{I}$ , the orientation  $\mathbf{R}_{\mathcal{S}}$  and the proper acceleration  $\mathbf{a}$  of  $\mathcal{S}$  w.r.t.  $\mathcal{I}$ , estimate the relative pose of  $\mathcal{S}$  w.r.t.  $\mathcal{B}$ , i.e., the position vector  ${}^{\mathcal{B}}\mathbf{p}_{\mathcal{S}} \in \mathbb{R}^3$  and the orientation  ${}^{\mathcal{B}}\mathbf{R}_{\mathcal{S}} \in SO(3)$ .*

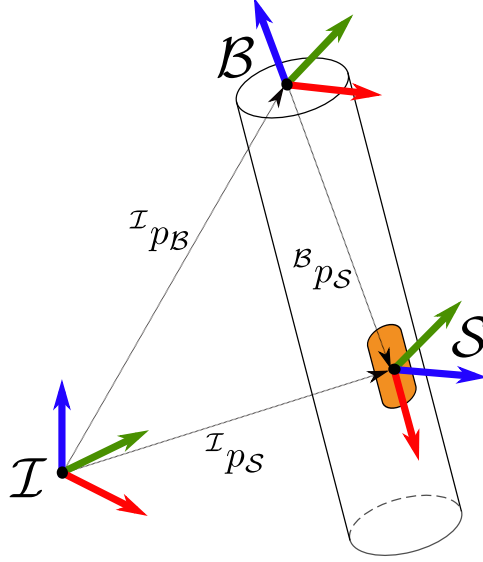


Fig. 3.2 Rigid body identified by the frame  $\mathcal{B}$  with a sensor (identified by the frame  $\mathcal{S}$ ) rigidly attached on it.

The relative orientation between the sensor and the link can be easily obtained by the following equation:

$${}^{\mathcal{B}}\mathbf{R}_{\mathcal{S}} = {}^{\mathcal{I}}\mathbf{R}_{\mathcal{B}}^{\top} {}^{\mathcal{I}}\mathbf{R}_{\mathcal{S}} . \quad (3.2)$$

To estimate the relative position, consider the measurement equation:

$$\begin{aligned} {}^{\mathcal{S}}\mathbf{a} &= {}^{\mathcal{S}}\mathbf{R}_{\mathcal{I}} \left( {}^{\mathcal{I}}\ddot{\mathbf{p}}_{\mathcal{S}} - {}^{\mathcal{I}}\mathbf{g} \right) \\ &= {}^{\mathcal{S}}\mathbf{R}_{\mathcal{I}} \left[ {}^{\mathcal{I}}\ddot{\mathbf{p}}_{\mathcal{B}} + \dot{\boldsymbol{\omega}} \times {}^{\mathcal{I}}\mathbf{R}_{\mathcal{B}} {}^{\mathcal{B}}\mathbf{p}_{\mathcal{S}} + \boldsymbol{\omega} \times \left( \boldsymbol{\omega} \times {}^{\mathcal{I}}\mathbf{R}_{\mathcal{B}} {}^{\mathcal{B}}\mathbf{p}_{\mathcal{S}} \right) - {}^{\mathcal{I}}\mathbf{g} \right] \\ &= {}^{\mathcal{S}}\mathbf{R}_{\mathcal{I}} \left[ {}^{\mathcal{I}}\ddot{\mathbf{p}}_{\mathcal{B}} + \left( \mathbf{S}(\dot{\boldsymbol{\omega}}) + \mathbf{S}(\boldsymbol{\omega})^2 \right) {}^{\mathcal{I}}\mathbf{R}_{\mathcal{B}} {}^{\mathcal{B}}\mathbf{p}_{\mathcal{S}} - {}^{\mathcal{I}}\mathbf{g} \right] , \end{aligned} \quad (3.3)$$

where  $\mathbf{S}(\boldsymbol{\omega}) = {}^{\mathcal{I}}\dot{\mathbf{R}}_{\mathcal{B}} {}^{\mathcal{B}}\mathbf{R}_{\mathcal{I}}$ , from (2.9).

To estimate  ${}^{\mathcal{B}}\mathbf{p}_{\mathcal{S}}$  we have to solve Equation (3.3). Given that measurements may be affected by errors, it is impractical to solve it with only one measurement. To estimate  ${}^{\mathcal{B}}\mathbf{p}_{\mathcal{S}}$  we thus collect multiple measurements and solve the resulting overdetermined system in the least-squares sense. We first rewrite (3.3) in the following form:

$$\underbrace{\left( \mathbf{S}(\dot{\boldsymbol{\omega}}) + \mathbf{S}(\boldsymbol{\omega})^2 \right) {}^{\mathcal{I}}\mathbf{R}_{\mathcal{B}} {}^{\mathcal{B}}\mathbf{p}_{\mathcal{S}}}_{\mathbf{A}} = \underbrace{{}^{\mathcal{I}}\mathbf{R}_{\mathcal{S}} {}^{\mathcal{S}}\mathbf{a} - \left( {}^{\mathcal{I}}\ddot{\mathbf{p}}_{\mathcal{B}} - {}^{\mathcal{I}}\mathbf{g} \right)}_{\mathbf{b}} . \quad (3.4)$$

By denoting with  $\mathbf{A}_i$  and  $\mathbf{b}_i$  the matrices  $\mathbf{A}$  and  $\mathbf{b}$  associated with the  $i$ -th measurement, after collecting  $N$  measurements we obtain the following linear system:

$$\begin{bmatrix} \mathbf{A}_1 \\ \vdots \\ \mathbf{A}_N \end{bmatrix} {}^{\mathcal{B}}\mathbf{p}_S = \begin{bmatrix} \mathbf{b}_1 \\ \vdots \\ \mathbf{b}_N \end{bmatrix}, \quad (3.5)$$

thus

$$\bar{\mathbf{A}} {}^{\mathcal{B}}\mathbf{p}_S = \bar{\mathbf{b}}, \quad (3.6)$$

$${}^{\mathcal{B}}\mathbf{p}_S = \bar{\mathbf{A}}^\dagger \bar{\mathbf{b}}, \quad (3.7)$$

where  $\bar{\mathbf{A}}^\dagger = (\bar{\mathbf{A}}^\top \bar{\mathbf{A}})^{-1} \bar{\mathbf{A}}^\top$  denotes the Moore-Penrose pseudoinverse of  $\bar{\mathbf{A}}$ . Equations (3.7) and (3.2) identify the relative pose of  $\mathcal{S}$  w.r.t.  $\mathcal{B}$ . In the Algorithm 1 the pseudocode for the procedure of sensor position estimation is shown.

---

**Algorithm 1** Compute sensor pose, Equation (3.7)

---

```

1: procedure SENSORPOSEESTIMATION
2:    $N \leftarrow$  number of samples
3:    $N_{IMU} \leftarrow$  number of IMUs, 17
4:   main loop:
5:     for  $j = 1 \rightarrow N_{IMU}$  do
6:       nested loop:
7:         for  $i = 1 \rightarrow N$  do
8:            $\Rightarrow$  compute  $\mathbf{A}_i$ :
9:            $\mathbf{A}_i = \left( \mathbf{S}(\dot{\boldsymbol{\omega}}) + \mathbf{S}(\boldsymbol{\omega})^2 \right) {}^{\mathcal{I}}\mathbf{R}_{\mathcal{B}} \Big|_i$ 
10:           $\Rightarrow$  compute  $\mathbf{b}_i$ :
11:           $\mathbf{b}_i = {}^{\mathcal{I}}\mathbf{R}_S^{\mathcal{S}} \mathbf{a} - \left( {}^{\mathcal{I}}\ddot{\mathbf{p}}_{\mathcal{B}} - {}^{\mathcal{I}}\mathbf{g} \right) \Big|_i$ 
12:           $\Rightarrow$  compute  $\text{RPY}_i$ :
13:           ${}^{\mathcal{B}}\mathbf{R}_S \Big|_i = {}^{\mathcal{I}}\mathbf{R}_{\mathcal{B}}^\top {}^{\mathcal{I}}\mathbf{R}_S$  as RPY
14:        goto nested loop.
15:      end
16:       $\Rightarrow$  compute  ${}^{\mathcal{B}}\mathbf{p}_S$ :
17:       ${}^{\mathcal{B}}\mathbf{p}_S = \mathbf{A} \setminus \mathbf{b}$ 
18:       $\Rightarrow$  compute  $\text{RPY}$ :
19:       ${}^{\mathcal{B}}\mathbf{R}_S = \text{mean}(\text{RPY}_i)$ 
20:    goto main loop.
21:  end

```

---

A URDF model for the 48-DoF human template is shown in Figure 3.3. The figure shows the 17 IMUs distributed on the body.

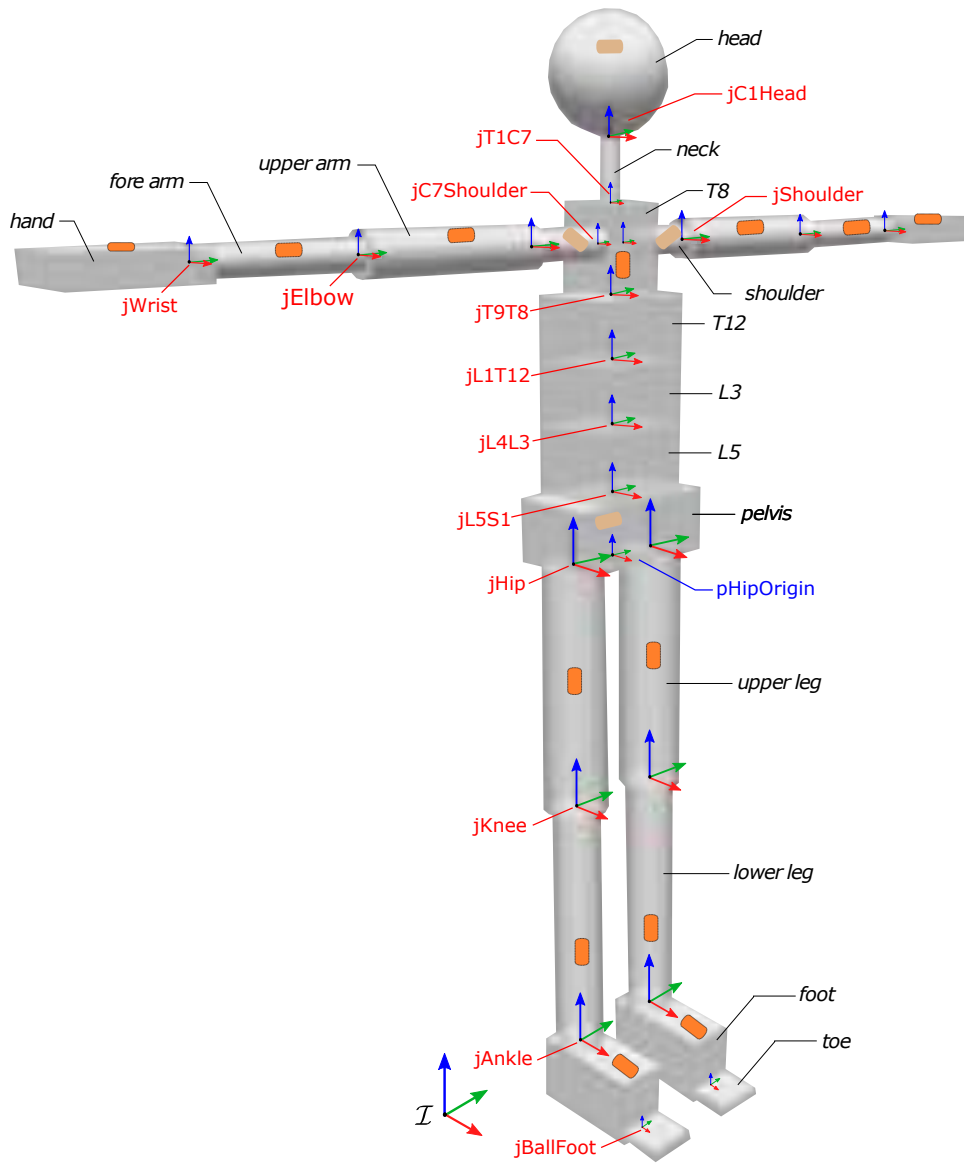


Fig. 3.3 URDF human body model with 17 IMUs distributed along the body. Their pose is estimated via IMUs readings by applying the estimation procedure of Algorithm 1.



## Chapter 4

# The Human Dynamics Estimation Problem: a Probabilistic Solution

*No great discovery was ever made without a bold guess.*

Isaac Newton

In this Chapter, the estimation problem for the human dynamics is investigated. As recalled in Section 1.2.1, the procedure for computing the joint torques  $\boldsymbol{\tau}$  given the joint accelerations  $\ddot{\boldsymbol{q}}$  and the external forces  $\boldsymbol{f}^x$  acting on a kinematic tree model is the well-known identified problem of the inverse dynamics. In [Featherstone, 2007], the problem is formulated as follows:

$$\boldsymbol{\tau} = \text{ID}(\text{model}, \boldsymbol{q}, \dot{\boldsymbol{q}}, \ddot{\boldsymbol{q}}, \boldsymbol{f}^x) . \quad (4.1)$$

A classical and computationally efficient solution for the ID problem is the RNEA (presented in Section 2.5.3) which also computes the internal forces  $\boldsymbol{f}$  and the link accelerations  $\boldsymbol{a}$ .

We perform here a different choice which encompasses the computation of other human variables (in a new vector  $\boldsymbol{d}$ ) in a probabilistic domain and includes the sensors measurements (defined in a new vector  $\boldsymbol{y}$ ). The problem in (4.1) could be therefore written in the form

$$\boldsymbol{d} = \text{MAPD}(\text{model}, \boldsymbol{q}, \dot{\boldsymbol{q}}, \ddot{\boldsymbol{q}}, \boldsymbol{y}) , \quad (4.2)$$

where

- the torques  $\boldsymbol{\tau}$  of (4.1) are embedded in a new vector  $\boldsymbol{d}$ ,
- the external forces  $\boldsymbol{f}^x$  used as input in (4.1) are embedded in a new vector of measurements  $\boldsymbol{y}$ .

A detailed explanation for the new quantities will follow in Sections 4.1 and 4.2, respectively.

Clearly, there is an unquestionably strong parallelism with the problem (4.1) and over this Chapter it is explained how the classical robotics formalism has been adapted to fit the needs of the human dynamics framework. The Chapter provides the reader with a detailed description of the methodology used for solving the estimation problem whose novelty lies in considering simultaneously the fusion of different sensors information.

## 4.1 The System Constraints Formulation

Given a suitable model for the human, as in Chapter 3, it is convenient to define a new vector quantity  $\mathbf{d}$  containing variables for describing both the kinematics and the dynamics of the model, with  $N_B$  number of bodies and  $n$  internal DoFs number. If  $i = 1 : N_B$ , the vector  $\mathbf{d}$  is such that

$$\mathbf{d} = [\mathbf{d}_1^\top \quad \mathbf{d}_2^\top \quad \dots \quad \mathbf{d}_{N_B}^\top]^\top \in \mathbb{R}^{24N_B+2n}, \quad (4.3)$$

where

$$\mathbf{d}_i = [\underline{\mathbf{a}}_i^\top \quad \underline{\mathbf{f}}_i^{B\top} \quad \underline{\mathbf{f}}_i^\top \quad \tau_i \quad \underline{\mathbf{f}}_i^{x\top} \quad \ddot{q}_i]^\top \in \mathbb{R}^{24+2n_i}. \quad (4.4)$$

It is worth remarking that  $\mathbf{d}$  is a *hybrid* vector that, by construction, contains quantity related to the  $i$ -th link (i.e., the acceleration  $\underline{\mathbf{a}}_i$ , the net force  $\underline{\mathbf{f}}_i^B$  and the external force  $\underline{\mathbf{f}}_i^x$ ) and the  $i$ -th joint (i.e., the force exchanged through the joint  $\underline{\mathbf{f}}_i$ , the joint torque  $\tau_i$  and the joint acceleration  $\ddot{q}_i$ ).

If the Newton-Euler formalism is properly rearranged in a matrix form, thus Equations (2.34)-(2.37) can be considered as a set of linear constraint equations that  $\mathbf{d}$  has to satisfy. Given (4.3) and (4.4), Equations (2.34)-(2.37) can be compactly written in the following matrix equation representing the constraints of the system:

$$\mathbf{D}(\mathbf{q}, \dot{\mathbf{q}})\mathbf{d} + \mathbf{b}_D(\mathbf{q}, \dot{\mathbf{q}}) = \mathbf{0}, \quad (4.5)$$

where  $\mathbf{D}$  is a block matrix  $\in \mathbb{R}^{(18N_B+n) \times d}$  and  $\mathbf{b}_D$  is a vector  $\in \mathbb{R}^{18N_B+n}$ , as follows<sup>1</sup>:

---

<sup>1</sup>Note on the notation: it is referred here to  $\mathbf{D} \in \mathbb{R}^{(18N_B+n) \times d}$ . Within this notation  $\mathbf{D}$  is a matrix with  $(18N_B+n)$  rows and  $d$  columns, i.e., number of rows of  $\mathbf{d}$  (4.3), namely  $(24N_B+2n)$ . This form will be recurring throughout the thesis.

$$\mathbf{D} = \begin{bmatrix} \mathbf{D}_{1,1} & \cdots & \mathbf{D}_{1,N_B} \\ \vdots & \ddots & \vdots \\ \mathbf{D}_{N_B,1} & \cdots & \mathbf{D}_{N_B,N_B} \end{bmatrix}, \quad \mathbf{b}_D = \begin{bmatrix} \mathbf{b}_1 \\ \vdots \\ \mathbf{b}_{N_B} \end{bmatrix}.$$

More in detail:

$$\mathbf{D}_{i,i} = \begin{bmatrix} -1 & \mathbf{0} & \mathbf{0} & \mathbf{0} & \mathbf{0} & \bar{\mathbf{S}}_i \\ \mathbf{I}_i & -1 & \mathbf{0} & \mathbf{0} & \mathbf{0} & \mathbf{0} \\ \mathbf{0} & \mathbf{1} & -1 & \mathbf{0} & -{}^i\mathbf{X}_0^* & \mathbf{0} \\ \mathbf{0} & \mathbf{0} & \bar{\mathbf{S}}_i^\top & -1 & \mathbf{0} & \mathbf{0} \end{bmatrix}, \quad (4.6)$$

$$\forall \mu(i) \quad \mathbf{D}_{i,\mu(i)} = \begin{bmatrix} \mathbf{0} & \mathbf{0} & \mathbf{0} & \mathbf{0} & \mathbf{0} & \mathbf{0} \\ \mathbf{0} & \mathbf{0} & \mathbf{0} & \mathbf{0} & \mathbf{0} & \mathbf{0} \\ \mathbf{0} & \mathbf{0} & {}^i\mathbf{X}_{\mu(i)}^* & \mathbf{0} & \mathbf{0} & \mathbf{0} \\ \mathbf{0} & \mathbf{0} & \mathbf{0} & \mathbf{0} & \mathbf{0} & \mathbf{0} \end{bmatrix}, \quad (4.7)$$

$$\forall \lambda(i) \quad \mathbf{D}_{i,\lambda(i)} = \begin{bmatrix} {}^i\mathbf{X}_{\lambda(i)} & \mathbf{0} & \mathbf{0} & \mathbf{0} & \mathbf{0} & \mathbf{0} \\ \mathbf{0} & \mathbf{0} & \mathbf{0} & \mathbf{0} & \mathbf{0} & \mathbf{0} \\ \mathbf{0} & \mathbf{0} & \mathbf{0} & \mathbf{0} & \mathbf{0} & \mathbf{0} \\ \mathbf{0} & \mathbf{0} & \mathbf{0} & \mathbf{0} & \mathbf{0} & \mathbf{0} \end{bmatrix}, \quad (4.8)$$

$$\text{if } \lambda(i) = 0 \quad \mathbf{b}_i = \begin{bmatrix} {}^i\mathbf{X}_0 \underline{\mathbf{a}}_0 + \underline{\mathbf{v}}_i \times \bar{\mathbf{S}}_i \dot{q}_i \\ \underline{\mathbf{v}}_i \times {}^* \mathbf{I}_i \underline{\mathbf{v}}_i \\ \mathbf{0} \\ \mathbf{0} \end{bmatrix}, \quad (4.9)$$

$$\text{if } \lambda(i) \neq 0 \quad \mathbf{b}_i = \begin{bmatrix} \underline{\mathbf{v}}_i \times \bar{\mathbf{S}}_i \dot{q}_i \\ \underline{\mathbf{v}}_i \times {}^* \mathbf{I}_i \underline{\mathbf{v}}_i \\ \mathbf{0} \\ \mathbf{0} \end{bmatrix}. \quad (4.10)$$

### 4.1.1 Considerations on the Representation

Equation (4.5) is an equivalent representation of (2.31). The Lagrangian formulation can be obtained from Equation (4.5) as hereafter described. First, the vector  $\mathbf{d}$  and the columns of  $\mathbf{D}$  should be rearranged so that they respect the following order:  $\underline{\mathbf{a}}_1 \dots \underline{\mathbf{a}}_{N_B}$ ,  $\underline{\mathbf{f}}_1^B \dots \underline{\mathbf{f}}_{N_B}^B$ ,  $\underline{\mathbf{f}}_1 \dots \underline{\mathbf{f}}_{N_B}$ ,  $\ddot{\mathbf{q}}_1 \dots \ddot{\mathbf{q}}_{N_B}$ ,  $\underline{\mathbf{f}}_1^x \dots \underline{\mathbf{f}}_{N_B}^x$  and  $\tau_1 \dots \tau_{N_B}$ . The resulting  $\mathbf{D}$  and  $\mathbf{b}$  are:

$$\begin{aligned} & \text{Equations (2.34)–(2.36)} \left\{ \left[ \begin{array}{cc|cc} \overbrace{\mathbf{a}, \mathbf{f}, \mathbf{f}_B} & \overbrace{\ddot{\mathbf{q}}, \mathbf{f}^x, \tau} & & \\ \mathbf{D}_{\mathbf{a}, \mathbf{f}, \mathbf{f}_B} & \mathbf{D}_{\ddot{\mathbf{q}}} & \mathbf{D}_{\mathbf{f}^x} & \mathbf{D}_{\tau} \end{array} \right] \right. \\ & \text{Equations (2.37)} \left\{ \left[ \begin{array}{cc|cc} \mathbf{D}_{\mathbf{a}, \mathbf{f}, \mathbf{f}_B} & \mathbf{D}_{\ddot{\mathbf{q}}} & \mathbf{D}_{\mathbf{f}^x} & \mathbf{D}_{\tau} \end{array} \right] \right. \end{aligned} \quad (4.11)$$

$$\begin{aligned} & \text{Equations (2.34)–(2.36)} \left\{ \left[ \begin{array}{c} \mathbf{b}_D \end{array} \right] \right. \\ & \text{Equations (2.37)} \left\{ \left[ \begin{array}{c} \mathbf{b}_D \end{array} \right] \right. \end{aligned} \quad (4.12)$$

Within this rearrangement, Equation (2.31) can be obtained as follows:

$$\begin{aligned} & \mathbf{D}_{\mathbf{a}, \mathbf{f}, \mathbf{f}_B}^{(2.37)} \left\{ \left[ \mathbf{D}_{\mathbf{a}, \mathbf{f}, \mathbf{f}_B}^{(2.34)–(2.36)} \right]^{-1} \right. \\ & \left. \left[ -\mathbf{b}_D^{(2.34)–(2.36)} - \mathbf{D}_{\ddot{\mathbf{q}}}^{(2.34)–(2.36)} \ddot{\mathbf{q}} - \mathbf{D}_{\mathbf{f}^x}^{(2.34)–(2.36)} \mathbf{f}^x - \mathbf{D}_{\tau}^{(2.34)–(2.36)} \tau \right] \right\} \\ & + \mathbf{D}_{\ddot{\mathbf{q}}}^{(2.37)} \ddot{\mathbf{q}} + \mathbf{D}_{\mathbf{f}^x}^{(2.37)} \mathbf{f}^x + \mathbf{D}_{\tau}^{(2.37)} \tau + \mathbf{b}_D^{(2.37)} = \mathbf{0}. \end{aligned} \quad (4.13)$$

In the human dynamics estimation problem, the choice for preferring (4.5) formulation to (2.31) is two-fold. On the one hand, Equation (4.5) can be used to represent uncertainties that capture relevant modeling approximations. In particular, approximations result from the fact that human bones coupling is neither rigid nor purely rotational and these can be captured with additive noise on Equations (2.34)–(2.37). On the other hand, there are numerical advantages associated to Equation (4.5). In the case of inverse and forward dynamics, the numerical advantages are exactly those obtained by the RNEA presented in [Featherstone, 2007] and whose relations to Equation (4.5) is discussed in [Nori et al., 2015].

## 4.2 The Measurements Equation

Let  $\mathbf{y} \in \mathbb{R}^y$  be the vector containing all the available sensors readings. The explicit equation for the measurements is such that

$$\mathbf{Y}(\mathbf{q}, \dot{\mathbf{q}})\mathbf{d} + \mathbf{b}_Y(\mathbf{q}, \dot{\mathbf{q}}) = \mathbf{y} . \quad (4.14)$$

The structure of the  $\mathbf{Y}$  matrix depends on how many sensors are considered in the analysis and it is independent from the number of link  $N_B$  in the model (more sensors could be associated to the same link, e.g., a combination of an IMU + a force sensor). If  $i = 1 : N_S$  number of sensors, thus  $\mathbf{Y}$  is a block matrix  $\in \mathbb{R}^{N_S \times d}$

$$\mathbf{Y} = [\mathbf{Y}_1 \quad \mathbf{Y}_2 \quad \dots \quad \mathbf{Y}_{N_S}]^\top \in \mathbb{R}^{N_S \times d} , \quad (4.15)$$

where the dimension of each block depends from the type of sensor. Similarly, the bias vector  $\mathbf{b}_Y$  is such that

$$\mathbf{b}_Y = [\mathbf{b}_{Y_1} \quad \mathbf{b}_{Y_2} \quad \dots \quad \mathbf{b}_{Y_{N_S}}]^\top \in \mathbb{R}^{N_S} . \quad (4.16)$$

### 4.2.1 An Illustrative Example

Hereafter, an illustrative example on the measurements equation is provided. Consider the generic 2-DoF model depicted in Figure 4.1. Suppose now that the model is standing on a force plate (in rigid contact with link 0) that provides a measurement of the force that the model is exchanging with the ground. Furthermore, an IMU is positioned on link 2.  $\mathbf{f}_1^x$  and  $\mathbf{f}_2^x$  represent possible external forces acting on the links. In this specific example

$$\mathbf{d} = [\mathbf{d}_1^\top \quad \mathbf{d}_2^\top]^\top \in \mathbb{R}^{52} , \quad (4.17)$$

and the set of equations related to the IMU and the force plate sensors on the fixed base (i.e.,  $fb$ ) are, respectively, the following:

$$\mathbf{y}_{2,IMU} = ({}^{IMU}\mathbf{X}_2\mathbf{a}_2)_{lin} + ({}^{IMU}\mathbf{X}_2\mathbf{v}_2)_{ang} \times ({}^{IMU}\mathbf{X}_2\mathbf{v}_2)_{lin} , \quad (4.18)$$

$$\mathbf{y}_{f_{FP,fb}^x} = {}^{FP}\mathbf{X}_0^* \left( {}^0\mathbf{X}_1^* \mathbf{f}_1 - \mathbf{I}_0 \mathbf{g} \right) . \quad (4.19)$$

See Equation (A.14) in Appendix A for retrieving Equation (4.19) , being  $\mathbf{a}_0 = -\mathbf{g}$  and  $\mathbf{v}_0 = \mathbf{0}$ .

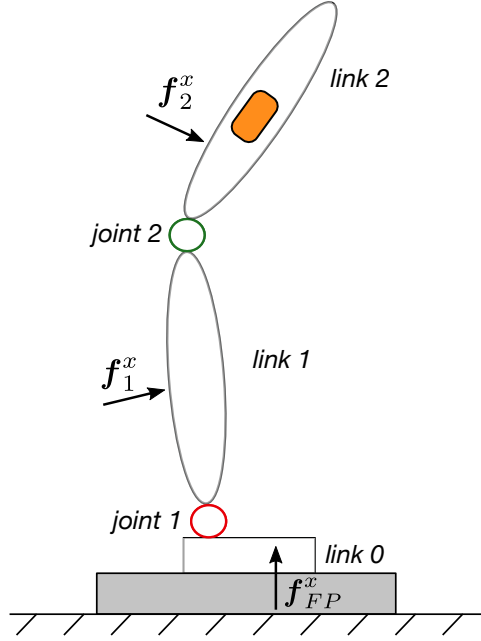


Fig. 4.1 Representation of a 2-DoF model standing on a force plate (in grey), with an IMU (in orange) positioned on link 2, and external forces  $f_{FP}^x$ ,  $f_1^x$ ,  $f_2^x$  acting on it.

Consider now to define the measurement equation (4.14) for this example. The algorithm that solves the human dynamics estimation (explained in the following sections) requires mandatorily to specify in the vector  $\mathbf{y}$  the following measurements:

- the linear acceleration for those links where an IMU is attached (e.g.,  $\mathbf{y}_{2,IMU}$ );
- the acceleration of all the joints of the model<sup>2</sup> (e.g.,  $y_{\ddot{q}_1}$ ,  $y_{\ddot{q}_2}$ );
- the force on the fixed base measured by the force plate or similar (e.g.,  $\mathbf{y}_{f_{FP,fb}^x}$ );
- the external force acting on all the links of the model<sup>3</sup> (e.g.,  $\mathbf{y}_{f_1^x}$ ,  $\mathbf{y}_{f_2^x}$ ).

This yields to a vector  $\mathbf{y}$  such that

$$\mathbf{y} = \left[ \mathbf{y}_{2,IMU} \quad y_{\ddot{q}_1} \quad y_{\ddot{q}_2} \quad \mathbf{y}_{f_{FP,fb}^x} \quad \mathbf{y}_{f_1^x} \quad \mathbf{y}_{f_2^x} \right]^T \in \mathbb{R}^{23}. \quad (4.20)$$

<sup>2</sup>Class of fictitious DoF-acceleration sensors.

<sup>3</sup>If any external force is acting on a link, the external force measurement for that link is a vector  $\in \mathbb{R}^6$  with entries equal to 0.

It is possible now to write down the measurements equation (4.14) as follows:

$$\begin{bmatrix}
 0 & 0 & 0 & 0 & 0 & 0 & (IMU \mathbf{X}_2)_{lin} & \dots & 0 & 0 \\
 0 & 0 & 0 & 0 & 0 & 1 & 0 & \dots & 0 & 0 \\
 0 & 0 & 0 & 0 & 0 & 0 & 0 & \dots & 0 & 1 \\
 0 & 0 & {}^{FP} \mathbf{X}_0^* \mathbf{X}_1^* & 0 & 0 & 0 & 0 & \dots & 0 & 0 \\
 0 & 0 & 0 & 0 & \mathbf{1}_6 & 0 & 0 & \dots & 0 & 0 \\
 0 & 0 & 0 & 0 & 0 & 0 & 0 & \dots & \mathbf{1}_6 & 0
 \end{bmatrix}
 \begin{bmatrix}
 \underline{a}_1 \\
 \underline{f}_1^B \\
 \underline{f}_1 \\
 \tau_1 \\
 \underline{f}_1^x \\
 \underline{\dot{q}}_1 \\
 \underline{a}_2 \\
 \underline{f}_2^B \\
 \underline{f}_2 \\
 \tau_2 \\
 \underline{f}_2^x \\
 \underline{\dot{q}}_2
 \end{bmatrix}
 +
 \begin{bmatrix}
 (IMU \mathbf{X}_2 \mathbf{v}_2)_{ang} \times (IMU \mathbf{X}_2 \mathbf{v}_2)_{lin} \\
 0 \\
 0 \\
 - {}^{FP} \mathbf{X}_0^* \mathbf{I}_0 \underline{g} \\
 0 \\
 0
 \end{bmatrix}
 =
 \begin{bmatrix}
 \mathbf{y}_{2,IMU} \\
 y_{\dot{q}_1} \\
 y_{\dot{q}_2} \\
 \mathbf{y}_{f_{FP,fb}^x} \\
 \mathbf{y}_{f_1^x} \\
 \mathbf{y}_{f_2^x}
 \end{bmatrix}
 \quad .(4.21)$$

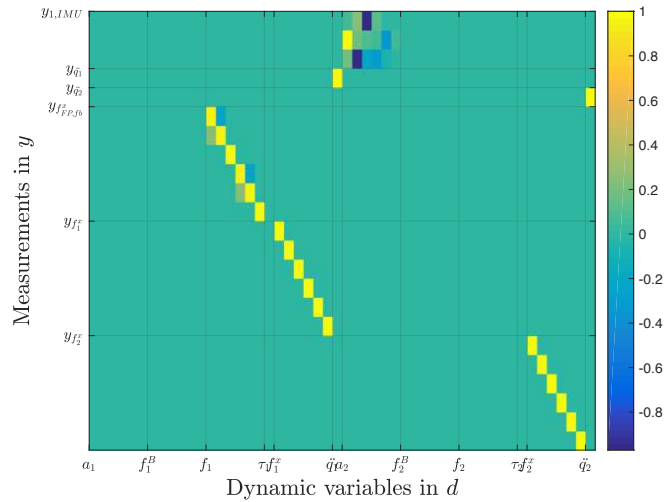


Fig. 4.2 Example of  $\mathbf{Y}$  matrix for the Equation (4.21).

### 4.3 The Estimation Problem Formulation

By stacking together the Equations (4.5) and (4.14), we obtain the following system of equations:

$$\begin{bmatrix} \mathbf{Y}(\mathbf{q}, \dot{\mathbf{q}}) \\ \mathbf{D}(\mathbf{q}, \dot{\mathbf{q}}) \end{bmatrix} \mathbf{d} + \begin{bmatrix} \mathbf{b}_Y(\mathbf{q}, \dot{\mathbf{q}}) \\ \mathbf{b}_D(\mathbf{q}, \dot{\mathbf{q}}) \end{bmatrix} = \begin{bmatrix} \mathbf{y} \\ \mathbf{0} \end{bmatrix}, \quad (4.22)$$

$$\text{rank} \left( \begin{bmatrix} \mathbf{Y}(\mathbf{q}, \dot{\mathbf{q}}) \\ \mathbf{D}(\mathbf{q}, \dot{\mathbf{q}}) \end{bmatrix} \right) = d. \quad (4.23)$$

The bottom part of (4.22) represents the constraints equation in (4.5), while the upper part contains the information coming from the, possibly noisy or redundant, sensors. It is possible to compute the whole-body dynamics estimation by solving the system in  $\mathbf{d}$ . The assumption on the rank in (4.23) guarantees that the available measurements  $\mathbf{y}$  give enough constraints on  $\mathbf{d}$ .

The novelty of the framework lies in moving away from the classical approach by replacing RNEA boundary conditions with measurements coming from sensors. Within this new framework, there are situations in which the system is overdetermined and an exact solution does not exist. An ‘approximated’ solution can be obtained only by making some additional hypothesis. If there is a valid reason to assume that all the constraints have equal relevance and all measurements the same accuracy, one possible approach is to solve (4.22) in the ordinary least-squares sense, by using a Moore-Penrose pseudoinverse. Otherwise, if we have good reasons for weighting differently the constraints and the sensors readings, we can use the weighted pseudoinverse to obtain a weighted least-squares solution. However, finding proper weights might be not an easy task.

In this thesis a different choice is performed: given the prior knowledge of the measurements  $\mathbf{y}$  and the prior information about the constraints of the model, the estimation of  $\mathbf{d}$  is framed in a Gaussian domain by means of a maximum-a-posteriori estimator.

### 4.4 Probabilistic Preliminaries

Since the estimation problem solution is framed in a Gaussian domain, some basic notations related to the probability theory are here recalled.

- Given a stochastic variable  $\mathbf{x}$ , let  $p(\mathbf{x})$  be its probability density distribution and  $p(\mathbf{x}|\mathbf{y})$  the conditional probability distribution of  $\mathbf{x}$  given the assumption that another stochastic variable  $\mathbf{y}$  has occurred.
- Given  $\mathbf{x}$  and  $\mathbf{y}$ , let  $p(\mathbf{x}, \mathbf{y}) = p(\mathbf{x})p(\mathbf{y}|\mathbf{x})$  be their joint probability distribution.
- If  $\mathbf{y}$  is associated to a deterministic function  $f(\mathbf{x})$ , let  $E_{\mathbf{x}}[f(\mathbf{x})]$  be the expected value of  $f(\mathbf{x})$  w.r.t.  $p(\mathbf{x})$ . Let  $\boldsymbol{\mu}_{\mathbf{x}}$  be the mean of  $\mathbf{x}$ , i.e.,  $\boldsymbol{\mu}_{\mathbf{x}} = E[\mathbf{x}]$  and  $\boldsymbol{\Sigma}_{\mathbf{x}}$  the covariance associated to  $\mathbf{x}$ , such that  $\boldsymbol{\Sigma}_{\mathbf{x}} = cov[\mathbf{x}] = E[\mathbf{x}\mathbf{x}^{\top}]$ .

- Given a multivariate Gaussian distribution  $\mathbf{x} \in \mathbb{R}^n$ , expressed with the notation

$$\mathbf{x} \sim \mathcal{N}(\boldsymbol{\mu}_{\mathbf{x}}, \boldsymbol{\Sigma}_{\mathbf{x}}), \quad (4.24)$$

its probability density function (PDF) is

$$p(\mathbf{x}) = (2\pi)^{-\frac{n}{2}} |\boldsymbol{\Sigma}_{\mathbf{x}}|^{-\frac{1}{2}} \exp -\frac{1}{2} \left\{ (\mathbf{x} - \boldsymbol{\mu}_{\mathbf{x}})^{\top} \boldsymbol{\Sigma}_{\mathbf{x}}^{-1} (\mathbf{x} - \boldsymbol{\mu}_{\mathbf{x}}) \right\}, \quad (4.25)$$

where  $|\boldsymbol{\Sigma}_{\mathbf{x}}|$  denotes the determinant of the matrix  $\boldsymbol{\Sigma}_{\mathbf{x}} \in \mathbb{R}^{n \times n}$ . It is worth noting that when in a multivariate normal distribution the covariance  $\boldsymbol{\Sigma}$  is not a full-rank matrix, then the distribution is degenerate and does not have a density. In order to avoid the drawback, it can be useful to restrict the problem on a subset of  $\boldsymbol{\Sigma}$  such that the covariance matrix for this subset is positive definite.

## 4.5 The Maximum-A-Posteriori Solution

The Maximum-A-Posteriori (MAP) estimator is here adopted as a tool for computing an estimation of the vector  $\mathbf{d}$  and therefore the solution of (4.22). The MAP algorithm can be interpreted as a way for choosing a weighted pseudoinverse according to the reliability of the available measurements.

The first assumption for adopting the MAP approach is to consider the vector of dynamics variables  $\mathbf{d}$  and the vector of the measurements  $\mathbf{y}$  as two stochastic variables with Gaussian distributions. The estimation problem can be summarized as follows.

### The problem

*Given the measurements  $\mathbf{y}$  and the prior knowledge of the model constraints, estimate the vector  $\mathbf{d}$  by maximizing the conditional probability distribution of  $\mathbf{d}$  given  $\mathbf{y}$ , such that*

$$\mathbf{d}^{\text{MAP}} = \arg \max_{\mathbf{d}} p(\mathbf{d}|\mathbf{y}) \propto \arg \max_{\mathbf{d}} p(\mathbf{d}, \mathbf{y}). \quad (4.26)$$

Since the normal distributions  $\mathbf{x}$  and  $\mathbf{y}$  are jointly Gaussian, the conditional probability distribution  $p(\mathbf{d}|\mathbf{y})$  is such that

$$p(\mathbf{d}|\mathbf{y}) = \frac{p(\mathbf{d}, \mathbf{y})}{p(\mathbf{y})} = \frac{p(\mathbf{d})p(\mathbf{y}|\mathbf{d})}{p(\mathbf{y})}. \quad (4.27)$$

In the following computation, the term  $p(\mathbf{y})$  is negligible since it does not depend on  $\mathbf{d}$ . This is the reason of the proportionality between the conditional probability distribution and the joint distribution in (4.26). Hereafter each term in (4.27) is computed separately to obtain the final analytical solution. For the sake of simplicity,  $(\mathbf{q}, \dot{\mathbf{q}})$  dependencies are omitted in the computations.

### Computation of $p(\mathbf{y}|\mathbf{d})$

Let us first give an expression for the conditional PDF  $p(\mathbf{y}|\mathbf{d})$ :

$$\begin{aligned} p(\mathbf{y}|\mathbf{d}) &\propto \exp -\frac{1}{2} \left\{ (\mathbf{y} - \boldsymbol{\mu}_{y|\mathbf{d}})^\top \boldsymbol{\Sigma}_{y|\mathbf{d}}^{-1} (\mathbf{y} - \boldsymbol{\mu}_{y|\mathbf{d}}) \right\} \\ &= \exp -\frac{1}{2} \left\{ [\mathbf{y} - (\mathbf{Y}\mathbf{d} + \mathbf{b}_Y)]^\top \boldsymbol{\Sigma}_{y|\mathbf{d}}^{-1} [\mathbf{y} - (\mathbf{Y}\mathbf{d} + \mathbf{b}_Y)] \right\}, \end{aligned} \quad (4.28)$$

which implicitly makes the assumption that the measurements equation (4.14) is affected by a Gaussian noise with zero mean and covariance  $\boldsymbol{\Sigma}_{y|\mathbf{d}}$ .

### Computation of $p(\mathbf{d})$

Define now a PDF for the normal distribution  $\mathbf{d}$ . By pursuing the same methodology, we would like to write its distribution in the following form

$$\mathbf{d} \sim \mathcal{N}(\boldsymbol{\mu}_D, \boldsymbol{\Sigma}_D), \quad (4.29)$$

such that the PDF

$$p(\mathbf{d}) \propto \exp -\frac{1}{2} \left\{ \mathbf{e}(\mathbf{d})^\top \boldsymbol{\Sigma}_D^{-1} \mathbf{e}(\mathbf{d}) \right\}, \quad (4.30)$$

taking into account constraints of Equation (4.5) with  $\mathbf{e}(\mathbf{d}) = \mathbf{D}\mathbf{d} + \mathbf{b}_D$ .

However, this intuitive choice leads to a degenerate normal distribution and a regularization term is needed. For example, if we have a Gaussian prior knowledge on  $\mathbf{d}$  in the form of  $\mathbf{d} \sim \mathcal{N}(\boldsymbol{\mu}_d, \boldsymbol{\Sigma}_d)$  distribution, we can reformulate Equation (4.29) as follows:

$$\mathbf{d} \sim \mathcal{N}(\bar{\boldsymbol{\mu}}_D, \bar{\boldsymbol{\Sigma}}_D), \quad (4.31)$$

such that (4.30) becomes

$$\begin{aligned} p(\mathbf{d}) &\propto \exp -\frac{1}{2} \left\{ \mathbf{e}(\mathbf{d})^\top \boldsymbol{\Sigma}_D^{-1} \mathbf{e}(\mathbf{d}) + (\mathbf{d} - \boldsymbol{\mu}_d)^\top \boldsymbol{\Sigma}_d^{-1} (\mathbf{d} - \boldsymbol{\mu}_d) \right\} \\ &= \exp -\frac{1}{2} \left\{ (\mathbf{D}\mathbf{d} + \mathbf{b}_D)^\top \boldsymbol{\Sigma}_D^{-1} (\mathbf{D}\mathbf{d} + \mathbf{b}_D) + (\mathbf{d} - \boldsymbol{\mu}_d)^\top \boldsymbol{\Sigma}_d^{-1} (\mathbf{d} - \boldsymbol{\mu}_d) \right\} \\ &= \exp -\frac{1}{2} \left\{ (\mathbf{d} - \bar{\boldsymbol{\mu}}_D)^\top \bar{\boldsymbol{\Sigma}}_D^{-1} (\mathbf{d} - \bar{\boldsymbol{\mu}}_D) \right\}, \end{aligned} \quad (4.32)$$

where the covariance and the mean are, respectively,

$$\bar{\boldsymbol{\Sigma}}_D = \left( \mathbf{D}^\top \boldsymbol{\Sigma}_D^{-1} \mathbf{D} + \boldsymbol{\Sigma}_d^{-1} \right)^{-1}, \quad (4.33a)$$

$$\bar{\boldsymbol{\mu}}_D = \bar{\boldsymbol{\Sigma}}_D \left( \boldsymbol{\Sigma}_d^{-1} \boldsymbol{\mu}_d - \mathbf{D}^\top \boldsymbol{\Sigma}_D^{-1} \mathbf{b}_D \right). \quad (4.33b)$$

The role of  $\boldsymbol{\Sigma}_D$  is to establish how much the dynamic model (4.5) should be considered correct. The quantities  $\boldsymbol{\mu}_d$  and  $\boldsymbol{\Sigma}_d$ , instead, define the Gaussian prior distribution on  $\mathbf{d}$  (namely, the regularization term).

### Computation of $p(\mathbf{d}|\mathbf{y})$

By combining Equations (4.28) and (4.32) we are now ready to give a new formulation of the estimation problem for the conditional PDF of  $\mathbf{d}$  given  $\mathbf{y}$ , i.e.,

$$\begin{aligned} p(\mathbf{d}|\mathbf{y}) &\propto \exp -\frac{1}{2} \left\{ (\mathbf{d} - \bar{\boldsymbol{\mu}}_D)^\top \bar{\boldsymbol{\Sigma}}_D^{-1} (\mathbf{d} - \bar{\boldsymbol{\mu}}_D) + \right. \\ &\quad \left. + \left[ \mathbf{y} - (\mathbf{Y}\mathbf{d} + \mathbf{b}_Y) \right]^\top \boldsymbol{\Sigma}_{y|\mathbf{d}}^{-1} \left[ \mathbf{y} - (\mathbf{Y}\mathbf{d} + \mathbf{b}_Y) \right] \right\}, \end{aligned} \quad (4.34)$$

with covariance matrix and mean as follows:

$$\Sigma_{d|y} = \left( \bar{\Sigma}_D^{-1} + \mathbf{Y}^\top \Sigma_{y|d}^{-1} \mathbf{Y} \right)^{-1}, \quad (4.35a)$$

$$\boldsymbol{\mu}_{d|y} = \Sigma_{d|y} \left[ \mathbf{Y}^\top \Sigma_{y|d}^{-1} (\mathbf{y} - \mathbf{b}_Y) + \bar{\Sigma}_D^{-1} \bar{\boldsymbol{\mu}}_D \right]. \quad (4.35b)$$

Moreover, in the Gaussian case the MAP solution coincides with the mean of the PDF  $p(\mathbf{d}|\mathbf{y})$  yielding to:

$$\mathbf{d}^{\text{MAP}} = \boldsymbol{\mu}_{d|y}. \quad (4.36)$$

### 4.5.1 The Cholesky Decomposition

Computations for (4.36) can be performed in several ways but computationally cost-efficient solutions need to exploit the sparsity in the matrices  $\mathbf{D}$  and  $\mathbf{Y}$ . The solution is here retrieved by applying the Cholesky decomposition. The Cholesky decomposition is mainly used for the numerical solution of systems expressed in the  $\mathbf{A}\mathbf{x} = \mathbf{b}$  form. This approach allows to decompose the generic symmetric<sup>4</sup>, positive-definite matrix  $\mathbf{A} \in \mathbb{R}^{n \times n}$  into a product of a couple of triangular matrices (a lower triangular and its transpose), such that  $\mathbf{A} = \mathbf{L}\mathbf{L}^\top$ .

When  $\mathbf{A}$  is a sparse matrix (i.e., the most of its entries are zero), it is convenient to compute a heuristic permutation matrix  $\mathbf{P}$  for sparsing  $\mathbf{L}$ , such that,  $\mathbf{A} = \mathbf{P}\mathbf{L}\mathbf{L}^\top\mathbf{P}^\top$ . This speeds up remarkably the time of the execution for computing the system solution and the computational cost<sup>5</sup> decreases passing from a Cholesky to a sparse Cholesky decomposition ( $O(n^3)_{\text{sparse}} < O(n^3)_{\text{nonSparse}}$ ).

In the Algorithms 2 and 3, the pseudocodes for computing the solutions (4.33b) and (4.35b) via sparse Cholesky method are shown, respectively. For the sake of simplicity, they were here split into two different algorithms. Clearly, in the code computation they represent a whole algorithm since the solution (4.33b) is mandatorily required for computing (4.35b).

<sup>4</sup>The Cholesky decomposition embraces the widest case of Hermitian matrices. For the MAP case all the entries of the matrix  $\in \mathbb{R}$ , thus the Hermitian coincides exactly with its transpose.

<sup>5</sup>The computational cost is considered as the amount of the operations performed during an algorithm execution. It is a parameter to define how the cost scales with the size  $n$  of the problem. For example, in the case of a  $n \times n$  matrix related operation, the syntax  $O(n^3)$  means that the algorithm has a computational complexity that grows proportionally to  $n^3$  (e.g., the complexity of a matrix inversion).

---

**Algorithm 2** Compute  $\bar{\mu}_D$ , Equation (4.33b)

---

**Require:** Pre-computation of the permutation matrix  $\bar{P}_D$

```
1: procedure SOLUTIONWITHSPARSECHOLESKY
2:    $N \leftarrow$  number of samples
3:   cholSolver  $\leftarrow$  Matlab function
4: loop:
5:   for  $i = 1 \rightarrow N$  do
6:      $\Rightarrow$  consider  $\mathbf{b}_i = (\Sigma_d^{-1} \boldsymbol{\mu}_d - D^\top \Sigma_D^{-1} \mathbf{b}_D) \Big|_i$ 
7:      $\Rightarrow$  solve  $\mathbf{A}_i \mathbf{x} = \mathbf{b}_i$  :
8:      $\bar{\mu}_D \Big|_i = \text{cholSolver} \left( \bar{\Sigma}_D^{-1} \Big|_i, \mathbf{b}_i, \bar{P}_D \right)$ 
9:     goto loop.
10:  end
```

---

---

**Algorithm 3** Compute  $d^{\text{MAP}}$ , Equation (4.35b)

---

**Require:** Pre-computation of the permutation matrix  $P_{d|y}$

```
1: procedure SOLUTIONWITHSPARSECHOLESKY
2:    $N \leftarrow$  number of samples
3:   cholSolver  $\leftarrow$  Matlab function
4: loop:
5:   for  $i = 1 \rightarrow N$  do
6:      $\Rightarrow$  consider  $\mathbf{b}_i = \left[ \mathbf{Y}^\top \Sigma_{y|d}^{-1} (\mathbf{y} - \mathbf{b}_Y) + \bar{\Sigma}_D^{-1} \bar{\mu}_D \right] \Big|_i$ 
7:      $\Rightarrow$  solve  $\mathbf{A}_i \mathbf{x} = \mathbf{b}_i$  :
8:      $\boldsymbol{\mu}_{d|y} \Big|_i = \text{cholSolver} \left( \Sigma_{d|y}^{-1} \Big|_i, \mathbf{b}_i, P_{d|y} \right)$ 
9:     goto loop.
10:  end
```

---

Both the algorithms require the pre-computation of the permutation matrix  $P$  through the Matlab `chol` built-in function. Moreover, it is important to note that, even though the algorithm currently does not work in this way, in lines 8, it would be useful to re-order the matrix  $\Sigma$  (accordingly to the permutation matrix structure) before the *cholSolver* step.

## 4.6 Considerations on the Estimator Choice

In this Section some considerations on the choice of the MAP estimator are made. The accuracy of the estimation heavily depends on the adopted estimator and therefore a detailed description is needed.

### 4.6.1 Linear Estimator for Jointly Gaussian Vectors

Let  $\mathbf{x}$ ,  $\mathbf{y}$  be two random Gaussian vectors with distributions

$$\mathbf{x} \sim \mathcal{N}(\boldsymbol{\mu}_x, \boldsymbol{\Sigma}_x), \quad \mathbf{y} \sim \mathcal{N}(\boldsymbol{\mu}_y, \boldsymbol{\Sigma}_y), \quad (4.37)$$

respectively, and jointly Gaussian, i.e.,

$$\begin{bmatrix} \mathbf{x} \\ \mathbf{y} \end{bmatrix} \sim \mathcal{N} \left( \begin{bmatrix} \boldsymbol{\mu}_x \\ \boldsymbol{\mu}_y \end{bmatrix}, \begin{bmatrix} \boldsymbol{\Sigma}_x & \boldsymbol{\Sigma}_{xy} \\ \boldsymbol{\Sigma}_{xy}^T & \boldsymbol{\Sigma}_y \end{bmatrix} \right), \quad (4.38)$$

where the terms  $\boldsymbol{\Sigma}_{xy}$  and  $\boldsymbol{\Sigma}_{xy}^T$  represent the jointly covariance matrices.

Consider now the following estimation problem.

#### The problem

*Given two Gaussian vectors  $\mathbf{x}$  and  $\mathbf{y}$  jointly Gaussian, estimate the value of (the unobserved)  $\mathbf{x}$  given that we have observed  $\mathbf{y}$ . The estimate of  $\mathbf{x}$  is a function of  $\mathbf{y}$ , i.e.,  $\hat{\mathbf{x}}(\mathbf{y})$  and the associated estimation error is defined as  $\mathbf{e} = \mathbf{x} - \hat{\mathbf{x}}(\mathbf{y})$ .*

The time has now come to choose the proper form of the estimator  $\hat{\mathbf{x}}(\mathbf{y})$ . Let us start with considering a minimum mean square error (MMSE) estimator  $\hat{\mathbf{x}}^{\text{MMSE}}(\mathbf{y})$  of  $\mathbf{x}$  that is a function which minimizes the mean square error (MSE), i.e., the trace of the error covariance matrix, such that

$$\begin{aligned} \hat{\mathbf{x}}^{\text{MMSE}}(\mathbf{y}) &= \arg \min_{\hat{\mathbf{x}}} \text{Tr} \left\{ \underbrace{E \left[ \left[ (\mathbf{x} - \hat{\mathbf{x}}(\mathbf{y})) (\mathbf{x} - \hat{\mathbf{x}}(\mathbf{y}))^T \right] \right]}_{\text{MSE}} \right\} \\ &= \arg \min_{\hat{\mathbf{x}}} E \left[ \text{Tr}(\mathbf{e}\mathbf{e}^T) \right] \\ &= \arg \min_{\hat{\mathbf{x}}} E \left[ \mathbf{e}^T \mathbf{e} \right]. \end{aligned} \quad (4.39)$$

See Equation (17) of [Petersen and Pedersen, 2012] for retrieving Equation (4.39).

It is shown in [Oppenheim et al., 2016] (as well as in many other textbooks of probability theory) that the estimator as defined in (4.39) coincides with the expectation of the conditional distribution

$$\mathbf{x}|\mathbf{y} \sim \mathcal{N}(\boldsymbol{\mu}_{x|y}, \boldsymbol{\Sigma}_{x|y}), \quad (4.40)$$

such as

$$\hat{\mathbf{x}}^{\text{MMSE}}(\mathbf{y}) = \boldsymbol{\mu}_{x|y}. \quad (4.41)$$

For the Gauss-Markov theorem [Nowak, 2011], if  $\mathbf{x}$  and  $\mathbf{y}$  are jointly Gaussian random vectors with the distribution in (4.38), then the conditional distribution of  $\mathbf{x}$  given  $\mathbf{y}$  is

$$\mathbf{x}|\mathbf{y} \sim \mathcal{N}(\boldsymbol{\mu}_x + \boldsymbol{\Sigma}_{xy}\boldsymbol{\Sigma}_y^{-1}(\mathbf{y} - \boldsymbol{\mu}_y), \boldsymbol{\Sigma}_x - \boldsymbol{\Sigma}_{xy}\boldsymbol{\Sigma}_y^{-1}\boldsymbol{\Sigma}_{xy}^T). \quad (4.42)$$

This yields to a new formulation that identifies the estimator, such that

$$\hat{\mathbf{x}}^{\text{MMSE}}(\mathbf{y}) = \boldsymbol{\mu}_x + \boldsymbol{\Sigma}_{xy}\boldsymbol{\Sigma}_y^{-1}(\mathbf{y} - \boldsymbol{\mu}_y), \quad (4.43a)$$

$$\text{cov} \left[ \mathbf{x} - \hat{\mathbf{x}}^{\text{MMSE}}(\mathbf{y}) \right] = \boldsymbol{\Sigma}_x - \boldsymbol{\Sigma}_{xy}\boldsymbol{\Sigma}_y^{-1}\boldsymbol{\Sigma}_{xy}^T, \quad (4.43b)$$

where (4.43a) is the mean and (4.43b) is the covariance associated to the estimator. According to the Gauss-Markov theorem, Equation (4.43a) is a linear function of  $\mathbf{y}$  and in this case the MMSE estimator is said to be linear. In many cases, it is difficult to determine the analytical expression of the MMSE estimator. A widely used tradeoff is to restrict the estimator to be a linear (i.e., linear plus a constant) function of  $\mathbf{y}$ , and to choose the linear relationship in order to minimize the MSE [Oppenheim and Verghese, 2010]. The resulting estimator is called the linear minimum mean square error (LMMSE) estimator.

## 4.6.2 Linear Estimator for Linear Regressors

Let us suppose now to consider the following linear regressor model:

$$\mathbf{y} = \mathbf{C}\mathbf{x} + \mathbf{e}, \quad (4.44)$$

where

$$\mathbf{x} \sim \mathcal{N}(\boldsymbol{\mu}_x, \mathbf{C}\boldsymbol{\Sigma}_x\mathbf{C}^T), \quad \mathbf{e} \sim \mathcal{N}(\mathbf{0}, \boldsymbol{\Sigma}_e), \quad (4.45)$$

are the distributions of the Gaussian variable  $\mathbf{x}$  and of the error  $\mathbf{e}$ , respectively. This straightforwardly yields to

$$\mathbf{y} \sim \mathcal{N}(\mathbf{C}\boldsymbol{\mu}_x, \mathbf{C}\boldsymbol{\Sigma}_x\mathbf{C}^T + \boldsymbol{\Sigma}_e), \quad (4.46)$$

being  $\boldsymbol{\mu}_y = \mathbf{C}\boldsymbol{\mu}_x$  and  $\boldsymbol{\Sigma}_y = \mathbf{C}\boldsymbol{\Sigma}_x\mathbf{C}^T + \boldsymbol{\Sigma}_e$  the mean and the covariance of the regressor model, respectively. Also in this case we can consider the same jointly Gaussian situation as in (4.38), where now:

$$\boldsymbol{\Sigma}_{xy} = \text{cov} \left[ \mathbf{x}, \mathbf{C}\mathbf{x} \right] = \text{cov} \left[ \mathbf{x}, \mathbf{x} \right] \mathbf{C}^T = E \left[ (\mathbf{x}\mathbf{x}^T) - \boldsymbol{\mu}_x\boldsymbol{\mu}_x^T \right] \mathbf{C}^T = \boldsymbol{\Sigma}_x\mathbf{C}^T. \quad (4.47)$$

Given that, the set of Equations (4.43) become

$$\hat{\mathbf{x}}^{\text{LMMSE}}(\mathbf{y}) = \boldsymbol{\mu}_x + \boldsymbol{\Sigma}_x\mathbf{C}^T (\mathbf{C}\boldsymbol{\Sigma}_x\mathbf{C}^T + \boldsymbol{\Sigma}_e)^{-1} (\mathbf{y} - \mathbf{C}\boldsymbol{\mu}_x), \quad (4.48a)$$

$$\text{cov} \left[ \mathbf{x} - \hat{\mathbf{x}}^{\text{LMMSE}}(\mathbf{y}) \right] = \boldsymbol{\Sigma}_x - \boldsymbol{\Sigma}_x\mathbf{C}^T (\mathbf{C}\boldsymbol{\Sigma}_x\mathbf{C}^T + \boldsymbol{\Sigma}_e)^{-1} \mathbf{C}\boldsymbol{\Sigma}_x. \quad (4.48b)$$

This formulation is useful to understand what happens to the solution when the variable  $\mathbf{x}$  (i.e., the prior in our algorithm) is very reliable. This yields to  $\boldsymbol{\Sigma}_x \approx \mathbf{0}$  and therefore to

$$\hat{\mathbf{x}}^{\text{LMMSE}}(\mathbf{y}) \approx \boldsymbol{\mu}_x, \quad (4.49a)$$

$$\text{cov} \left[ \mathbf{x} - \hat{\mathbf{x}}^{\text{LMMSE}}(\mathbf{y}) \right] \approx \mathbf{0}. \quad (4.49b)$$

Another equivalent representation can be provided by applying the Woodbury identities:

- to (4.48a) (see Equation (156) in [Petersen and Pedersen, 2012] or in [Golub and Van Loan, 1996], Chapter 2.1.4)

$$\boldsymbol{\Sigma}_x\mathbf{C}^T (\mathbf{C}\boldsymbol{\Sigma}_x\mathbf{C}^T + \boldsymbol{\Sigma}_e)^{-1} = (\boldsymbol{\Sigma}_x^{-1} + \mathbf{C}^T\boldsymbol{\Sigma}_e^{-1}\mathbf{C})^{-1} \mathbf{C}^T\boldsymbol{\Sigma}_e^{-1}, \quad (4.50)$$

- to (4.48b) (see Equation (158) in [Petersen and Pedersen, 2012])

$$\boldsymbol{\Sigma}_x - \boldsymbol{\Sigma}_x\mathbf{C}^T (\mathbf{C}\boldsymbol{\Sigma}_x\mathbf{C}^T + \boldsymbol{\Sigma}_e)^{-1} \mathbf{C}\boldsymbol{\Sigma}_x = (\boldsymbol{\Sigma}_x^{-1} + \mathbf{C}^T\boldsymbol{\Sigma}_e^{-1}\mathbf{C})^{-1}. \quad (4.51)$$

Given (4.50) and (4.51), Equations (4.48) can be written as

$$\begin{aligned} \hat{\mathbf{x}}^{\text{LMMSE}}(\mathbf{y}) &= \boldsymbol{\mu}_x + (\boldsymbol{\Sigma}_x^{-1} + \mathbf{C}^T\boldsymbol{\Sigma}_e^{-1}\mathbf{C})^{-1} \mathbf{C}^T\boldsymbol{\Sigma}_e^{-1} (\mathbf{y} - \mathbf{C}\boldsymbol{\mu}_x) \\ &= \left[ (\boldsymbol{\Sigma}_x^{-1} + \mathbf{C}^T\boldsymbol{\Sigma}_e^{-1}\mathbf{C})^{-1} \mathbf{C}^T\boldsymbol{\Sigma}_e^{-1} \right] \mathbf{y} + \\ &+ \left[ \mathbf{1} - (\boldsymbol{\Sigma}_x^{-1} + \mathbf{C}^T\boldsymbol{\Sigma}_e^{-1}\mathbf{C})^{-1} \mathbf{C}^T\boldsymbol{\Sigma}_e^{-1}\mathbf{C} \right] \boldsymbol{\mu}_x \\ &= (\boldsymbol{\Sigma}_x^{-1} + \mathbf{C}^T\boldsymbol{\Sigma}_e^{-1}\mathbf{C})^{-1} (\mathbf{C}^T\boldsymbol{\Sigma}_e^{-1}\mathbf{y} + \boldsymbol{\Sigma}_x^{-1}\boldsymbol{\mu}_x), \end{aligned} \quad (4.52a)$$

$$\text{cov} \left[ \mathbf{x} - \hat{\mathbf{x}}^{\text{LMMSE}}(\mathbf{y}) \right] = (\boldsymbol{\Sigma}_x^{-1} + \mathbf{C}^T\boldsymbol{\Sigma}_e^{-1}\mathbf{C})^{-1}. \quad (4.52b)$$

Equation (4.52a) clearly shows that the solution is the weighted sum of  $\boldsymbol{\mu}_x$  (i.e., the mean of the prior in our algorithm) and the variable  $\mathbf{y}$  (i.e., the measurements vector in our algorithm). The second formulation is convenient to understand what happens in case of  $\mathbf{x}$  is very unreliable ( $\boldsymbol{\Sigma}_x^{-1} \approx \mathbf{0}$ ). In this case, the solution is mainly relying on  $\mathbf{y}$ , such that

$$\hat{\mathbf{x}}^{\text{LMMSE}}(\mathbf{y}) \approx (\mathbf{C}^T \boldsymbol{\Sigma}_e^{-1} \mathbf{C})^{-1} \mathbf{C}^T \boldsymbol{\Sigma}_e^{-1} \mathbf{y}, \quad (4.53a)$$

$$\text{cov} [\mathbf{x} - \hat{\mathbf{x}}^{\text{LMMSE}}(\mathbf{y})] \approx (\mathbf{C}^T \boldsymbol{\Sigma}_e^{-1} \mathbf{C})^{-1}. \quad (4.53b)$$

### 4.6.3 Generalized Least-Squares Estimator

In this Section it is shown that the linear estimator solution of the problem in Section 4.6.1 coincides with the solution of the generalized<sup>6</sup> least-squares (GLS) problem.

Define the following GLS problem for the system in the form  $\mathbf{Ax} = \mathbf{b}$ :

$$\begin{aligned} \hat{\mathbf{x}}^{\text{GLS}}(\mathbf{y}) &= \arg \min_x \|\mathbf{Ax} - \mathbf{b}\|_{\boldsymbol{\Sigma}}^2 \\ &= \arg \min_x (\mathbf{Ax} - \mathbf{b})^T \boldsymbol{\Sigma} (\mathbf{Ax} - \mathbf{b}). \end{aligned} \quad (4.54)$$

Thanks to Cholesky factorization (see Section 4.5.1), if  $\boldsymbol{\Sigma} = \boldsymbol{\Sigma}^T$  (symmetric<sup>7</sup>) and  $\boldsymbol{\Sigma} > 0$  (positive-definite), it is always possible the following decomposition:

$$\boldsymbol{\Sigma} = \mathbf{U}^T \mathbf{U}, \quad (4.55)$$

where  $\mathbf{U}$  is an upper triangular matrix. Thus in (4.54),

$$\begin{aligned} \hat{\mathbf{x}}^{\text{GLS}}(\mathbf{y}) &= \arg \min_x (\mathbf{Ax} - \mathbf{b})^T \mathbf{U}^T \mathbf{U} (\mathbf{Ax} - \mathbf{b}) \\ &= \arg \min_x (\mathbf{UAx} - \mathbf{Ub})^T (\mathbf{UAx} - \mathbf{Ub}) \\ &= (\mathbf{A}^T \mathbf{U}^T \mathbf{U} \mathbf{A})^{-1} \mathbf{A}^T \mathbf{U}^T \mathbf{U} \mathbf{b} \\ &= (\mathbf{A}^T \boldsymbol{\Sigma} \mathbf{A})^{-1} \mathbf{A}^T \boldsymbol{\Sigma} \mathbf{b}. \end{aligned} \quad (4.56)$$

<sup>6</sup>The generalized least-square problem is a weighted least-squares where  $\boldsymbol{\Sigma}$  is a non-diagonal matrix, but still symmetric and positive-definite.

<sup>7</sup>Indeed here it is required an Heritian matrix  $\boldsymbol{\Sigma} = \boldsymbol{\Sigma}^*$ , but the case of only real entries yields to  $\boldsymbol{\Sigma}^* = \boldsymbol{\Sigma}^T$ .

Consider in our specific case  $\mathbf{A} = \begin{bmatrix} \mathbf{C} \\ \mathbf{1} \end{bmatrix}$  and  $\mathbf{b} = \begin{bmatrix} \mathbf{y} \\ \boldsymbol{\mu}_x \end{bmatrix}$ , such that in (4.54)

$$\begin{aligned}
\hat{\mathbf{x}}^{\text{GLS}}(\mathbf{y}) &= \arg \min_x \left\| \begin{bmatrix} \mathbf{C} \\ \mathbf{1} \end{bmatrix} \mathbf{x} - \begin{bmatrix} \mathbf{y} \\ \boldsymbol{\mu}_x \end{bmatrix} \right\|_{\text{diag}(\boldsymbol{\Sigma}_e^{-1}, \boldsymbol{\Sigma}_x^{-1})}^2 \\
&= \arg \min_x \left( \|\mathbf{C}\mathbf{x} - \mathbf{y}\|_{\boldsymbol{\Sigma}_e^{-1}}^2 + \|\mathbf{x} - \boldsymbol{\mu}_x\|_{\boldsymbol{\Sigma}_x^{-1}}^2 \right) \\
&= \left( \begin{bmatrix} \mathbf{C} & \mathbf{1} \end{bmatrix} \begin{bmatrix} \boldsymbol{\Sigma}_e^{-1} & \mathbf{0} \\ \mathbf{0} & \boldsymbol{\Sigma}_x^{-1} \end{bmatrix} \begin{bmatrix} \mathbf{C} \\ \mathbf{1} \end{bmatrix} \right)^{-1} \begin{bmatrix} \mathbf{C} & \mathbf{1} \end{bmatrix} \begin{bmatrix} \boldsymbol{\Sigma}_e^{-1} & \mathbf{0} \\ \mathbf{0} & \boldsymbol{\Sigma}_x^{-1} \end{bmatrix} \begin{bmatrix} \mathbf{y} \\ \boldsymbol{\mu}_x \end{bmatrix} \\
&= (\boldsymbol{\Sigma}_x^{-1} + \mathbf{C}^T \boldsymbol{\Sigma}_e^{-1} \mathbf{C})^{-1} (\mathbf{C}^T \boldsymbol{\Sigma}_e^{-1} \mathbf{y} + \boldsymbol{\Sigma}_x^{-1} \boldsymbol{\mu}_x) \\
&\equiv \hat{\mathbf{x}}^{\text{LMMSE}}(\mathbf{y}). \tag{4.57}
\end{aligned}$$

#### 4.6.4 The MAP Estimator

The solution (4.57) is written in the form of the MAP solution (4.35). Thus solving the problem in (4.26) is equivalent to solve a generalized least-squares problem (4.57). Because of this, the MAP problem can be written in the following form:

$$\begin{aligned}
\mathbf{d}^{\text{MAP}} &= \arg \min_d \left\| \begin{bmatrix} \mathbf{D} \\ \mathbf{Y} \\ \mathbf{1} \end{bmatrix} \mathbf{d} - \begin{bmatrix} \mathbf{b}_D \\ \mathbf{y} - \mathbf{b}_Y \\ \boldsymbol{\mu}_d \end{bmatrix} \right\|_{\text{diag}(\boldsymbol{\Sigma}_D^{-1}, \boldsymbol{\Sigma}_{y|d}^{-1}, \boldsymbol{\Sigma}_d^{-1})}^2 \\
&= \arg \min_d \left( \|\mathbf{D}\mathbf{d} - \mathbf{b}_D\|_{\boldsymbol{\Sigma}_D^{-1}}^2 + \|\mathbf{Y}\mathbf{d} - (\mathbf{y} - \mathbf{b}_Y)\|_{\boldsymbol{\Sigma}_{y|d}^{-1}}^2 + \|\mathbf{d} - \boldsymbol{\mu}_d\|_{\boldsymbol{\Sigma}_d^{-1}}^2 \right). \tag{4.58}
\end{aligned}$$

The importance of the Equation (4.58) is two-fold:

- i) it shows clearly the role of each part in the estimation of  $\mathbf{d}$ : the contribution of the dynamic constraints weighted by  $\boldsymbol{\Sigma}_D^{-1}$ , the contribution coming from the sensor readings weighted by  $\boldsymbol{\Sigma}_{y|d}^{-1}$  and the contribution due to the prior on  $\mathbf{d}$  weighted by  $\boldsymbol{\Sigma}_d^{-1}$ ;

- ii) it provides the form of  $\mathbf{A}$  and  $\mathbf{b}$  for the solution in (4.54):

$$\mathbf{A} = \begin{bmatrix} \mathbf{D} \\ \mathbf{Y} \\ \mathbf{1} \end{bmatrix}, \quad \mathbf{b} = \begin{bmatrix} \mathbf{b}_D \\ \mathbf{y} - \mathbf{b}_Y \\ \boldsymbol{\mu}_d \end{bmatrix}. \tag{4.59}$$

If we prefer, Equation (4.58) can be written in the following form:

$$\mathbf{d}^{\text{MAP}} = \arg \min_d \left\{ \|\mathbf{Y}\mathbf{d} - (\mathbf{y} - \mathbf{b}_Y)\|_{\boldsymbol{\Sigma}_{y|d}^{-1}}^2 + \|\mathbf{d} - \bar{\boldsymbol{\mu}}_D\|_{\bar{\boldsymbol{\Sigma}}_D^{-1}}^2 \right\}, \tag{4.60}$$

where  $\bar{\boldsymbol{\mu}}_D$  can be seen as a regularization term in *shaping* the measurements equation.

## Chapter 5

# Software Implementation and Algorithm Validation

- *If an experiment works, something has gone wrong.*
- *In any collection of data, the figure most obviously correct, beyond all need of checking, is the mistake.*

Finagle's laws, Arthur Block

This Chapter presents the software implementation of the MAP solution and several offline validation procedures to assess the effectiveness of the presented estimation algorithm. Since the sensors play a paramount role in the analysis, they will be detailed described in a dedicated section. A new type of wearable force sensing is also introduced in this Chapter and an investigation for its validation w.r.t. the force gold standard is provided to the reader.

### 5.1 MAP Software Implementation

In this Section the software architecture of the MAP framework is presented (see pipeline in Figure 5.1). It was implemented in Matlab and created specifically for offline validations. The code related to the MAP offline computation is hosted on GitHub in a dedicated public repository [MAPest, 2016]. The starting point of the analysis consists in the IMUs readings. Kinematic data are parsed into a compatible Matlab format and then processed as in the following steps.

- Computation of the position of each sensor in the suit w.r.t. the attached link. Xsens does not provide directly this information as output, therefore it

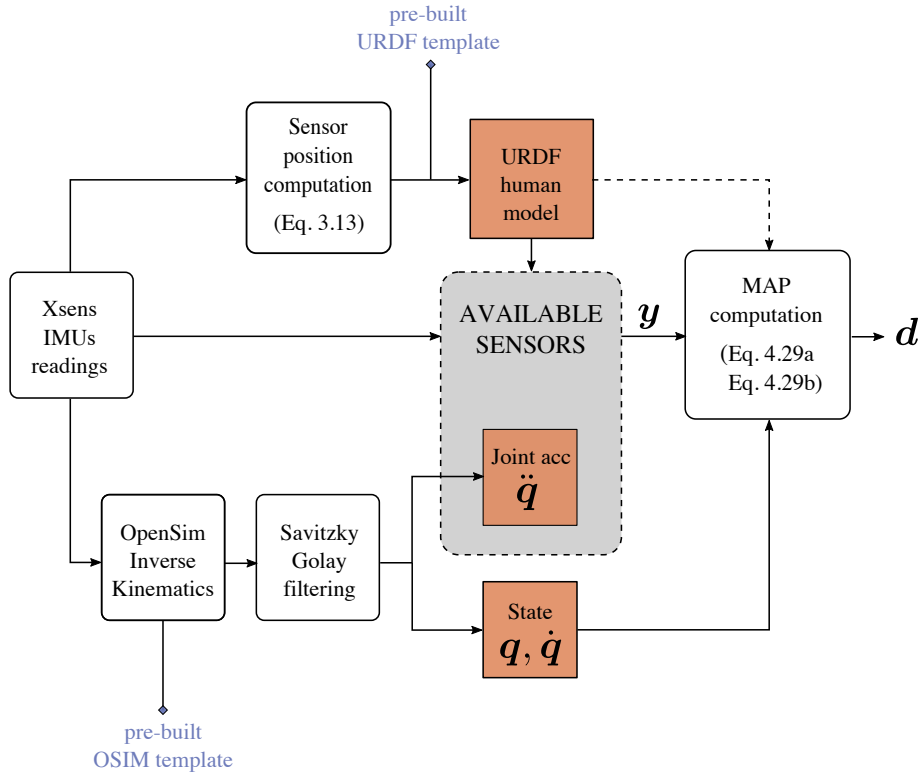


Fig. 5.1 Pipeline for the MAP offline estimation framework.

is necessary to compute it through the estimation Algorithm 1 (Chapter 3). This step is mandatory since sensors position has to be encoded in the non-standard extension of the URDF (see Section B.1 of Appendix B). It is worth remarking that, at this stage, a URDF template exists, built according to the human whole-body modelling in Figure B.2. The dimension of the URDF elements (cylinders, parallelepipeds and spheres) is estimated from IMUs data by making in this way the model scalable with the subject proportions. This is possible thanks to the Xsens trajectories acquisition of ‘fictitious’ markers positioned at several anatomical known bony landmarks.

- Computation of the Inverse Kinematics (IK) by means of the OpenSim specific toolbox [OpenSim] [Delp et al., 2007] that solves a weighted least-squares problem for obtaining the joint angles  $q$ . This is possible thanks to *i*) an OpenSim (OSIM) template previously built in order to match with the URDF model and *ii*) a .trc file containing the markers trajectories acquired by the Xsens system, (see Appendix C). Joint velocities  $\dot{q}$  and accelerations

$\ddot{\mathbf{q}}$  are computed by using a weighted sum of moving windows of elements with a third-order polynomial Savitzky-Golay filtering [Savitzky and Golay, 1964].

- Extraction of the IMUs linear acceleration readings for filling the measurements vector  $\mathbf{y}$ .

All the above-listed points are used to obtain Equation (4.14) for the measurements. They are typically kinematic readings, force sensing data (e.g., the ground reaction forces but in general the external forces acting on the model links) and joint accelerations that are here considered as acquired from a class of ‘fictitious’ DoF-acceleration sensors. By exploiting the information coming from the model and the state, the pipeline block of the MAP computation provides the estimation of  $\mathbf{d}$  given  $\mathbf{y}$  (see Algorithm 3, Chapter 4). It is worth to highlight that Figure 5.1 does not refer to the temporal aspect of the data flow. For a better understanding of the steps sequentiality refer to the Algorithm 4, where a situation with  $S$  subjects performing  $T$  different tasks is considered.

---

**Algorithm 4** MAP offline estimation, Figure 5.1

---

**Require:** IMUs Xsens acquisition, URDF and OSIM templates

```

1: procedure MAPOFFLINEPROCEDURE
2:    $S \leftarrow$  number of subjects
3:    $T \leftarrow$  number of tasks
4: main loop:
5:   for  $s = 1 \rightarrow S$  do
6:     nested loop:
7:       for  $t = 1 \rightarrow T$  do
8:          $\Rightarrow$  parse Xsens data :  $\text{suit}^s\{t\}$ 
9:          $\Rightarrow$  compute sensor position :  $\text{suit}^s\{t\}.\text{sensor}$  goto Algorithm 1
10:         $\Rightarrow$  create URDF model :  $\text{model}^s\{t\}.\text{urdf}$ 
11:         $\Rightarrow$  create OSIM model :  $\text{model}^s\{t\}.\text{osim}$ 
12:         $\Rightarrow$  compute IK :  $\mathbf{q}^s\{t\}$ 
13:         $\Rightarrow$  compute Savitzky-Golay filtering :  $\dot{\mathbf{q}}^s\{t\}, \ddot{\mathbf{q}}^s\{t\}$ 
14:         $\Rightarrow$  wrap available measurements in  $\mathbf{y}^s\{t\}$ 
15:         $\Rightarrow$  compute MAP :  $\mathbf{d}^s\{t\}$  goto Algorithm 3
16:       goto nested loop.
17:     end
18:   goto main loop.
19: end

```

---

## 5.2 Experimental Sensor Setup

### 5.2.1 Motion Capture

The full-body motion capture tracking of the human is retrieved by a Xsens wearable lycra suit in which 17 wired body-mounted IMUs (Figures 5.2a, 5.2b) are located in the upper legs, lower legs, upper arms, lower arms, the pelvis, the sternum, the shoulders and the head. All the IMUs are connected to the Xbus Masters (mounted on the back of the subject) that is in charge of *i*) synchronizing the sensor readings, *ii*) providing them with power and *iii*) handling the wireless communication with a laptop. The wireless connection is guaranteed by an external Access Point connected via Ethernet to a laptop. See Figure 5.2c for the Xsens motion capture tracking setup. The output of this system is a XML-like file with the kinematic variables of the subject who is wearing the suit, according with the Xsens body modelling (Figure 3.1).

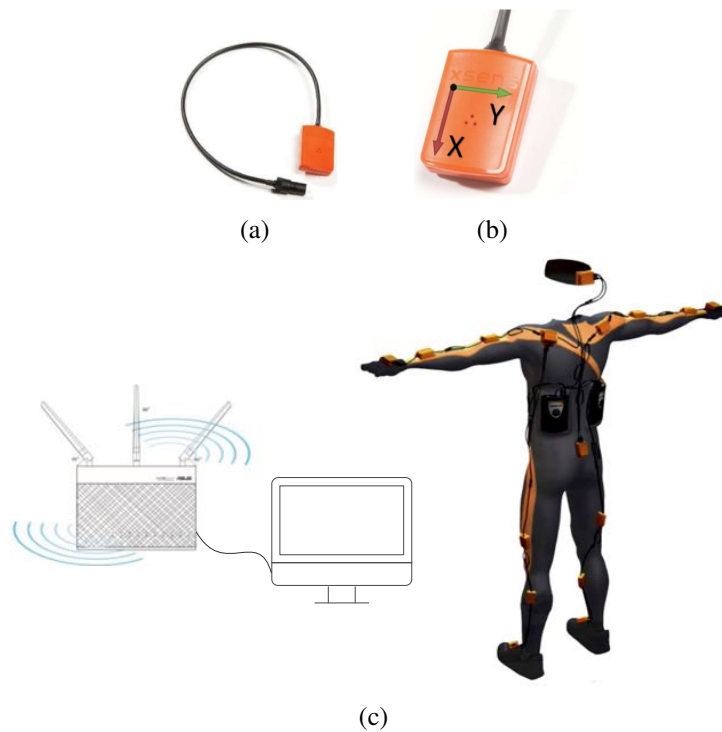


Fig. 5.2 (a) An example of a wired IMU. (b) Reference frame of the IMU. (c) Xsens motion capture setup: 17-wired IMUs embedded in a wearable lycra suit, an Access Point connected to a laptop used for the data acquisition.

[Source: Xsens.]

## 5.2.2 Ground Reaction Forces Tracking

For tracking the human ground reaction forces a new sensing shoes technology was used. By starting from a Xsens original design [Schepers et al., 2007], the *ftShoes* wearable technology is a prototype recently developed at Istituto Italiano di Tecnologia for measuring the human ground reaction forces. It consists of a pair of shoes instrumented with four Force/Torque (F/T) sensors (Figures 5.3a, 5.3b) applied at the bottom of both soles. Each shoe has two F/T sensors positioned at the heel and the forefoot, respectively, and in turn each sensor is comprised in between two metallic thin plates, thus they can be considered independent w.r.t. each other. Each human foot is placed in the *ftShoe* as in Figure 5.3c.

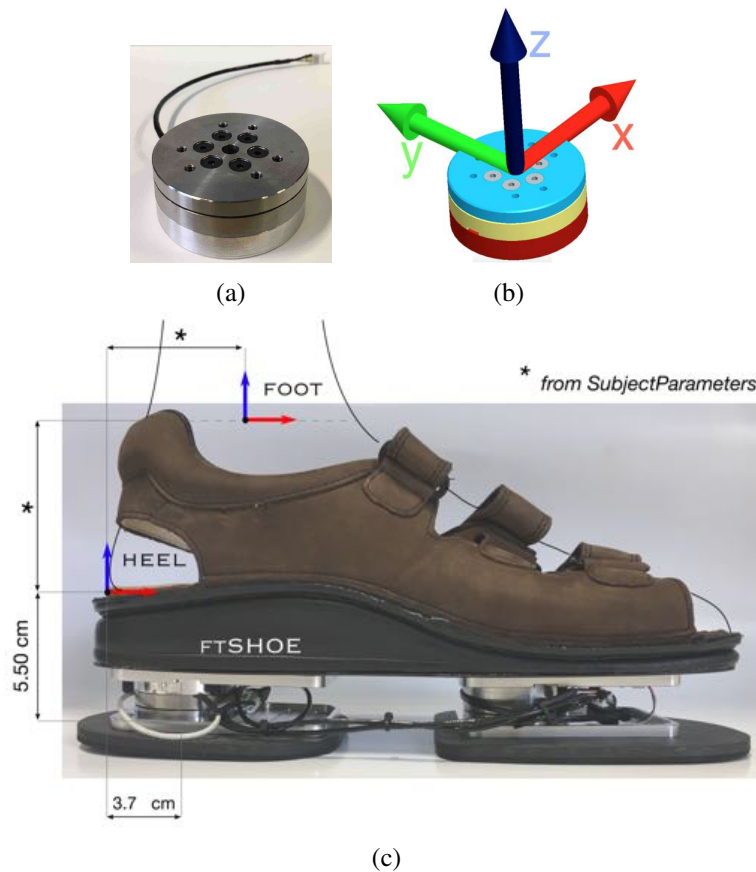


Fig. 5.3 A F/T sensor developed for the iCub robot (a) with reference frame (b). Each shoe is provided of two F/T sensors. (c) Sketch of human foot located into the *ftShoe* with reference frames used for transforming the forces from the shoe frame into the human related foot frame.

### 5.3 Data Analysis

Data for the algorithm validation were collected at University of Waterloo (ON, Canada). The setup encompassed *i*) the Xsens wearable suit (in the look-and-hoop strap version) for the human motion tracking , *ii*) the ftShoes prototype for the ground reaction computation. Two portable AMTI force plates and a printed fixture of the shoes to be applied on the force plates (Figure 5.5a) were additionally required for the shoes validation.

Five healthy subjects (Table 5.1) were asked to wear the sensorized suit and the ftShoes and to perform on the force plates different tasks, with the feet aligned to the printed fixture (as Figure 5.5b). The tasks selected for this analysis are listed here as follows and shown in Figure 5.4:

- 10 repetitions of up-and-down arm movements (T1), Figure 5.4a;
- 10 repetitions of right-left-right torso twisting (T2), Figure 5.4b.

Kinematic data were acquired at a frequency of 240 Hz, force plates and ft-Shoes data at 100 Hz. The synchronization between the motion capture system and the force plates was guaranteed by a synch station provided by Xsens. Readings from the shoes<sup>1</sup> were synchronized by code. Data with different acquisition rates were linearly interpolated before being processed.



(a) Task T1



(b) Task T2

Fig. 5.4 Human subjects while performing (a) the up-and-down arms movement (task T1) and (b) the right-left-right torso twisting (task T2).

<sup>1</sup>ftShoes readings are obtained through YARP, see in chapter Section 6.1.

Table 5.1 Subjects eligible for the analysis. Each subject was provided of a written informative consent before starting the experiment.

Subject	Gender	Age	Height [ cm]	Mass [ kg]
S1	M	24	179	75.9
S2	F	26	163	63.9
S3	M	27	179	83.0
S4	M	26	187	93.6
S5	M	27	175	72.0

### 5.3.1 *ftShoes* Validation

The Section reports the analysis for the validation of the new technology w.r.t. the gold standard in ground reaction force measurements (i.e., the force plates). The analysis required to express both readings in a common reference frame (e.g., the human foot frame<sup>2</sup>).

A Root Mean Square Error (RMSE) analysis (Table 5.2) has been performed for the above described dataset, for validating the three components of the forces ( $f_x, f_y, f_z$ ) and moments ( $m_x, m_y, m_z$ ). Figure 5.6 shows the forces (on the left column) and moments (on the right column) for validating the left *ftShoe* reading (in human left foot frame) w.r.t. the gold standard provided by its coupled force plate FP1, for subject S1, tasks T1-T2. Similarly, Figure 5.7 validates the right *ftShoe* w.r.t. the force plate FP2, for the same subject, in the same tasks.

The RMSE values are in general very low denoting a good matching of each shoe signal w.r.t. the related force plate. Despite some values (highlighted in red) seem to provide a worst estimation of the forces, they are anyway considered acceptable from the force plate datasheet<sup>3</sup>. Another important source of error could be attributed to fact that the shoes are not rigidly attached to the force plates. It is worth noting that, even if explicitly required, the subject did not hold his feet

<sup>2</sup>IMUs readings have been used here for retrieving the position of each foot w.r.t. the reference frame of the related *ftShoe*/force plate.

<sup>3</sup>From AMTI datasheet: by considering an error of 0.4% on the full scale due to a combination of hysteresis and non-linearity noises and a subject standard weight of 700 [ N], the error  $e_f$  on the forces could be quantified as  $e_f = [23, 23, 18]$  [ N]. Similarly for the moment error  $e_m = [4.5, 4.5, 2.25]$  [ Nm].

fixed on the fixture (e.g., some tasks implicitly caused slippery conditions), while the analysis is completely based on this strong assumption (i.e., constant transformation between the ftShoes/force plates origins).

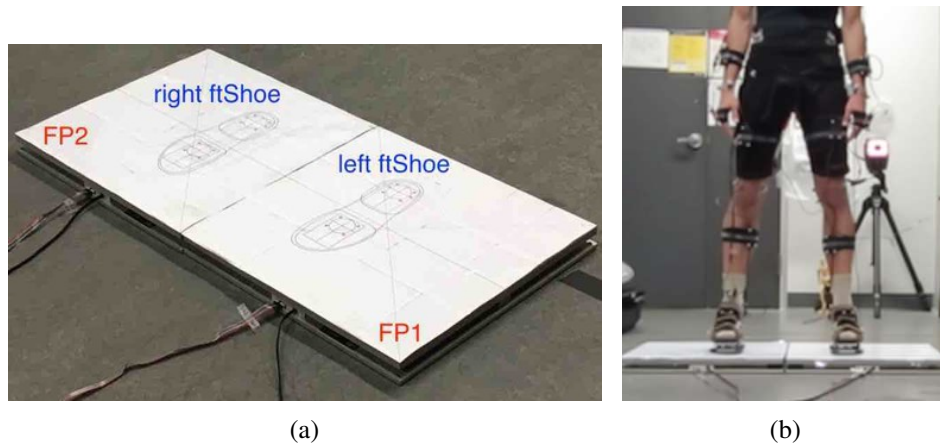


Fig. 5.5 (a) ftShoes fixture applied on the top surface of two force plates. The left ftShoe is coupled with the force plate FP1 and the right ftShoe with FP2. (b). A subject equipped stands on the force plates with the ftShoes, on the position defined in (a).

Table 5.2 RMSE analysis of the forces [ N] and the moments [ Nm] for validating the left ftShoe w.r.t. the forceplate FP1 and the right ftShoe w.r.t. the force plate FP2, respectively. (Subjects S1, S2, S3, S4, S5; tasks T1, T2).

Subject	Task	FP1 - left ftShoe						FP2 - right ftShoe					
		$f_x$	$f_y$	$f_z$	$m_x$	$m_y$	$m_z$	$f_x$	$f_y$	$f_z$	$m_x$	$m_y$	$m_z$
S1	T1	1.52	1.30	5.53	2.39	3.93	0.57	1.74	2.42	1.52	3.13	1.77	0.48
	T2	4.50	4.72	5.86	2.79	4.44	0.74	4.19	5.80	2.98	2.60	1.73	2.03
S2	T1	1.76	2.65	0.96	1.81	0.29	1.53	1.92	3.34	3.37	1.14	0.49	0.33
	T2	4.13	4.59	1.22	1.92	0.46	1.74	4.97	4.95	6.02	0.70	1.30	0.79
S3	T1	3.28	1.60	11.09	2.31	2.24	0.58	7.61	1.03	1.99	2.03	3.26	1.13
	T2	4.96	6.08	11.20	3.55	2.23	1.12	8.99	4.69	4.31	1.19	5.01	2.50
S4	T1	1.88	1.68	2.73	2.89	4.05	0.53	1.51	1.60	3.65	3.20	5.84	0.61
	T2	9.55	11.66	3.44	4.71	5.66	1.03	10.58	8.17	5.99	1.68	3.75	2.60
S5	T1	2.89	4.90	1.38	2.01	0.97	1.67	1.40	3.48	1.33	2.74	1.63	1.57
	T2	4.50	4.29	1.53	1.72	1.16	1.63	3.16	4.09	3.41	3.24	2.01	0.88

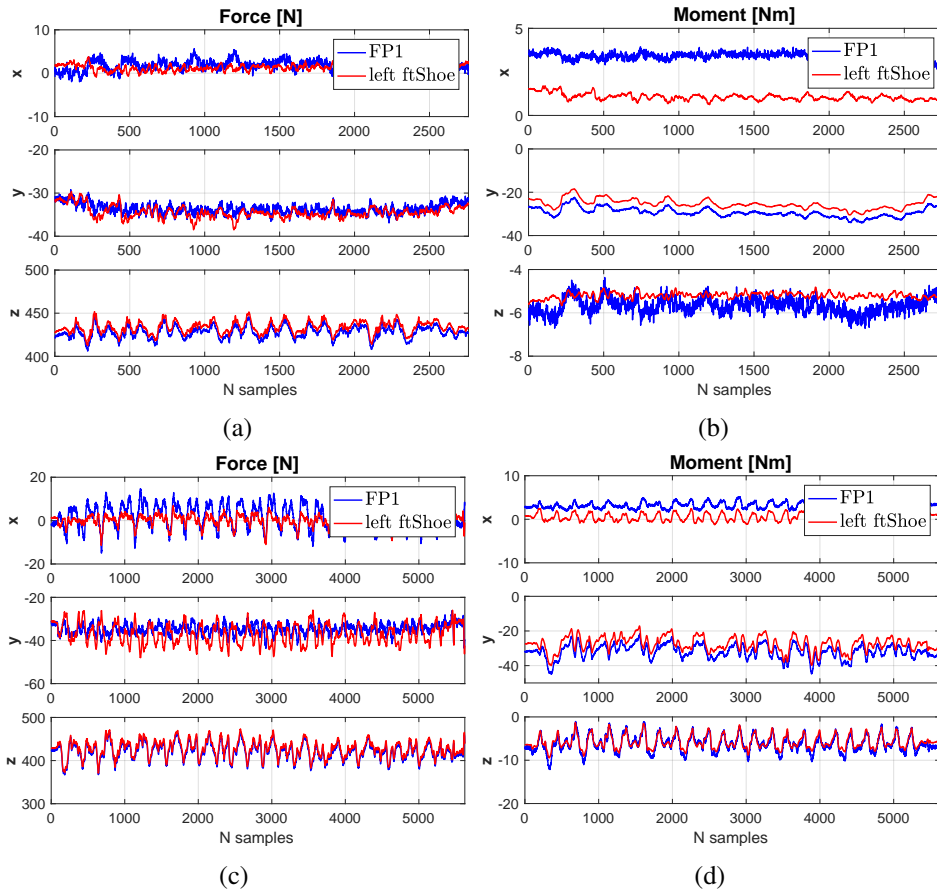


Fig. 5.6 Subject S1 validation of the left ftShoe (in red) with the related force plate FP1 (in blue) for the forces (on the left column) and the moment (on the right column) for the task T1 (a)-(b) and task T2 (c)-(d).

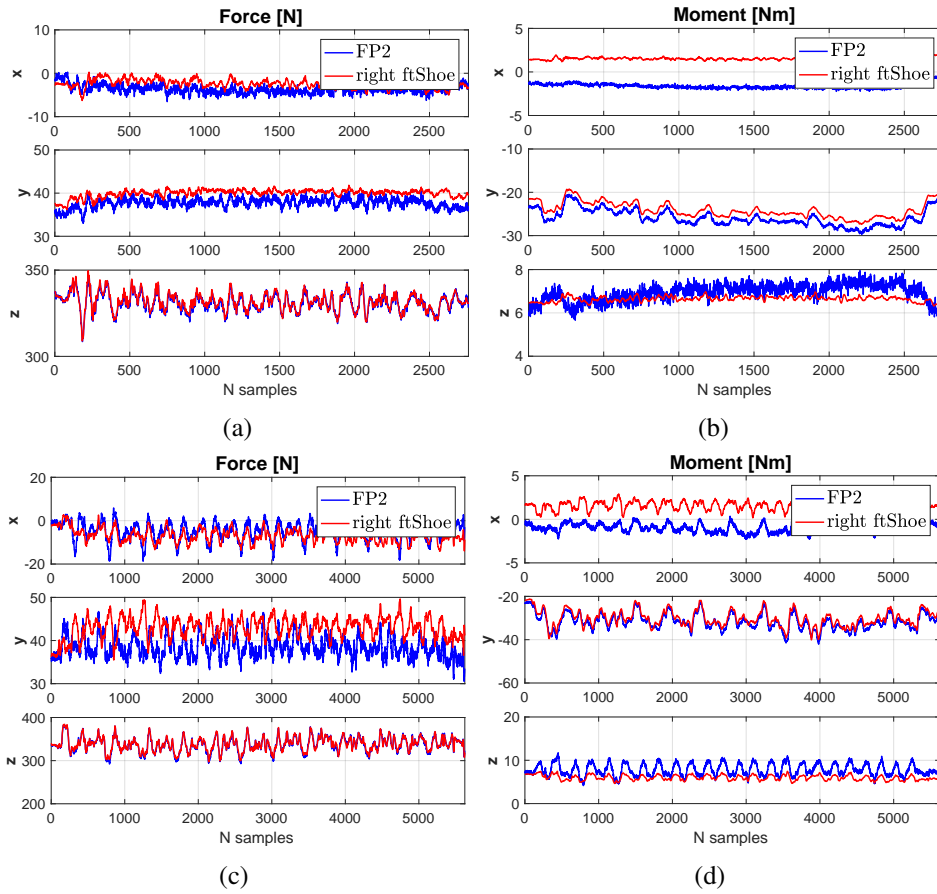


Fig. 5.7 Subject S1 validation of the right ftShoe (in red) with the related force plate FP2 (in blue) for the forces (on the left column) and the moment (on the right column) for the task T1 (a)-(b) and task T2 (c)-(d).

### 5.3.2 Estimation of Human Variables

The MAP algorithm is a tool for estimating quantities related to the joints and links of the human model. It is worth remarking that the vector  $\mathbf{d}$  (the solution (4.35b)) contains variables that can be directly measured ( $\underline{\mathbf{a}}, \underline{\mathbf{f}}^x$ ) and variables that can not be directly measured in humans ( $\underline{\mathbf{f}}^B, \underline{\mathbf{f}}, \boldsymbol{\tau}$ ) but only estimated through the algorithm.

The MAP algorithm represents, in a sense, the probabilistic way to estimate those quantities for which a direct measure does not exist. We consider the goodness in the estimation of the measurable quantities as a parameter of reliability of the method in estimating those variables that are not directly measurable. The leading idea is to compare the same variables (measured and then estimated) in order to prove the quality of the proposed algorithm.

Subjects of Table 5.1 were asked to perform tasks T1 and T2 equipped with the Xsens suit for the motion tracking and the ftShoes prototype for computing the ground reaction forces.

Xsens data were acquired at 240 Hz through the MVN Studio software, ftShoes data at 100 Hz through the YARP driver. Data were synchronized and downsampled in post-processing phase by means of Matlab. A 48-DoF model template was used both for the URDF and for the OpenSim model, ( $\mathbf{d} \in \mathbb{R}^{1248}$ ). The IK was computed by using the OpenSim API for Matlab and a Savitzky-Golay filtering (3-th order, 57-elements moving window) was used for retrieving joint velocities  $\dot{\mathbf{q}}$  and accelerations  $\ddot{\mathbf{q}}$ . The MAP settings were tuned as follows:  $\boldsymbol{\Sigma}_d = 10^4$  (i.e., no reliable prior on vector  $\mathbf{d}$ ),  $\boldsymbol{\Sigma}_D = 10^{-4}$  (i.e., high reliable prior on the dynamic model),  $\boldsymbol{\Sigma}_y$  composed of each sensor variance submatrix (IMUs  $\approx 10^{-3}$ , joint acceleration  $\approx 10^{-3}$ , external forces on the feet  $\approx 10^{-3}$  and on the other links of the model  $\approx 10^{-6}$ ).

The analysis shows the comparison between the measure and the estimation for the external forces, linear accelerations and joint accelerations of certain links/joints of the model. Their choice was task-driven by considering those links/joints mainly involved in the tasks. The analysis has been performed for all the subjects in Table 5.1 along with a RMSE investigation for the external forces (Table 5.3), the linear accelerations (Table 5.4) and the joint accelerations (Table 5.5). However, the following figures refer to one subject (i.e., S2) and they have to be interpreted in the following way: the three columns are the  $x$ - $y$ - $z$  components; the rows are related to the link/joint chosen for the evaluation. Blank plots mean that there is not a related quantity for that component (depending on the joint DoFs).

Figure 5.8 shows the comparison between the external force [ N ] measured (in red) and estimated by the algorithm (in blue) for the right foot<sup>4</sup>. Figure 5.9 shows

<sup>4</sup>The similar analysis on the left foot is not retrieved since the left foot is the fixed base of the

the comparison between the linear acceleration [ $\text{m/s}^2$ ] measured by sensors (in red) and estimated quantity (in blue) by the algorithm for right upper arm, forearm and hand links, respectively, in the tasks T1 (on top) and T2 (on bottom). Figure 5.10 shows the same analysis for the related left links. Similarly, the comparison between the joint acceleration [ $\text{rad/s}^2$ ] (assumed to be) measured by the class of ‘fictitious’ DoF-acceleration sensors (in red) and the related estimation (in blue) via MAP is shown for the right (in Figure 5.11) and for the left (in Figure 5.12) shoulder, elbow and wrist joints, respectively, for T1 (on top) and T2 (on bottom).

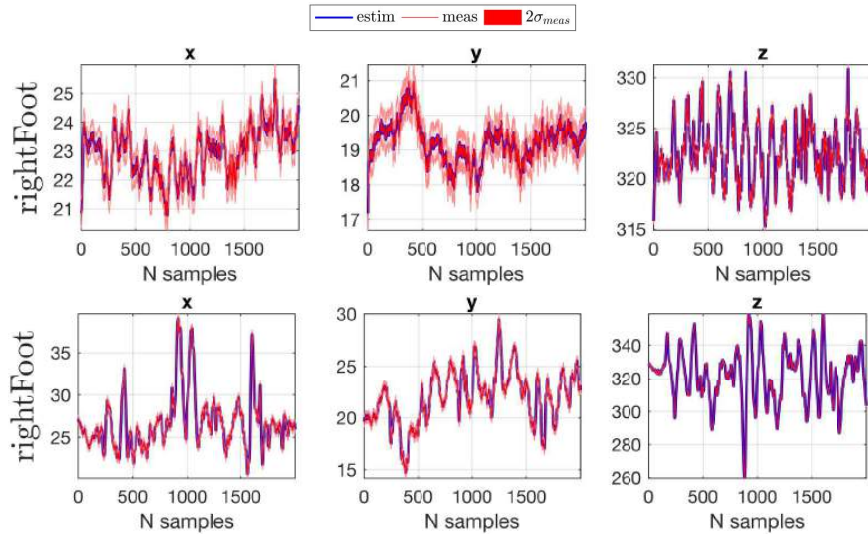


Fig. 5.8 External force [N] comparison. The plots show the measured quantity (with  $2\sigma$  standard deviation, in red) and the MAP estimation (in blue) and for the S2 right foot link in the tasks T1 (top) and T2 (bottom).

model. In general, the iDynTree library [Nori et al., 2015b] used here for describing the dynamics of the model does not support the application of any kind of sensor on the fixed base and therefore neither the estimation of its dynamics.

Table 5.3 RMSE analysis of the force [ N ] estimation w.r.t. the related measured quantity. (Subjects S1, S2, S3, S4, S5; tasks T1, T2).

Subject	Task	rightFoot
S1	T1	$f_x$ 0.0024
		$f_y$ 0.0010
		$f_z$ 0.0211
	T2	$f_x$ 0.0028
		$f_y$ 0.0029
		$f_z$ 0.0215
S2	T1	$f_x$ $6.2968 \cdot 10^{-4}$
		$f_y$ $3.4981 \cdot 10^{-4}$
		$f_z$ 0.0185
	T2	$f_x$ 0.0033
		$f_y$ 0.0058
		$f_z$ 0.0188
S3	T1	$f_x$ 0.0079
		$f_y$ 0.0065
		$f_z$ 0.0246
	T2	$f_x$ 0.0095
		$f_y$ 0.0080
		$f_z$ 0.0247
S4	T1	$f_x$ 0.0141
		$f_y$ 0.0116
		$f_z$ 0.0272
	T2	$f_x$ 0.0208
		$f_y$ 0.0184
		$f_z$ 0.0282
S5	T1	$f_x$ 0.0063
		$f_y$ 0.0051
		$f_z$ 0.0206
	T2	$f_x$ 0.0072
		$f_y$ 0.0076
		$f_z$ 0.0211

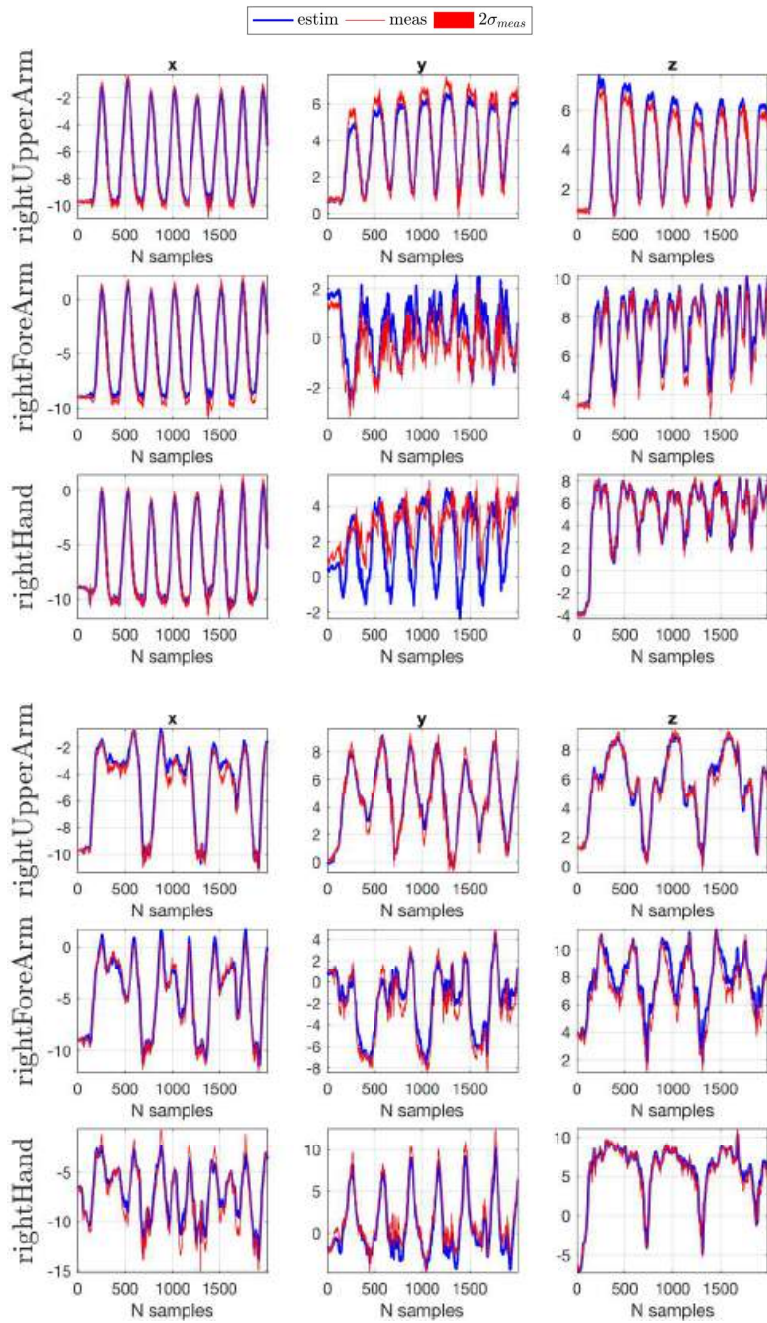


Fig. 5.9 Linear acceleration [ $m/s^2$ ] comparison. The plots show the estimate (in blue) and the measured quantity (with  $2\sigma$  standard deviation, in red) for the S2 right upper arm, forearm and hand links, respectively, in the tasks T1 (top) and T2 (bottom).

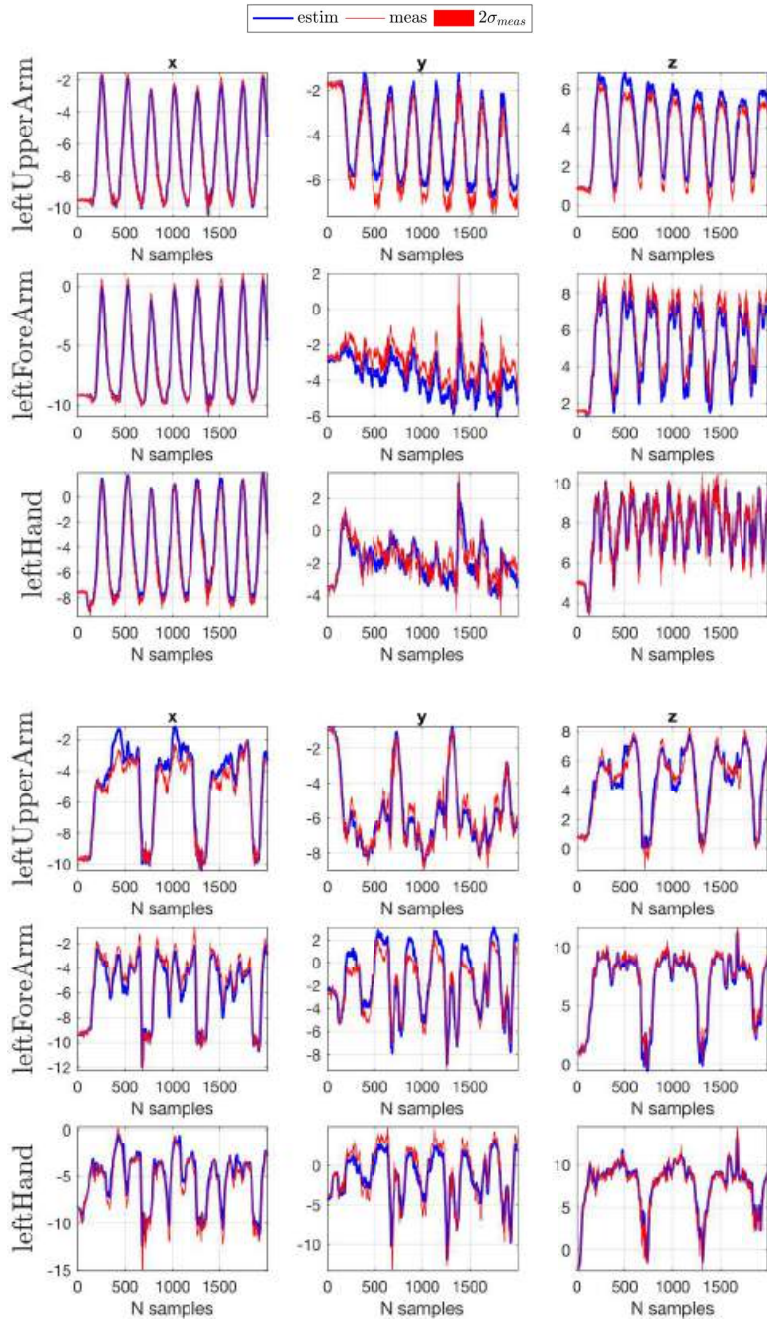


Fig. 5.10 Linear acceleration [ m/s<sup>2</sup>] comparison. The plots show the estimate (in blue) and the measured quantity (with 2σ standard deviation, in red) for the S2 left upper arm, forearm and hand links, respectively, in the tasks T1 (top) and T2 (bottom).

Table 5.4 RMSE analysis of the linear acceleration [ m/s<sup>2</sup>] estimation w.r.t. the related measured quantity. (Subjects S1, S2, S3, S4, S5; tasks T1, T2).

Subject	Task							
		<i>rightUpperArm</i>	<i>rightForeArm</i>	<i>rightHand</i>	<i>leftUpperArm</i>	<i>leftForeArm</i>	<i>leftHand</i>	
S1	T1	<i>a<sub>x</sub></i>	1.23	1.67	0.49	0.24	0.20	0.37
		<i>a<sub>y</sub></i>	0.68	1.07	1.01	0.58	1.03	0.45
		<i>a<sub>z</sub></i>	0.79	1.17	0.92	0.34	0.57	0.75
	T2	<i>a<sub>x</sub></i>	1.65	1.83	1.17	1.03	1.01	1.09
		<i>a<sub>y</sub></i>	1.82	1.26	1.73	0.87	1.80	1.86
		<i>a<sub>z</sub></i>	1.41	1.11	2.55	0.87	1.16	1.45
S2	T1	<i>a<sub>x</sub></i>	0.28	0.49	0.26	0.18	0.34	0.46
		<i>a<sub>y</sub></i>	0.41	0.75	1.66	0.60	0.90	0.64
		<i>a<sub>z</sub></i>	0.42	0.60	0.38	0.52	0.70	0.33
	T2	<i>a<sub>x</sub></i>	0.47	0.55	0.86	0.69	0.68	0.81
		<i>a<sub>y</sub></i>	0.43	0.97	1.09	0.48	0.89	1.21
		<i>a<sub>z</sub></i>	0.37	0.82	0.54	0.56	0.46	0.53
S3	T1	<i>a<sub>x</sub></i>	0.17	0.17	0.30	0.51	0.55	0.45
		<i>a<sub>y</sub></i>	0.36	0.64	0.50	0.59	0.73	1.67
		<i>a<sub>z</sub></i>	0.34	0.41	0.52	1.02	0.42	0.56
	T2	<i>a<sub>x</sub></i>	0.29	0.46	0.38	0.82	0.92	0.51
		<i>a<sub>y</sub></i>	0.51	0.75	0.91	1.59	1.74	3.18
		<i>a<sub>z</sub></i>	0.40	0.36	0.51	1.26	1.42	1.40
S4	T1	<i>a<sub>x</sub></i>	0.40	0.64	0.31	0.27	0.36	0.34
		<i>a<sub>y</sub></i>	0.41	0.64	0.74	0.40	0.49	0.77
		<i>a<sub>z</sub></i>	0.34	0.54	0.60	0.29	0.33	0.64
	T2	<i>a<sub>x</sub></i>	1.11	1.08	1.24	0.80	1.09	2.05
		<i>a<sub>y</sub></i>	0.67	1.53	1.67	1.05	1.28	1.91
		<i>a<sub>z</sub></i>	0.57	1.01	1.05	0.66	0.60	0.73
S5	T1	<i>a<sub>x</sub></i>	0.34	0.51	0.72	0.32	0.30	0.76
		<i>a<sub>y</sub></i>	0.65	0.72	1.06	0.57	0.57	1.17
		<i>a<sub>z</sub></i>	0.43	0.33	1.03	0.61	0.41	0.75
	T2	<i>a<sub>x</sub></i>	0.32	0.58	0.87	0.52	0.62	1.03
		<i>a<sub>y</sub></i>	0.55	0.83	0.78	0.54	1.02	1.09
		<i>a<sub>z</sub></i>	0.38	0.39	0.69	0.87	0.94	0.95

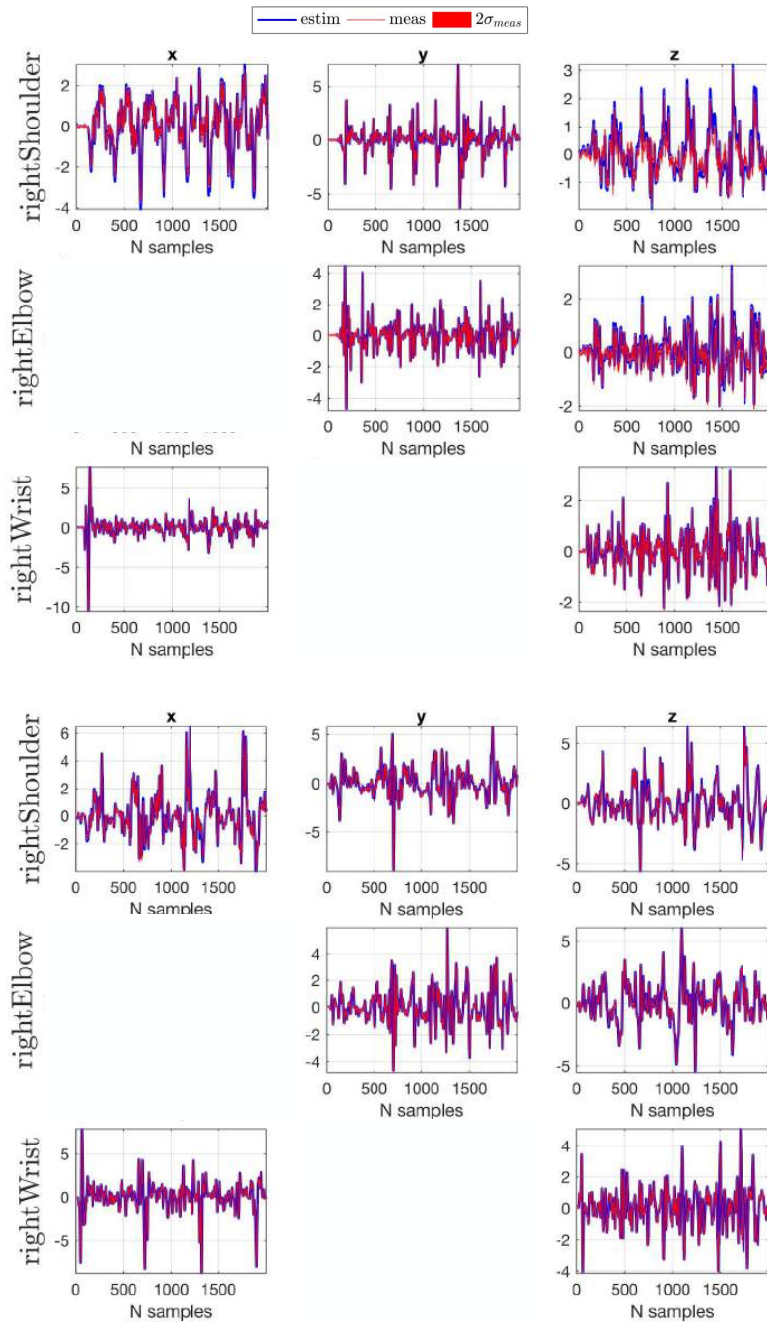


Fig. 5.11 Joint acceleration [ $\text{rad/s}^2$ ] comparison. The plots show the estimate (in blue) and the measured quantity (with  $2\sigma$  standard deviation, in red) for the S2 right shoulder, elbow and wrist joints, respectively, in the tasks T1 (top) and T2 (bottom).

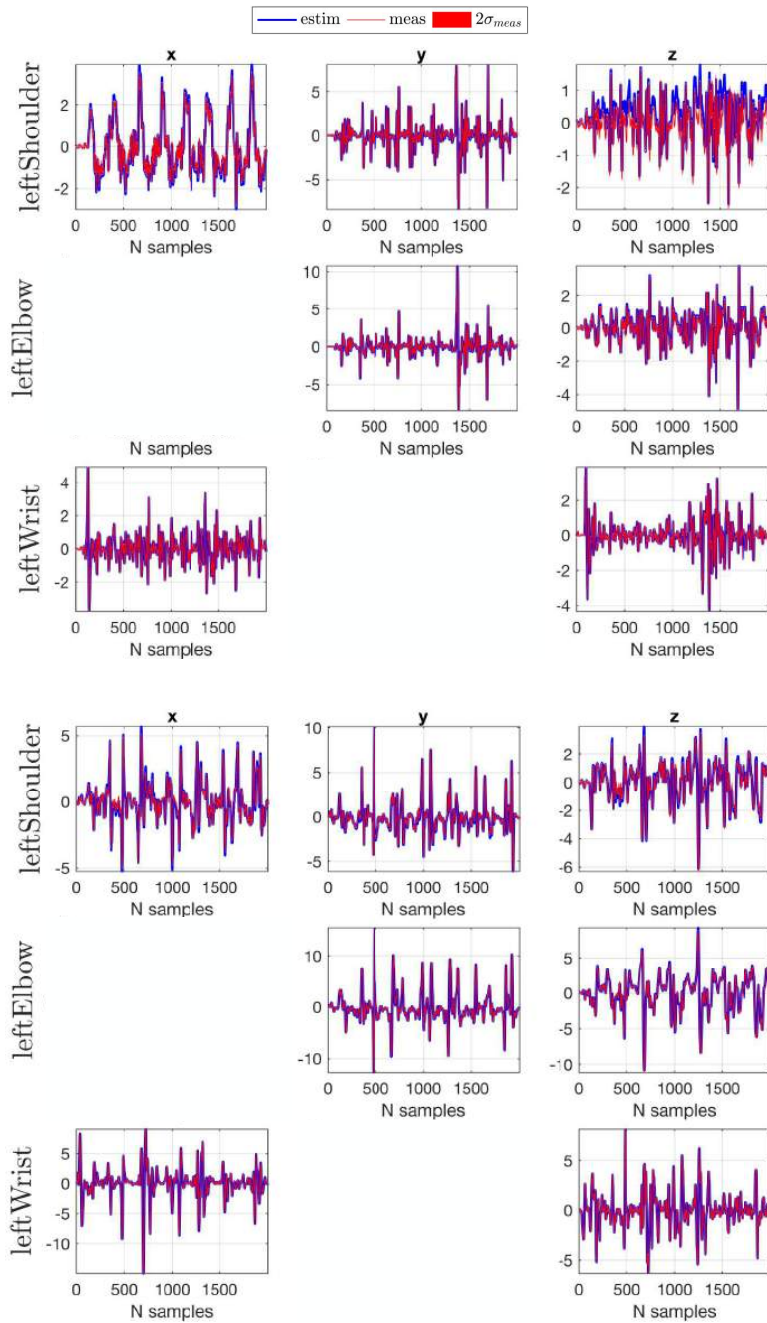


Fig. 5.12 Joint acceleration [ $\text{rad/s}^2$ ] comparison. The plots show the estimate (in blue) and the measured quantity (with  $2\sigma$  standard deviation, in red) for the S2 left shoulder, elbow and wrist joints, respectively, in the tasks T1 (top) and T2 (bottom).

Table 5.5 RMSE analysis of the joint acceleration [rad/s<sup>2</sup>] estimation w.r.t. the related measured quantity. (Subjects S1, S2, S3, S4, S5; tasks T1, T2).

Subject	Task							
		<i>rightShoulder</i>	<i>rightElbow</i>	<i>rightWrist</i>	<i>leftShoulder</i>	<i>leftElbow</i>	<i>leftWrist</i>	
S1	T1	$\ddot{q}_x$	0.30		0.03	0.27		0.02
		$\ddot{q}_y$	0.09	0.11		0.04	0.01	
		$\ddot{q}_z$	0.22	0.30	0.02	0.20	0.14	0.02
	T2	$\ddot{q}_x$	0.73		0.09	0.22		0.05
		$\ddot{q}_y$	0.53	0.20		0.50	0.26	
		$\ddot{q}_z$	0.82	0.39	0.05	0.38	0.38	0.06
S2	T1	$\ddot{q}_x$	0.13		0.02	0.14		0.02
		$\ddot{q}_y$	0.05	0.04		0.04	0.03	
		$\ddot{q}_z$	0.23	0.13	0.05	0.27	0.08	0.01
	T2	$\ddot{q}_x$	0.12		0.02	0.19		0.03
		$\ddot{q}_y$	0.08	0.03		0.13	0.06	
		$\ddot{q}_z$	0.10	0.08	0.03	0.16	0.14	0.03
S3	T1	$\ddot{q}_x$	0.22		0.02	0.36		0.06
		$\ddot{q}_y$	0.02	0.04		0.13	0.11	
		$\ddot{q}_z$	0.24	0.13	0.02	0.19	0.20	0.03
	T2	$\ddot{q}_x$	0.13		0.02	0.44		0.10
		$\ddot{q}_y$	0.16	0.06		0.76	0.66	
		$\ddot{q}_z$	0.38	0.22	0.03	0.53	0.41	0.06
S4	T1	$\ddot{q}_x$	0.27		0.02	0.26		0.03
		$\ddot{q}_y$	0.02	0.03		0.03	0.01	
		$\ddot{q}_z$	0.17	0.07	0.03	0.23	0.12	0.03
	T2	$\ddot{q}_x$	0.24		0.03	0.25		0.06
		$\ddot{q}_y$	0.27	0.06		0.34	0.14	
		$\ddot{q}_z$	0.40	0.31	0.06	0.27	0.28	0.06
S5	T1	$\ddot{q}_x$	0.29		0.04	0.30		0.04
		$\ddot{q}_y$	0.06	0.05		0.07	0.07	
		$\ddot{q}_z$	0.31	0.15	0.03	0.38	0.13	0.02
	T2	$\ddot{q}_x$	0.14		0.03	0.17		0.04
		$\ddot{q}_y$	0.14	0.04		0.32	0.11	
		$\ddot{q}_z$	0.17	0.10	0.02	0.30	0.24	0.03

Hereafter, the human joint torque estimated by the MAP algorithm. No direct comparison with the related measured quantity is possible in this case.

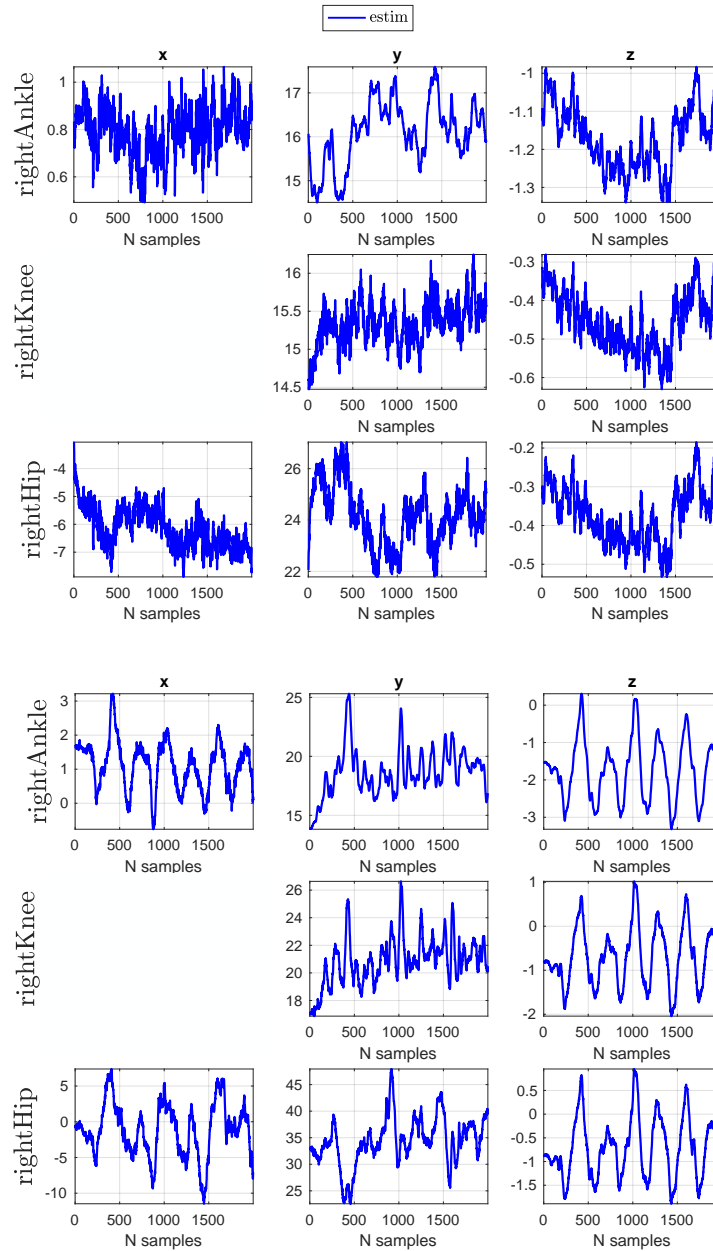


Fig. 5.13 Joint torque [ Nm] estimation for the S2 right ankle, knee and hip joints, respectively, in the tasks T1 (top) and T2 (bottom).

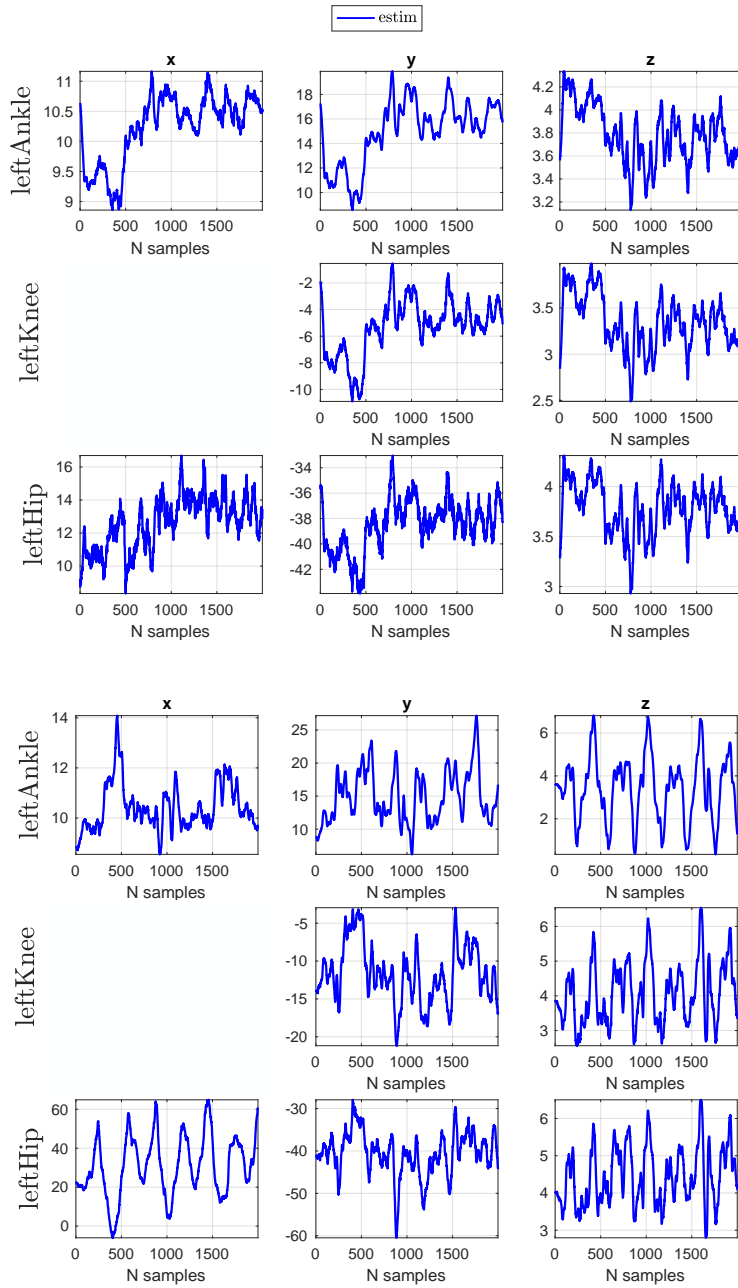


Fig. 5.14 Joint torque [ Nm] estimation for the S2 left ankle, knee and hip joints, respectively, in the tasks T1 (top) and T2 (bottom).

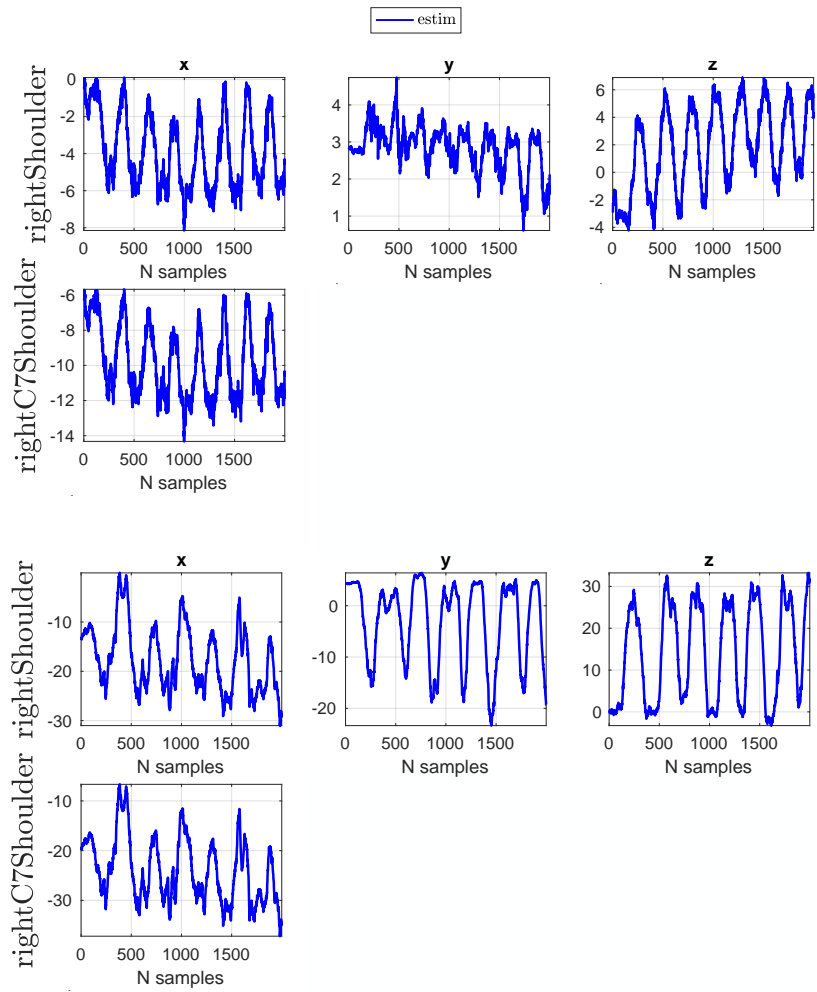


Fig. 5.15 Joint torque [ Nm] estimation for the S2 right shoulder and C7 shoulder joints, respectively, in the tasks T1 (top) and T2 (bottom).

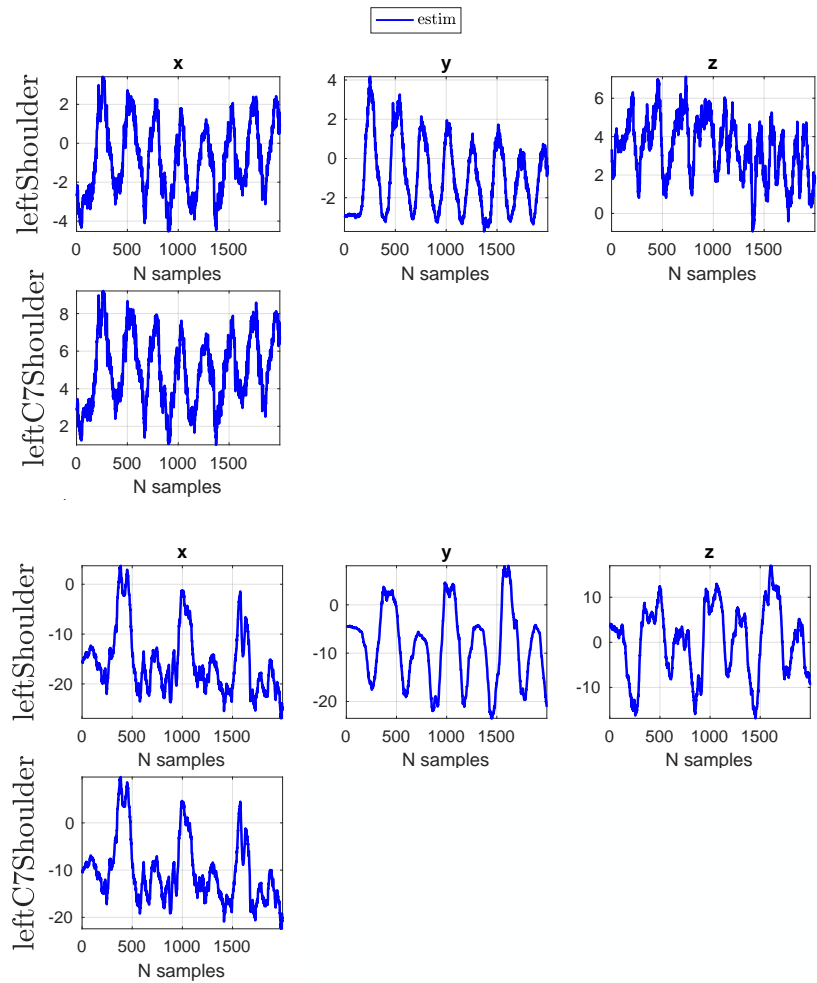


Fig. 5.16 Joint torque [ Nm] estimation for the S2 left shoulder and C7 shoulder joints, respectively, in the tasks T1 (top) and T2 (bottom).

Figures from 5.13 to 5.16 show the joint torque estimation for the right and left ankle, knee, hip, shoulder and C7 shoulder joints, respectively.

### 5.3.3 Incremental Sensor Fusion Analysis

As previously said, the novelty of the MAP framework consists in replacing the classical RNEA boundary conditions with readings coming from different types of sensors. In this Section, we discuss the benefits of the multi-sensor data fusion for solving the estimation problem by characterizing the effects of the data fusion on the covariance of the estimator. The benefit of the MAP is such that the more sensors we use in the estimation, the better the estimation itself will be. Let us consider writing Equations (4.33a) and (4.35a) in a more compact form, such as

$$\Sigma_{d|y} = \left( D^\top \Sigma_D^{-1} D + \Sigma_d^{-1} + Y^\top \Sigma_{y|d}^{-1} Y \right)^{-1}. \quad (5.1)$$

Let us assume  $m$  multiple statistically independent measurements

$$\begin{aligned} \mathbf{y}_1 &= \mathbf{Y}_1 \mathbf{d} + \mathbf{b}_{Y_1}, \\ \mathbf{y}_2 &= \mathbf{Y}_2 \mathbf{d} + \mathbf{b}_{Y_2}, \\ &\vdots \\ \mathbf{y}_m &= \mathbf{Y}_m \mathbf{d} + \mathbf{b}_{Y_m}, \end{aligned}$$

this yields to a diagonal structure for the matrix  $\Sigma_{y|d}^{-1}$ . Thus, we have:

$$\begin{aligned} Y^\top \Sigma_{y|d}^{-1} Y &= \begin{bmatrix} \mathbf{Y}_1^\top & \mathbf{Y}_2^\top & \dots & \mathbf{Y}_m^\top \end{bmatrix} \begin{bmatrix} \Sigma_{y_1|d}^{-1} & \mathbf{0} & \dots & \mathbf{0} \\ \mathbf{0} & \Sigma_{y_2|d}^{-1} & \dots & \mathbf{0} \\ \vdots & \vdots & \ddots & \vdots \\ \mathbf{0} & \mathbf{0} & \dots & \Sigma_{y_m|d}^{-1} \end{bmatrix} \begin{bmatrix} \mathbf{Y}_1 \\ \mathbf{Y}_2 \\ \vdots \\ \mathbf{Y}_m \end{bmatrix} \\ &= \mathbf{Y}_1^\top \Sigma_{y_1|d}^{-1} \mathbf{Y}_1 + \mathbf{Y}_2^\top \Sigma_{y_2|d}^{-1} \mathbf{Y}_2 + \dots + \mathbf{Y}_m^\top \Sigma_{y_m|d}^{-1} \mathbf{Y}_m. \end{aligned} \quad (5.3)$$

With an abuse of notation, let  $d|y_m$  be the estimator which exploits all the measurements from  $y_1$  up to  $y_m$ . The addition of each measurement induces changes into the associated covariance matrix according to the following recursive equation:

$$\Sigma_{d|y_m}^{-1} = \Sigma_{d|y_{m-1}}^{-1} + \mathbf{Y}_m^\top \Sigma_{y_m}^{-1} \mathbf{Y}_m, \quad (5.4)$$

where, for  $m = 1$ , the initial condition is

$$\Sigma_{d|y_0}^{-1} = D^\top \Sigma_D^{-1} D + \Sigma_d^{-1}. \quad (5.5)$$

A situation of two sets of measurements equations is here evaluated for the subjects in Table 5.1, for tasks T1 and T2. In particular, the measurements equation (4.14) is built for two different cases:

$$CASE 1 \quad \mathbf{y} = \left[ \mathbf{y}_{\ddot{q}} \quad \mathbf{y}_{f_{ftShoe,fb}^x} \quad \mathbf{y}_{f^x} \right]^T \in \mathbb{R}^{342}, \quad (5.6a)$$

$$CASE 2 \quad \mathbf{y} = \left[ \mathbf{y}_{IMUs} \quad \mathbf{y}_{\ddot{q}} \quad \mathbf{y}_{f_{ftShoe,fb}^x} \quad \mathbf{y}_{f^x} \right]^T \in \mathbb{R}^{390}. \quad (5.6b)$$

The MAP algorithm is performed twice by including as set of sensors firstly Equation (5.6a) and then Equation (5.6b). The attempt is to prove that, by adding (e.g., increasing) progressively different sensors data, the variance associated to the estimated dynamic variables consequently decreases at each MAP computation, by making the estimation more reliable. By passing progressively from *CASE 1* to *CASE 2* the variance associated to the torques decreases. Figure 5.17 shows the decreasing behaviour of the 5-subjects mean torque variances from *CASE 1* (in orange) to *CASE 2* (in violet) for both left and right ankle, hip joints, respectively and L5S1, L4L3, L1T12 joints. The two plots are for the tasks T1 (5.17a) and T2 (5.17b).

The variance values at the ankles do not change significantly among the two cases since the ankle torque estimation depends mostly on the readings of the ft-Shoes that are included in both of them. Conversely, an ever-growing decreasing behaviour is present starting from the values associated to the hips towards the L1T12 joint on the torso. This because as we are considering joints always further apart from the feet, the ftShoes contribution to the estimation has a lower weight than at the feet while the contribution of the IMUs becomes more important (i.e., weights more). In Table 5.6 detailed values of the analysis per each subject are reported.

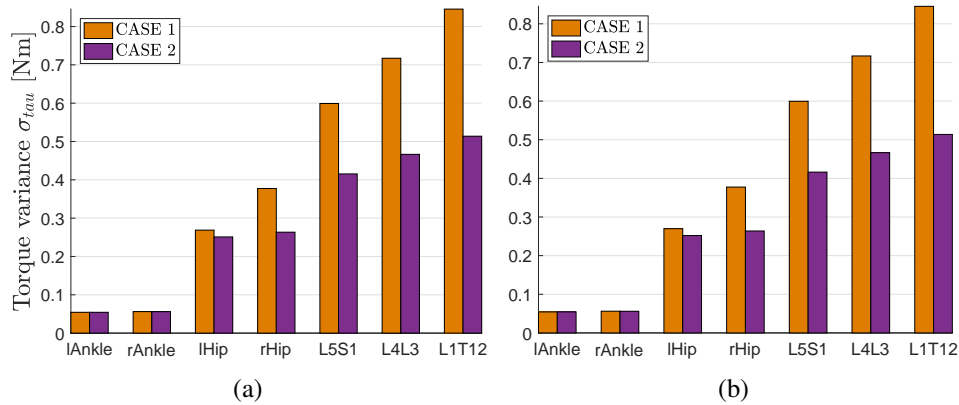


Fig. 5.17 5-subjects mean torque variance [Nm] by using two different versions of the measurements equation: *CASE 1* (in orange) and *CASE 2* (in violet), for both left and right ankle, hip joints, respectively and L5S1, L4L3, L1T12 joints. Plots are referred to tasks (a) T1 and (b) T2.

Table 5.6 Torque variance  $\sigma_{tau}$  [Nm] for both *CASE 1* and *CASE 2*. (Subjects S1, S2, S3, S4, S5; tasks T1, T2).

Subject	Task	CASE	lAnkle	rAnkle	lHip	rHip	L5S1	L4L3	L1T12
S1	T1	1	0.0544	0.0560	0.2608	0.3643	0.5696	0.6938	0.8240
		2	0.0544	0.0559	0.2446	0.2568	0.4009	0.4572	0.5064
	T2	1	0.0544	0.0561	0.2613	0.3649	0.5703	0.6937	0.8244
		2	0.0544	0.0560	0.2449	0.2574	0.4015	0.4570	0.5064
S2	T1	1	0.0543	0.0562	0.2495	0.3289	0.5255	0.6079	0.6978
		2	0.0543	0.0561	0.2378	0.2483	0.3924	0.4315	0.4682
	T2	1	0.0544	0.0562	0.2515	0.3244	0.5227	0.6072	0.6971
		2	0.0544	0.0561	0.2395	0.2455	0.3911	0.4317	0.4684
S3	T1	1	0.0544	0.0561	0.2791	0.3979	0.6468	0.7696	0.9056
		2	0.0544	0.0560	0.2594	0.2716	0.4361	0.4866	0.5351
	T2	1	0.0544	0.0561	0.2796	0.3984	0.6473	0.7697	0.9058
		2	0.0544	0.0560	0.2598	0.2722	0.4366	0.4868	0.5354
S4	T1	1	0.0544	0.0563	0.3013	0.4558	0.7161	0.8658	1.0300
		2	0.0544	0.0561	0.2742	0.9172	0.4567	0.5149	0.5702
	T2	1	0.0544	0.0564	0.3013	0.4559	0.7153	0.8642	1.0288
		2	0.0544	0.0561	0.2743	0.2924	0.4567	0.5141	0.5693
S5	T1	1	0.0544	0.0561	0.2530	0.3401	0.5779	0.6491	0.7700
		2	0.0544	0.0560	0.2394	0.2487	0.3913	0.4422	0.4894
	T2	1	0.0544	0.0562	0.2554	0.3439	0.5423	0.6495	0.7702
		2	0.0544	0.0560	0.2416	0.2518	0.3950	0.4425	0.4894

## 5.4 An Experiment with the iCub

The analysis, performed in the previous section, is here shown in a variant that encompasses the robot iCub. Data were collected at Istituto Italiano di Tecnologia, on a 48-DoF human model ( $d \in \mathbb{R}^{1248}$ ). The experimental setup encompassed *i*) the Xsens suit for the motion tracking, *ii*) two standard AMTI OR6 force platforms to acquire the ground reaction wrenches, *iii*) the F/T sensors of the robot arms. ftShoes were not used in the experiment since they did not exist at that time. Kinematic data were acquired at a frequency of 240 Hz. Each platform acquired a sample at a frequency of 1 kHz by using AMTI acquisition units.

Experiments were conducted on the iCub [Metta et al., 2010], a full-body humanoid robot with 53 DoFs: 6 in the head, 16 in each arm, 3 in the torso and 6 per each leg. The iCub is endowed with whole-body distributed F/T sensors, accelerometers, gyroscopes and tactile sensors. Specifically, the limbs are equipped

with six F/T sensors placed in the upper arms, in the upper legs and in the ankles. Internal joint torques and external wrenches are estimated through a whole-body estimation algorithm [Nori et al., 2015b]. Robot data were collected at a frequency of 100 Hz.

Ten healthy adult subjects (as in Table 5.7) have been recruited for the experimental session. Each subject was asked to wear the Xsens suit and to stand on the force plates by positioning one foot per platform. The robot was located in front of the subject facing him at a known position w.r.t. the human foot location (Figure 5.18a). The mutual feet position was fixed for all the trials and defined by a printed fixture located under both feet (Figure 5.18b) The interaction implied that the human grasped and pushed down both the robot arms while performing a bowing task (Figure 5.19).

As in Section 5.3.2, even here the MAP algorithm was able to estimate  $\mathbf{d}$  for all the links/joints in the model. As in the previous dataset, the MAP results are here shown for one subject (i.e., S1). Figure 5.20a shows the comparison for the external forces measured (in red) and estimated (in blue) for the right foot<sup>5</sup> and for both the human hands since during the interaction there are forces acting on them. The same comparison concerning the linear acceleration for the right foot, upper leg and hand, respectively, is shown in Figure 5.20b. Similar analysis in Figure 5.21a for the joint acceleration, for the right ankle and the hips. Again here, like in the previous case, the MAP algorithm is able to give us a suitable estimation of the human joint torques, Figure 5.21b.

Table 5.7 Subjects eligible for the pHRI analysis. Each subject was provided of a written informative consent before starting the experiment.

Subject	Gender	Age	Height [ cm]	Mass [ kg]
S1	F	30	165	60.8
S2	F	32	166	67.3
S3	M	29	161	54.4
S4	M	28	172	64.1
S5	F	25	171	58.7
S6	F	27	169	65.4
S7	F	24	170	68.2
S8	F	24	165	52.8
S9	M	40	169	65.4
S10	M	29	158	54.4

<sup>5</sup>No left foot as previously motivated.

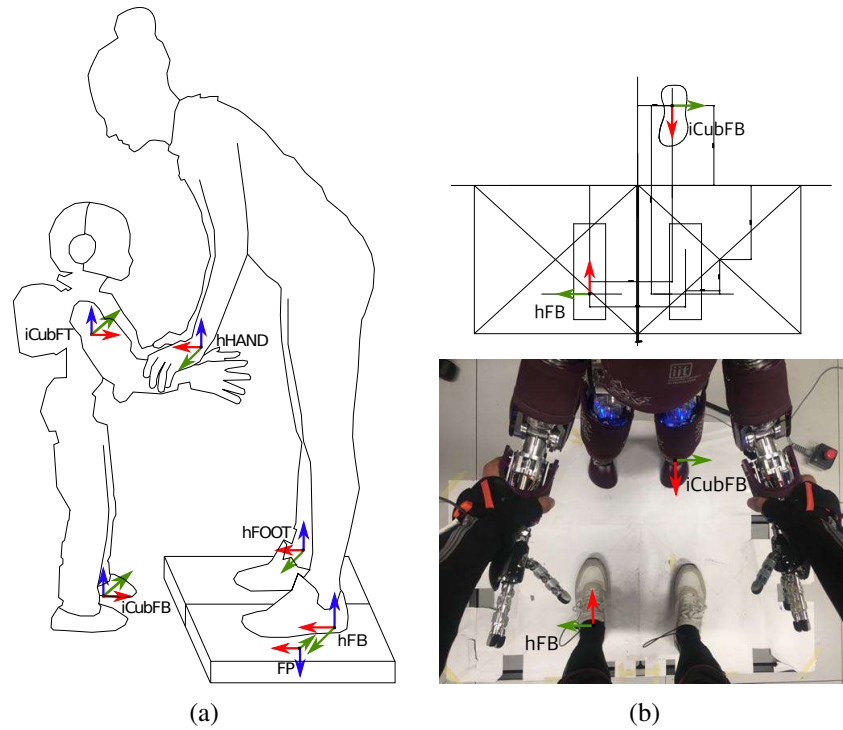
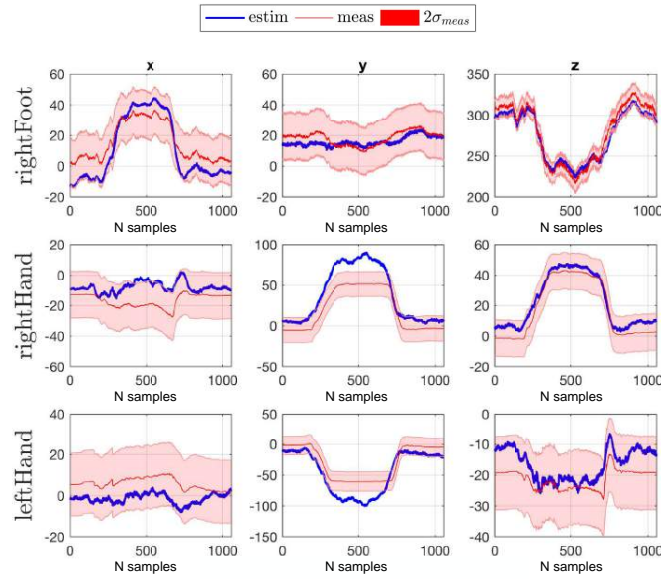


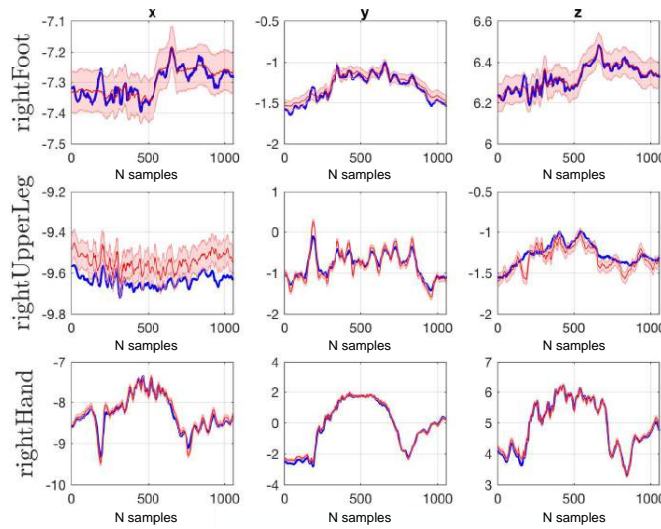
Fig. 5.18 (a) Human subject that grasps and pushes down the robot arms. The figure shows the reference frames for the F/T sensor of the robot ( $iCubFT$ ), the robot fixed base ( $iCubFB$ ), the force plate ( $FP$ ), the human fixed base ( $hFB$ ), the human foot and hand ( $hFOOT$ ,  $hHAND$ ), respectively. (b) The mutual feet position is defined by a fixture located under both the feet.



Fig. 5.19 Human subject while performing the bowing task with the iCub.

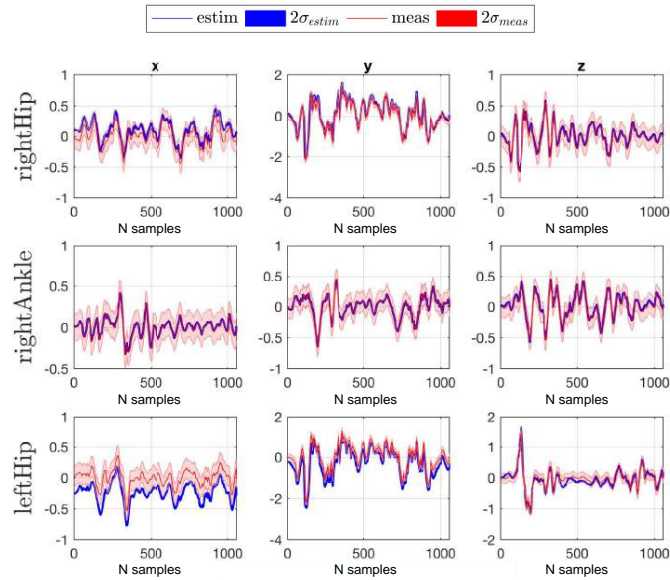


(a) External force [ N ]

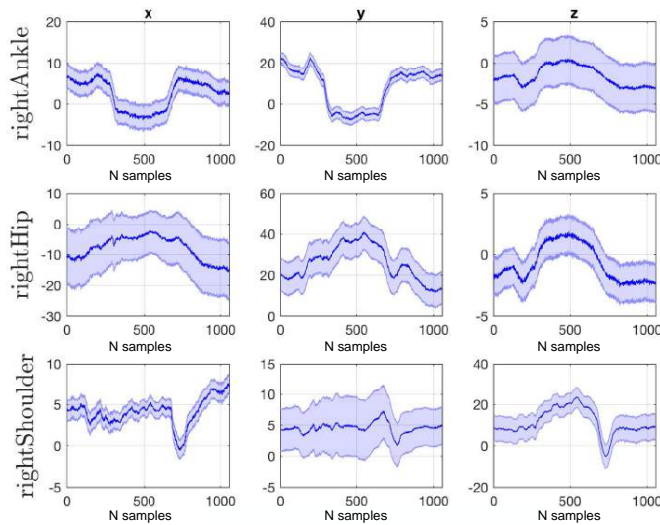


(b) Linear acceleration [  $m/s^2$  ]

Fig. 5.20 Comparison between the variables measured (with  $2\sigma$  standard deviation, in red) and their MAP estimation (in blue) for (a) the external force  $f^x$  for the S1 right foot and both the hands links, and (b) the linear acceleration on the S1 right foot, upper leg and hand links, respectively.



(a) Joint acceleration [ rad/s<sup>2</sup>]



(b) Joint torque [ Nm]

Fig. 5.21 (a) Joint acceleration comparison between the variables measured (with  $2\sigma$  standard deviation, in red) and their MAP estimation (in blue) for the S1 hips and right ankle joints. (b) Joint torque MAP estimation (with  $2\sigma$  estimated standard deviation) for the S1 right ankle, hip and shoulder joints, respectively.

As in the Section 5.3.3 analysis, an investigation by adding progressively different sensors has been done on the MAP computation. The set of measurements equation (4.14) is here composed as follows:

$$\text{CASE 1} \quad \mathbf{y} = \left[ \mathbf{y}_{\ddot{\mathbf{q}}} \quad \mathbf{y}_{f_{FP,fb}^x} \quad \mathbf{y}_{f^x} \right]^\top \in \mathbb{R}^{330}, \quad (5.7a)$$

$$\text{CASE 2} \quad \mathbf{y} = \left[ \mathbf{y}_{IMUs} \quad \mathbf{y}_{\ddot{\mathbf{q}}} \quad \mathbf{y}_{f_{FP,fb}^x} \quad \mathbf{y}_{f^x} \right]^\top \in \mathbb{R}^{378}, \quad (5.7b)$$

$$\text{CASE 3} \quad \mathbf{y} = \left[ \mathbf{y}_{IMUs} \quad \mathbf{y}_{\ddot{\mathbf{q}}} \quad \mathbf{y}_{f_{FP,fb}^x} \quad \mathbf{y}_{f_{iCubF/T}^x} \right]^\top \in \mathbb{R}^{390}. \quad (5.7c)$$

Even in this case the analysis reveals the important decreasing behaviour as in Figure 5.17. By passing progressively from *CASE 1* to *CASE 3* the variance associated to the 10-subjects mean torques decreases, Figure 5.22. Again, the variance values on the ankles do not change significantly among the three configurations since the ankles torque estimation depends mostly on the contribution of the force plates that are included in all the three cases. And for the same previous reason, the decreasing behaviour becomes to be evident at the hips since the torque estimation at the hips is affected by the complete set of sensors (i.e., contribution of the force plates weights lower, contribution of IMUs + F/T iCub sensors weights more).

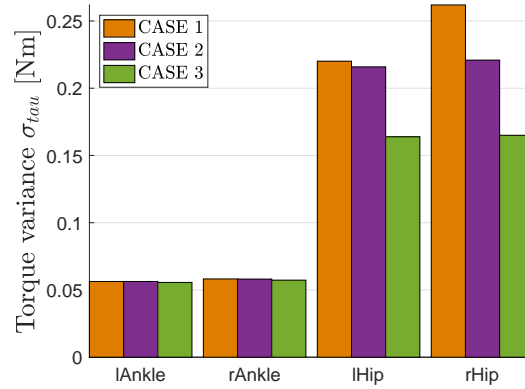


Fig. 5.22 10-subjects mean torque variance [Nm] by using three different combinations of the measurements equation: *CASE 1* (in orange), *CASE 2* (in violet) and *CASE 3* (in green), for both left and right ankle, hip joints, respectively, for the pHRI bowing task.

### 5.4.1 MAP vs. OpenSim Dynamics Estimation

To test the quality of our estimation w.r.t. a ground-truth tool, one subject of Table 5.7 was asked to perform four repetitions of the bowing task in two different configurations, i.e., *with* and *without* an additional mass  $W$  of 6 kg roughly positioned in correspondence of the torso center of mass. The MAP computation was performed by considering the following cases as algorithm inputs (see Table 5.8).

Table 5.8 Cases for the MAP vs. OpenSim evaluation.

	<i>CASE A</i>	<i>CASE B</i>
<b>URDF model</b>	without $W$	without $W$
<b>measurements</b>	with $W$	without $W$
$\Sigma_D$	$10^{-1}$	$10^{-4}$
<b><math>\tau</math> estimation</b>	$\tau_{(model+6\text{ kg})}$	$\tau_{model}$

In both the cases the analysis is performed with the same URDF model of the subject. In order to highlight a lower reliability for the *CASE A*, it is assigned a value to  $\Sigma_D$  equal to  $10^{-1}$  (different from the value  $10^{-4}$  assigned for the *CASE B*).

By exploiting the linearity property of the system we consider the following expression for the torques:

$$\tau_{(model+6\text{ kg})} - \tau_{model} = \tau_{6\text{ kg}} , \quad (5.8)$$

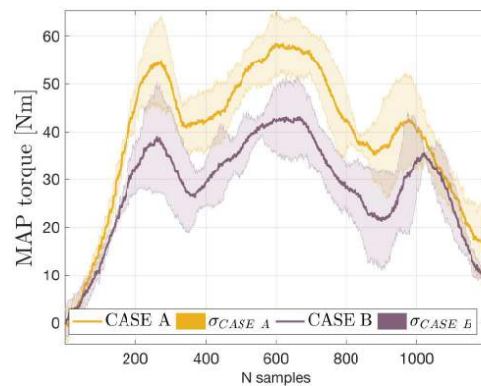
where  $\tau_{6\text{ kg}}$  is the theoretical torque due to the additional  $W$  positioned on the torso<sup>6</sup>. Figure 5.23 shows the mean and the  $\sigma$  standard deviation of the torque estimation at the hips (i.e., the sum of the torque estimated at each hip) by means of the MAP algorithm (Figure 5.23a) and the OpenSim ID toolbox (Figure 5.23b), respectively.

Given Equation (5.8), it is possible to retrieve the error  $\varepsilon_\tau$  on the  $\tau$  estimation due to the presence of the weight  $W$ :

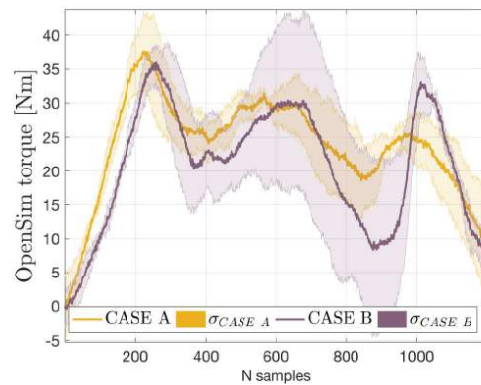
$$\varepsilon_\tau = |\tau_{(model+6\text{ kg})} - \tau_{model}| - \tau_{6\text{ kg}} . \quad (5.9)$$

<sup>6</sup>We consider a simple 2-DoF system (see [Latella et al., 2016]) in which the position of  $W$  and the hip joint angle are known.

Equation (5.9) has been computed for both the estimators in order to evaluate its effectiveness w.r.t the modelling errors. The error is higher in OpenSim ID computation (6.45 Nm) than in the MAP estimation (3.69 Nm) since OpenSim does not offer the possibility of setting the model reliability in the computation. This highlights that the MAP algorithm is a method more robust to the modelling errors since it gives the possibility of weighting the reliability of the model by properly tuning the related covariance matrix.



(a)



(b)

Fig. 5.23 Mean and  $\sigma$  standard deviation of the hips torque estimation among four repetitions of the bowing task performed by a subject with (a) the MAP algorithm and (b) the OpenSim ID toolbox. The analysis has been done for the case with the weight  $W$  (CASE A) and the case without  $W$  (CASE B).



## Chapter 6

# Towards the Real-Time Human Dynamics Estimation

*The Scientist must set in order. Science is built up with facts, as a house is with stones. But a collection of facts is no more a science than a heap of stones is a house.*

Henri Poincaré

In this Chapter, a first attempt to aim at advancing the current state of the art in pHRI is presented through the design of an estimation tool for monitoring the dynamics of the human in a real-time domain. From a theoretical point of view, the online design does not differ from the version implemented in the previous chapter. However the logic in which input data have to be acquired and the way in which they have to be processed are completely different in the real-time context. Here the idea is to exploit a middleware already developed for the robot iCub to perform the online human dynamics estimation. To this scope the software implementation in Figure 5.1 was revisited and modified accordingly.

All the software related to this Chapter has been released as an open source-code and it is hosted on GitHub in the Robotology organization [HDE, 2017].

### 6.1 YARP Middleware for the Human Framework

YARP (Yet Another Robot Platform) is a middleware developed at Istituto Italiano di Tecnologia [Metta et al., 2006]. It is a C++ platform embedding libraries, protocols and tools, written for interfacing humanoid robots. YARP is mainly used to

minimize the effort in the infrastructure-level software development by facilitating the code reusability and modularity.

YARP allows to split the algorithm for the estimation of the human dynamics into different modules by ensuring *i*) communication and *ii*) connection between them but preserving, in the meanwhile, their independence [Romano et al., 2017]. The algorithm, represented in Figure 5.1 for offline evaluations, is hereafter structured into modules (in Figure 6.1) in order to fit the online requirements.

### The *human-state-provider* Module

As suggested by the name, the module has to provide in real-time the human state  $(\mathbf{q}, \dot{\mathbf{q}})$ . A pre-built URDF model of the human and the Xsens motion capture data (coming here from a YARP driver) are the inputs of the module. The information coming from the motion capture system has to be converted in a representation compatible with our human dynamic model represented in Equation (4.22), as follows.

Let  $i$  and  $k$  be two links coupled by a joint. If  ${}^{\mathcal{I}}\mathbf{T}_i, {}^{\mathcal{I}}\mathbf{T}_k \in SE(3)$  are the pose of the links w.r.t. a generic inertial frame  $\mathcal{I}$  in the original human model (i.e., the Xsens model) and  ${}^{\mathcal{I}}\widehat{\mathbf{T}}_i(\mathbf{q}), {}^{\mathcal{I}}\widehat{\mathbf{T}}_k(\mathbf{q}) \in SE(3)$  the pose of the same quantities in our dynamic model, we can use IK to map the links pose to the configuration  $\mathbf{q}$ . The relative pose is  ${}^i\mathbf{T}_k = {}^i\mathbf{T}_{\mathcal{I}} {}^{\mathcal{I}}\mathbf{T}_k$  for the original model,  ${}^i\widehat{\mathbf{T}}_k(\mathbf{q}) = {}^i\widehat{\mathbf{T}}_{\mathcal{I}}(\mathbf{q}) {}^{\mathcal{I}}\widehat{\mathbf{T}}_k(\mathbf{q})$  for our model. The module solves a nonlinear optimization problem, such as

$$\min_{\mathbf{q}} \text{error}({}^i\mathbf{T}_k, {}^i\widehat{\mathbf{T}}_k(\mathbf{q})), \quad \mathbf{q}_{min} \leq \mathbf{q} \leq \mathbf{q}_{max}. \quad (6.1)$$

The solution of the problem (6.1) is that value of  $\mathbf{q}$  that minimizes the error function  $\text{error} : SE(3) \rightarrow \mathbb{R}$  in the joint limits range  $[\mathbf{q}_{min}, \mathbf{q}_{max}]$ .

To compute the velocity  $\dot{\mathbf{q}}$ , the module reads from the Xsens the angular velocities  $\boldsymbol{\omega}_i, \boldsymbol{\omega}_k$  and computes the relative angular velocity of the two links  ${}^i\boldsymbol{\omega}_k$ . Our model velocity is then computed by inverting the following relation:

$${}^i\widehat{\boldsymbol{\omega}}_k = {}^i\mathbf{J}_k(\mathbf{q})\dot{\mathbf{q}}, \quad (6.2)$$

where  ${}^i\mathbf{J}_k$  is the relative Jacobian of the link  $k$  w.r.t. the link  $i$  and  ${}^i\widehat{\boldsymbol{\omega}}_k$  is the angular velocity of the link  $k$  w.r.t. the link  $i$  of our dynamic model. Since in general  ${}^i\widehat{\boldsymbol{\omega}}_k \neq {}^i\boldsymbol{\omega}_k$ , Equation (6.2) is solved in the least-squares sense, such that

$$\dot{\mathbf{q}}^* = \arg \min_{\dot{\mathbf{q}}} \|{}^i\widehat{\boldsymbol{\omega}}_k - {}^i\mathbf{J}_k(\mathbf{q})\dot{\mathbf{q}}\|^2. \quad (6.3)$$

For each pair of coupled links  $(i, k)$ , the *human-state-provider* is in charge of computing the mapping procedure  $({}^i\mathbf{T}_k, {}^i\boldsymbol{\omega}_k) \rightarrow (\mathbf{q}, \dot{\mathbf{q}}^*)$ . This formulation is quite generic and allows to handle models of different complexity.

### **The *human-forces-provider* Module**

The module is composed of two interfaces. The first interface is in charge of reading forces coming from different YARP-based devices (force plates or ftShoes) and from YARP ports (the iCub, in case of pHRI). The second interface transforms force readings into 6D force vectors expressed in human reference frames, as required from the vector of measurements  $\mathbf{y}$ . The proper force transformation requires that the pose of the human w.r.t. the force plates and the robot is a known quantity.

### **The *human-dynamics-estimator* Module**

The module provides the final estimation for the vector  $\mathbf{d}$  given as inputs the previous two modules output data. In order to properly cluster data into  $\mathbf{y}$  vector, it needs the human state and the forces readings both expressed in human frames. Then, together with the human state  $(\mathbf{q}, \dot{\mathbf{q}})$  and some information extracted from the URDF model, the module launches the MAP algorithm with the Cholesky factorization.

YARP allows to visualize the real-time human dynamics estimation (whether a pHRI is occurring or not) by means of some structured modules and a ROS-based visualizer (gray part in the Figure 6.1). The *human-viz* module is composed of different YARP submodules that are in charge of reading information from the Xsens system, the human state  $(\mathbf{q}, \dot{\mathbf{q}})$ , the estimated vector  $\mathbf{d}$ , and of publishing information to be sent to the visualization tool in the form of ROS-topic messages. ROS messages (including those coming from the *human-forces-provider* module) are visualized in the toolkit RViz [Kam et al., 2015]. The advantage in adopting this tool is due to its versatility and agnosticism to the type of the data structure or algorithm.

At this preliminary stage, we observed that 100 Hz is a sufficient frequency for the outputs of the *human-forces-provider* and the *human-dynamics-estimator* modules; 20 Hz for obtaining a suitable output of the *human-state-provider* module. The last frequency is strongly dependent on the type of optimization solver used in computing the IK.

## **6.2 Towards the Online Estimation**

A preliminary investigation on the online algorithm estimation has been done. Similarly to the experimental setup in Figure 5.19, a subject was asked to wear the suit and the ftShoes and to interact with the iCub through a pushing bowing. The estimation vector  $\mathbf{d}$  was here online computed by the YARP infrastructure in Figure 6.1. Figure 6.2a shows very preliminary results of three consecutive pHRI bow-

ings. It shows the comparison between the external forces transformed in human frames by the *human-forces-provider* module (in red) and the same forces as estimated in  $\mathbf{d}$  by the *human-dynamics-estimator* module (in blue). The same analysis has been done for four repetitions of pHRI squat task, Figure 6.2b. It is important remarking that these preliminary results are relying only on the forces measurements (i.e., no IMUs or joint accelerations  $\ddot{\mathbf{q}}$  on vector  $\mathbf{y}$ ). Although they are very promising, further investigations are required in the very next future.

In addition to providing a visual feedback to the estimation, the visualizer gives us an important information about how much the human joint effort is. The joint torques (estimated via MAP) are represented with spheres whose colour is an indicator of the ‘effort’: in a gray scale, a light sphere means a high effort, a dark sphere a minor effort. Figure 6.3 shows three different pHRI tasks with their real-time visualizations, for a bowing, a squat task, a task in which the human is helping the robot to stand up from a rigid support, respectively. At the current stage, any kind of pHRI can be visualized in the real-time framework as long as it obeys the initial assumptions, (i.e., fixed base and rigid contact conditions).

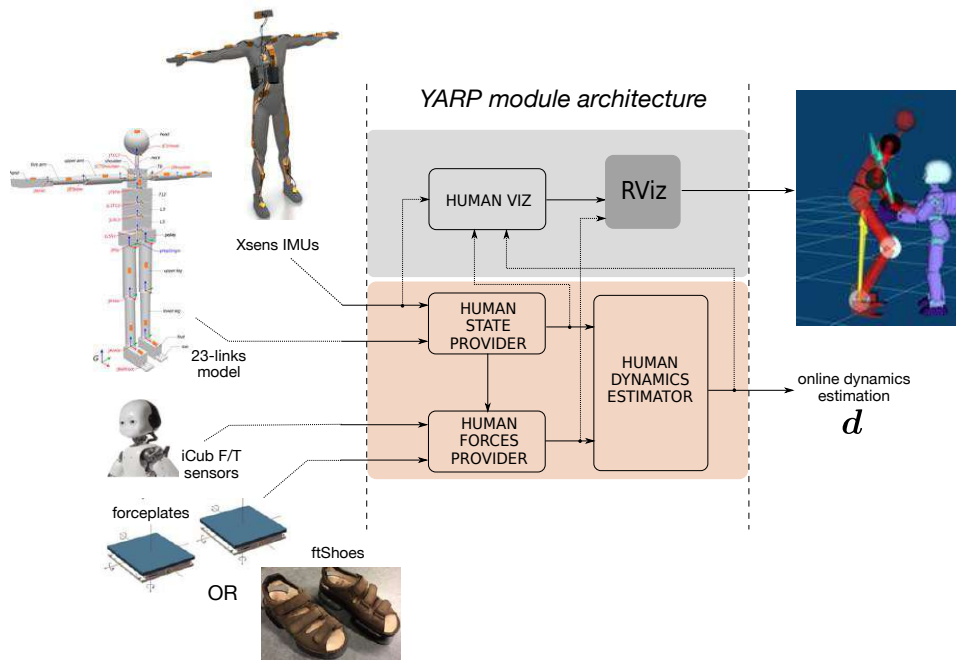
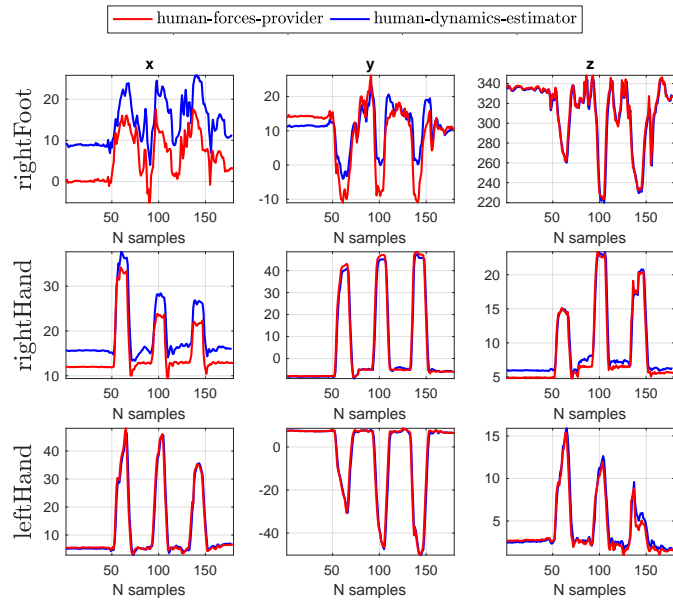
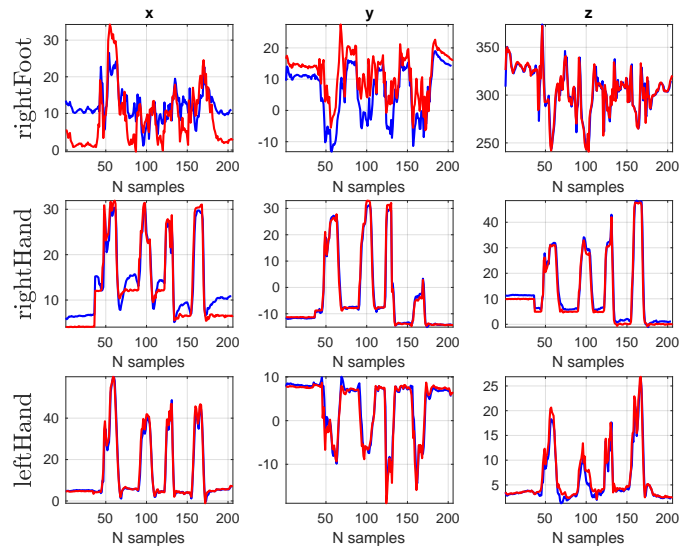


Fig. 6.1 The YARP architecture for estimating and visualizing real-domain human dynamics estimation. The software architecture is able to estimate the dynamic variables  $\mathbf{d}$  for each link/joint in the model (pink area) and to visualize the information about the kinematics and the dynamics of the human via RViz (gray area)



(a) pHRI bowing



(b) pHRI squat

Fig. 6.2 Comparison between external forces [N] transformed in human frames by the *human-forces-provider* module (in red) and the same quantities as estimated from the *human-dynamics-estimator* module (in blue), for the pHRI (a) bowing and (b) squat tasks.

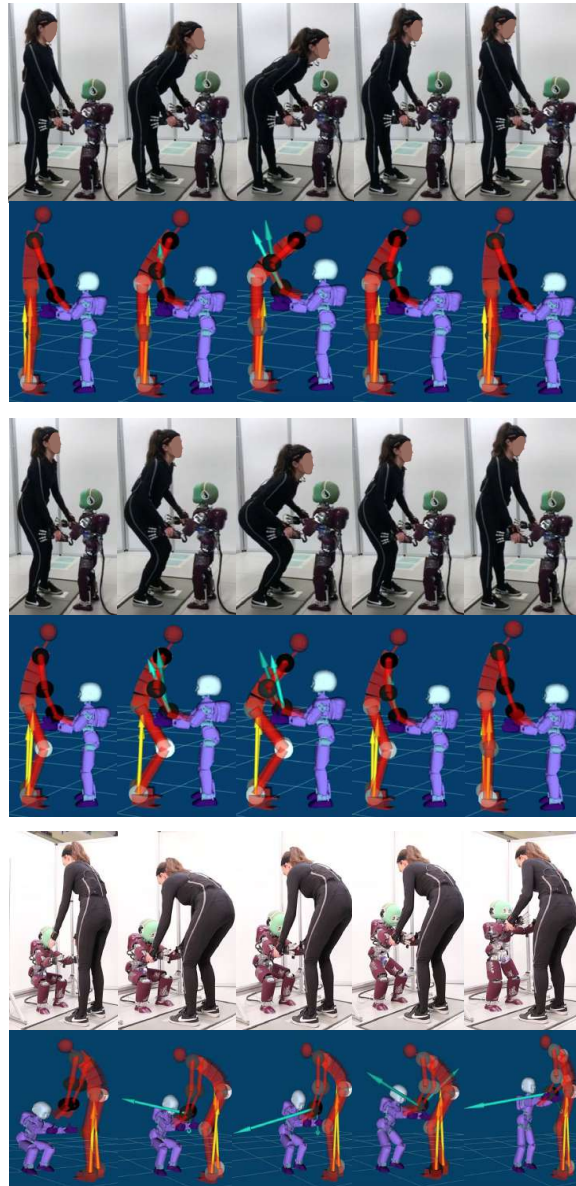


Fig. 6.3 Subject performing three different tasks with the related real-time RViz visualization: a bowing (*on top*), a squat (*on middle*), a task where the human is helping the iCub to stand up from a rigid support (*on bottom*). The visualizer shows the forces expressed in human frames: the ground reaction forces (in yellow) and the forces measured by the F/T sensors of the robot at the human hands (in light blue). It visualizes also how much 'effort' (in terms of joint torques) the human is doing during the pHRI by means of gray-scale spheres placed at the joints: a light sphere means a high effort, a dark sphere a minor effort.

## Chapter 7

# The *human-in-the-loop* Concept

*Without haste, but without rest.*

Wolfgang von Goethe

This Chapter discusses the possibility to extend the human dynamics estimation framework to a new framework that encompasses an *active* collaboration with a robot. The *human-in-the-loop* concept implies that the human agent is collaborating with a torque-controlled robot that is able to exploit the human collaboration (in term of human dynamics) to achieve its control objective. The dyadic interaction yields to a bidirectional contribute:

- i*) from the human side, it is mandatory to exploit the contact forces measured during the interaction through the robot for computing the human dynamics;
- ii*) from the robot side, it is mandatory to exploit the information coming from the human dynamics in order to synthesize a new control objective for taking advantage from the human help.

The partner-aware robot control is out of the scope of this thesis since it still has to be developed in the very next future. However, the Chapter introduces the theoretical background on which the control theory will lay its foundations.

Within this context, the framework has to be applied to a new coupled system composed by the human and the robot. The two agents maintain their own modelling (possibly in a comparable formalism) but new assumptions on the holonomic constraints have to be properly done.

## 7.1 Coupled System Modelling

Consider an interaction scenario with two agents: the human and the robot (see a generic scenario in Figure 7.1). Consider also to express the two systems with the formalism adopted for humanoid robots. The advantage of this choice is straightforward since it allows to handle both the systems with the same mathematical tool. In this domain, the application of the floating-base formalism in Section (2.5.2) leads to two sets of motion equations for the two systems, such that

$$\mathbf{M}(\mathbf{q})\dot{\boldsymbol{\nu}} + \mathbf{C}(\mathbf{q}, \boldsymbol{\nu})\boldsymbol{\nu} + \mathbf{G}(\mathbf{q}) = \begin{bmatrix} \mathbf{0} \\ \boldsymbol{\tau} \end{bmatrix} + \mathbf{J}^\top(\mathbf{q})\mathbf{f}, \quad (7.1a)$$

$$\mathbb{M}(\bar{\mathbf{q}})\dot{\bar{\boldsymbol{\nu}}} + \mathbb{C}(\bar{\mathbf{q}}, \bar{\boldsymbol{\nu}})\bar{\boldsymbol{\nu}} + \mathbb{G}(\bar{\mathbf{q}}) = \begin{bmatrix} \mathbf{0} \\ \bar{\boldsymbol{\tau}} \end{bmatrix} + \mathbb{J}^\top(\bar{\mathbf{q}})\bar{\mathbf{f}}, \quad (7.1b)$$

where the physical meaning of each term is defined in Table 7.1.

Assume that the human is subject to  $k_h$  external forces  $\mathbf{f} \in \mathbb{R}^{6k_h}$ . These forces are composed of two subsets: the forces  $\mathbf{f}^e \in \mathbb{R}^{6k_h^e}$  applied to the system by the *environment*  $e$  (e.g., from the ground), and the forces  $\mathbf{f}^d \in \mathbb{R}^{6k_h^d}$  due to the *dyadic*  $d$  interaction with the other agent, such that

$$\mathbf{f} = \left[ \mathbf{f}_1^e \quad \mathbf{f}_2^e \quad \dots \quad \mathbf{f}_{k_h^e}^e \quad \mathbf{f}_1^d \quad \mathbf{f}_2^d \quad \dots \quad \mathbf{f}_{k_h^d}^d \right]^\top \in \mathbb{R}^{6k_h}. \quad (7.2)$$

Similarly for the robot agent, there are two types of forces  $\bar{\mathbf{f}}^e \in \mathbb{R}^{6k_r^e}$  and  $\bar{\mathbf{f}}^d \in \mathbb{R}^{6k_r^d}$ , thus

$$\bar{\mathbf{f}} = \left[ \bar{\mathbf{f}}_1^e \quad \bar{\mathbf{f}}_2^e \quad \dots \quad \bar{\mathbf{f}}_{k_r^e}^e \quad \bar{\mathbf{f}}_1^d \quad \bar{\mathbf{f}}_2^d \quad \dots \quad \bar{\mathbf{f}}_{k_r^d}^d \right]^\top \in \mathbb{R}^{6k_r}. \quad (7.3)$$

Since the two systems are interacting with the environment independently from each other and from the mutual interaction, there is not any relation between the forces that the environment applies to each system (namely,  $\mathbf{f}^e$  and  $\bar{\mathbf{f}}^e$ ). Conversely, when the contact occurs, the interaction implies a holonomic relation between  $\mathbf{f}^d$  and  $\bar{\mathbf{f}}^d$ .

## 7.2 Rigid Constraints

Let  $\mathcal{I}$  be a generic inertial frame and define a set of frames

$$\mathcal{C} = \{c_1^e \quad c_2^e \quad \dots \quad c_{k_h^e}^e \quad c_1^d \quad c_2^d \quad \dots \quad c_{k_h^d}^d\} \quad (7.4)$$

associated to the human forces  $\mathbf{f}$  of (7.2), attached to the human links on which the forces are acting. More in detail, frames positions correspond to the point (on

Table 7.1 Physical meaning of the Equations (7.1a) and (7.1b) terms. In order to differentiate the same term for the two systems, the double – bold font is used for the robot matrices and the upper-lined notation for the robot variables.  $*k$  is the number of (6D) forces that each system is subject to from external entities (the other agent and/or the external environment).

Terms in Equations (7.1)	Human	Robot
Internal DoFs	$n_h$	$n_r$
Mass matrix	$\mathbf{M} \in \mathbb{R}^{(n_h+6) \times (n_h+6)}$	$\mathbf{M} \in \mathbb{R}^{(n_r+6) \times (n_r+6)}$
Coriolis effects matrix	$\mathbf{C} \in \mathbb{R}^{(n_h+6) \times (n_h+6)}$	$\mathbf{C} \in \mathbb{R}^{(n_r+6) \times (n_r+6)}$
Gravity bias	$\mathbf{G} \in \mathbb{R}^{n_h+6}$	$\mathbf{G} \in \mathbb{R}^{n_r+6}$
Configuration	$\mathbf{q} \in SE(3) \times \mathbb{R}^{n_h}$	$\bar{\mathbf{q}} \in SE(3) \times \mathbb{R}^{n_r}$
Velocity	$\boldsymbol{\nu} \in \mathbb{R}^{n_h+6}$	$\bar{\boldsymbol{\nu}} \in \mathbb{R}^{n_r+6}$
Torque	$\boldsymbol{\tau} \in \mathbb{R}^{n_h}$	$\bar{\boldsymbol{\tau}} \in \mathbb{R}^{n_r}$
Jacobian	$\mathbf{J}(\cdot)$	$\mathbb{J}(\cdot)$
Force*	$\mathbf{f} \in \mathbb{R}^{6k_h}$	$\bar{\mathbf{f}} \in \mathbb{R}^{6k_r}$

the link) of the force application with a z-axis pointing on the direction normal to the contact plane. If we consider a generic element  $c_k \in \mathcal{C}$  (both for  $c^e$  or  $c^d$ ), it is always possible to describe the following relation

$$\mathcal{I} \mathbf{v}_{c_k} = \mathbf{J}_{c_k}(\mathbf{q}) \boldsymbol{\nu}, \quad (7.5)$$

where the Jacobian is the map between the human floating-base velocity  $\boldsymbol{\nu}$  and the velocity of the frame  $c_k$  attached to the link w.r.t.  $\mathcal{I}$ .

Similarly for the robot, Equation (7.4) becomes

$$\bar{\mathcal{C}} = \{\bar{c}_1^e \quad \bar{c}_2^e \quad \dots \quad \bar{c}_{k_r^e}^e \quad \bar{c}_1^d \quad \bar{c}_2^d \quad \dots \quad \bar{c}_{k_r^d}^d\} \quad (7.6)$$

and if we consider the generic  $k$ -th element  $\bar{c}_k \in \bar{\mathcal{C}}$ , thus

$$\mathcal{I} \mathbf{v}_{\bar{c}_k} = \mathbb{J}_{\bar{c}_k}(\bar{\mathbf{q}}) \bar{\boldsymbol{\nu}}. \quad (7.7)$$

We can now distinguish between two types of rigid constraints occurring in a pHRI scenario, as represented in Figure 7.1.

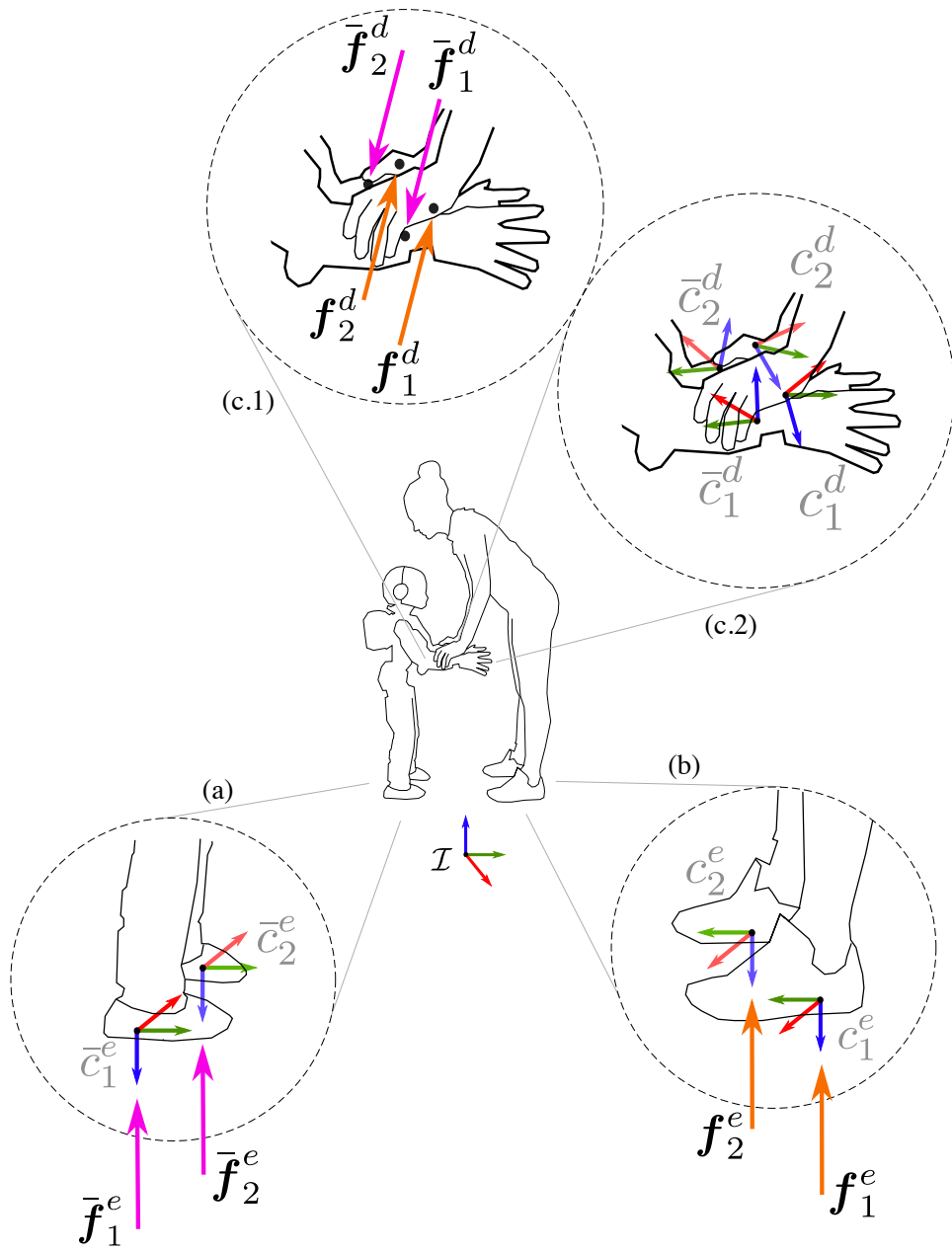


Fig. 7.1 Example of pHRI scenario: both the agents are with their feet fixed on the ground ( $k_h^e = 2, k_r^e = 2$ ) while the human is pushing down the robot arms ( $k_h^d = 2, k_r^d = 2$ ). Details (a) and (b) show the environment forces acting on the robot and the human, respectively. Both the feet are shown with their associated reference frames. Details (c.1) and (c.2) show the forces exchanged during the interaction and their frames, respectively. The frames are here represented no coincident between the human and the robot.

## 1) Environment Holonomic Constraints

If both the systems are rigidly attached to the ground during the interaction (see (a) and (b) in Figure 7.1), it can be assumed that the  $k$ -th frame in the set (7.4) associated to  $\mathbf{f}^e \in \mathbf{f}$  and the  $k$ -th frame in the set (7.6) associated to  $\bar{\mathbf{f}}^e \in \bar{\mathbf{f}}$  have a constant pose w.r.t.  $\mathcal{I}$ . For the duration of the contact, they have both zero velocity such that

$$\mathbf{0} = \mathbf{J}_{c_k^e}(\mathbf{q})\boldsymbol{\nu}, \quad (7.8a)$$

$$\mathbf{0} = \mathbb{J}_{\bar{c}_k^e}(\bar{\mathbf{q}})\bar{\boldsymbol{\nu}}. \quad (7.8b)$$

The differentiation of the Equations (7.8) yields to:

$$\mathbf{0} = \mathbf{J}_{c_k^e}(\mathbf{q})\dot{\boldsymbol{\nu}} + \dot{\mathbf{J}}_{c_k^e}(\mathbf{q})\boldsymbol{\nu}, \quad (7.9a)$$

$$\mathbf{0} = \mathbb{J}_{\bar{c}_k^e}(\bar{\mathbf{q}})\dot{\bar{\boldsymbol{\nu}}} + \dot{\mathbb{J}}_{\bar{c}_k^e}(\bar{\mathbf{q}})\bar{\boldsymbol{\nu}}, \quad (7.9b)$$

where (7.9a) represents the holonomic constraint of the human with the environment and (7.9b) the holonomic constraint of the robot with the environment.

## 2) Dyadic Interaction Holonomic Constraints

When the two systems mutually interact through a physical contact (see (c.1) and (c.2) in Figure 7.1), the relative transformation between the frames  $c_k^d \in \mathcal{C}$  and  $\bar{c}_k^d \in \bar{\mathcal{C}}$  assumes the following form:

$${}^{c_k^d}X_{\bar{c}_k^d}(\mathbf{q}, \bar{\mathbf{q}}) = {}^{c_k^d}X_{\mathcal{I}}(\mathbf{q}) {}^{\mathcal{I}}X_{\bar{c}_k^d}(\bar{\mathbf{q}}), \quad (7.10)$$

where  ${}^{c_k^d}X_{\mathcal{I}}(\mathbf{q})$  denotes the transformation from the inertial frame to the human frame  $c_k^d$  and  ${}^{\mathcal{I}}X_{\bar{c}_k^d}$  from the robot frame  $\bar{c}_k^d$  to  $\mathcal{I}$ . When  ${}^{c_k^d}X_{\bar{c}_k^d}(\mathbf{q}, \bar{\mathbf{q}})$  is constant, it means that the human and the robot are in contact. The assumption of rigid contact yields to the condition that the relative velocity between  $c_k^d$  and  $\bar{c}_k^d$  is zero and that they are moving with the same velocity w.r.t.  $\mathcal{I}$ , such as

$${}^{\mathcal{I}}\mathbf{v}_{c_k^d} = {}^{c_k^d}X_{\bar{c}_k^d}(\mathbf{q}, \bar{\mathbf{q}}) {}^{\mathcal{I}}\mathbf{v}_{\bar{c}_k^d}. \quad (7.11)$$

Consider, for the sake of simplicity, a situation in which the two frames  $c_k^d$  and  $\bar{c}_k^d$  are coincident, thus  ${}^{c_k^d}X_{\bar{c}_k^d}(\mathbf{q}, \bar{\mathbf{q}}) = \mathbf{1}_6$  and Equation (7.11) becomes

$${}^{\mathcal{I}}\mathbf{v}_{c_k^d} = {}^{\mathcal{I}}\mathbf{v}_{\bar{c}_k^d}. \quad (7.12)$$

By substituting Equations (7.5) and (7.7) in (7.12)

$$\mathbf{J}_{c_k^d}(\mathbf{q})\boldsymbol{\nu} = \mathbb{J}_{\bar{c}_k^d}(\bar{\mathbf{q}})\bar{\boldsymbol{\nu}}, \quad (7.13)$$

and differentiating Equation (7.13)

$$\mathbf{J}_{c_k^d}(\mathbf{q})\dot{\boldsymbol{\nu}} + \dot{\mathbf{J}}_{c_k^d}(\mathbf{q})\boldsymbol{\nu} = \mathbb{J}_{\bar{c}_k^d}(\bar{\mathbf{q}})\dot{\bar{\boldsymbol{\nu}}} + \dot{\mathbb{J}}_{\bar{c}_k^d}(\bar{\mathbf{q}})\bar{\boldsymbol{\nu}}, \quad (7.14)$$

$$\left[ \mathbf{J}_{c_k^d}(\mathbf{q}) \quad - \mathbb{J}_{\bar{c}_k^d}(\bar{\mathbf{q}}) \right] \begin{bmatrix} \dot{\boldsymbol{\nu}} \\ \dot{\bar{\boldsymbol{\nu}}} \end{bmatrix} + \left[ \dot{\mathbf{J}}_{c_k^d}(\mathbf{q}) \quad - \dot{\mathbb{J}}_{\bar{c}_k^d}(\bar{\mathbf{q}}) \right] \begin{bmatrix} \boldsymbol{\nu} \\ \bar{\boldsymbol{\nu}} \end{bmatrix} = \mathbf{0}. \quad (7.15)$$

In general, the pHRI scenario is fully described by the set of the following Equations:

- (7.1) for the motion description of the two systems;
- (7.9) for the holonomic constraints of both the systems with the external environment (e.g., the ground in Figure 7.1);
- (7.15) for the holonomic constraint imposed by the rigid contact interaction between the human and the robot.

A first investigation into the direction of a reactive pHRI has been done in [Romano et al., 2017]. The paper attempts to answer the question “*How can we predict human intentions so as to synthesize robot controllers that are aware of and can react to the human presence?*” by considering an interaction scenario between a human (equipped with the sensor technology described in the previous chapters) and a human-aware iCub robot. In the paper, the momentum-based balancing controller of the robot has been modified (see Section 2 of the paper) to take into account and exploit the human forces. A task for the robot stand-up from a rigid support has been performed with (as at the bottom of the Figure 6.3 ) and without the human help. Preliminary results show that the robot needs to provide less torque when helped by the human since it is capable to exploit the human assistance.

## Chapter 8

# Conclusions and Forthcoming Works

*Whatever you can do or dream you can, begin it. Boldness has genius, power and magic in it. (Begin it!)*

(misattributed to) Wolfgang von Goethe

The understanding of human dynamics and the way in which its contribution can be applied to enhance a physical human-robot interaction are two of the most promising challenges for the scientific community. The ever-growing interest in the topic, mainly aroused in the last two decades, led us to explore and shape the interaction mechanism involved during a physical interaction between humans and robotic machines.

Three years ago, the project call of my Ph.D. course stated the following sentence: [...] *this research proposal aims at developing a prototype of a force and motion capture system for humans*. By bearing in mind the final objective of the project, we really developed that prototype. This thesis describes the design of a novel framework for the simultaneous human whole-body motion tracking and dynamics estimation. However, it puts several questions that have to be tackled in the future if the human estimation will be integrated in the robot control loop to enhance the human-robot interaction.

In this conclusive Chapter, every treated topic in the thesis is recalled together with a discussion of the results and the future developments.

## 8.1 Discussion

In **Chapter 3** we apply the estimation approach to human models described as articulated multi-body systems composed of 1-DoF revolute joints, by using the classical formalism widespread in robotics [Featherstone, 2007]. In particular we combined this type of joints to obtain a series of joints with a high number of DoFs (2 or 3). As a straightforward consequence, the model is composed by 23 real and 23 fake links (see Appendix B). This results in a very big vector  $\mathbf{d}$  (i.e.,  $\mathbf{d} \in \mathbb{R}^{1248}$ ) and affects remarkably the computational time. The first intervention will deal with a solution for removing the fake links from the model.

Furthermore, real human joints barely exhibit the pure-axial motion, thus our modelling is only a rough approximation of the complexity exhibited by real-life biomechanical joints. Despite the fact that we chose this joint model for an initial exploration of the method, the proposed algorithm is not limited to this particular choice. In particular the properties of any joint (with an arbitrary number of DoFs) can be encapsulated in an interface where the relative position, velocity and acceleration of the two bodies connected by it are described by arbitrary functions of joint coordinates variables and their derivatives that can then be directly inserted in the equations of the system (4.22). In this way, any kind of joint modelling can be described under this formalism. In the future we plan to generalize the method to arbitrarily complex musculoskeletal models (see a possible inspiring implementation in [Seth et al., 2010]).

Another important investigation will concern the estimation of the human inertial parameters (mass, CoM, inertias). The use of the anthropometric tables is currently the most used tool for estimating such values. Even though the tables allow to scale the model along with the subject, this could be a rough approximation for the non-standard population samples (children, elderly, obese, individual with prostheses) and this is pushing the scientific community towards the development of new alternative ways to estimate these parameters directly from data [Venture et al., 2009], [Robert et al., 2017].

**Chapter 4** describes the human dynamics estimation problem by framing the solution in a probabilistic domain by means of a MAP estimator or equivalently a weighted least-squares. The main limitation of the current stage lies in its fixed-base formulation. Even if a mathematical formalism already exists for the floating-base representation (e.g., Equation (2.30)) the existing software tools do not support it yet. The upgrade to a floating-base model is mandatory if we want to test our algorithm in more complex experimental setups where both humans and robots could move while interacting.

**Chapter 5** presents a software implementation for the MAP algorithm specifically tailored for Matlab offline validation procedures. The Chapter shows how the algorithm is able to estimate human kinematic and dynamic variables. The estimation capability of the algorithm is validated through a comparison between those variables that can be measured and estimated at the same time. Although Section 5.3 leads to suitable estimations, the method questionability lies the over-reliance of the solution on the chosen measurement covariances. Their initial setting was manually tuned by using datasheet values (when available) and kept constant for all the setups. This may have altered the goodness of the results. The problem equally affects the real-time YARP estimation since, at the current stage, even there the measurement covariances are defined in a fixed initial configuration file. The next forthcoming work goes towards the direction of a sort of data-driven covariance estimation as it is well-known that the measurement covariances may vary when the process is at different operating conditions [Romagnoli and Sánchez, 1999]. The Expectation-Maximization (EM) algorithm is one solution for the data-driven estimation [Keller et al., 1992] [Chen et al., 1997] [Kulathinal et al., 2002]. By starting from a known initial covariance of the measurement (e.g., from the sensor datasheet), the covariance  $\Sigma_{y|d}$  (Equation (4.35a)) could be optimized until the EM does not increase the likelihood anymore.

**Chapter 6** endeavours to design a C++ based tool for monitoring the real-time dynamics of a human being physically involved in a collaborative task with a robot. This Chapter, in a sense, describes the real-time evolution of the previous offline framework and proposes a preliminary validation analysis with very promising results. The real-time context automatically yields to a different way for retrieving the human state and the joint accelerations w.r.t. the offline case. Currently, a straightforward way for computing  $\mathbf{q}$  and  $\dot{\mathbf{q}}$  from data has been already implemented in Section 6.1. However, we are still investigating on the real-time way for obtaining  $\ddot{\mathbf{q}}$ . Some solutions are suggested in [van den Bogert et al., 2013] and in the GitHub repository [RTbiomechanics].

For the time being, all the analysis performed in Chapters 5 and 6 completely disregard –at each computation step  $t$ – the contribution of the computation at the previous step  $t-1$ . Thus, the previous state does not influence every new computation at all. This is due to the fact that  $\mathbf{q}$  and  $\dot{\mathbf{q}}$  are known and without uncertainty. This assumption is definitively too restrictive since we typically have access to a limited set of these variables through noisy measurements. It is well-known that in practical acquisitions, the state is affected by statistical noise and other inaccuracies. The Kalman filtering analysis will allow us to obtain a more accurate estimation than those based on a single measurement alone (i.e., the current case). This research is therefore moving towards an extended Kalman filtering (EKF)

analysis [Lefebvre et al., 2004]. The EKF is a common used tool for improving the estimation performances of nonlinear problems (e.g., [Lin and Kulić, 2012]) and many variants have been developed starting from it (e.g., [Joukov et al., 2017]). However, in order to apply the Kalman theory to our estimation problem, several modifications on the formalism in the system (4.22) are required. The first step is to include the estimation of the state  $\boldsymbol{x} = (\boldsymbol{q}, \dot{\boldsymbol{q}})$  that currently is missing in the problem. This is not a trivial task and complications arise from the fact that the system (4.22) is not linear in  $\boldsymbol{x}$ . Appendix D recalls the mathematical computations necessary to modify the MAP problem for a simultaneous human dynamics and state estimation. This will be the very first step in order to fit the EKF requirements.

The long-term objective is represented by **Chapter 7** where the possibility to extend the human dynamics estimation framework to a new framework that encompasses an *active* collaboration with a robot is discussed. It is worth remarking that, at the current stage, the robot is considered as a *passive* forces measurer. In the experimental setups of Figures 5.19 and 6.3, the robot is considered only as a tool for estimating the external forces acting on the human hands.

However, since the human dynamics is of pivotal importance for a control design aimed at considering the *human in the loop*, the forthcoming idea will be to provide (online) the robot with the human force feedback. This information could be used as a tool for *reactive* human-robot collaboration (implying a robot reactive control) and, in a long-term perspective, for *predictive* collaboration and enhancing remarkably the interaction naturalness. Thus, in the near future a new robot controller has to be designed in order that the robot can adapt and adjust the interaction strategy accordingly. This is also the first milestone of the H2020 An.Dy project that represents the technology outcome of this work and aims at advancing the current state of the art in the pHRI field.





## Appendix A

# Top-Down and Bottom-Up Approaches

Consider a generic 2-DoF model (Figure A.1). The model is represented as a kinematic tree with  $N_B = 2$  moving links numbering from 1 to  $N_B$ . Assume that the model is standing on a force plate (FP), in rigid contact with link 0 (i.e., the fixed base), that provides a measurement of the force that the model is exchanging with the ground. No external forces are acting on links 1 and 2. Let  $\underline{g} = [0 \ 0 \ -9.81 \ 0 \ 0 \ 0]^T$  be the gravitational spatial acceleration vector expressed in the body frame 0.

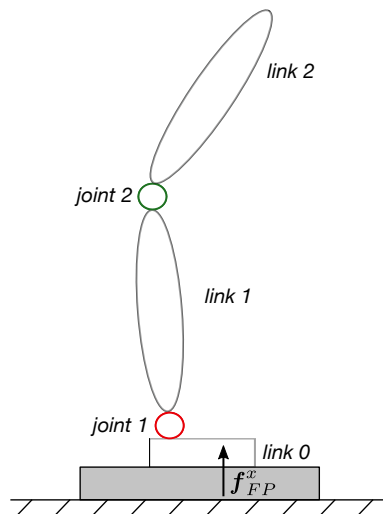


Fig. A.1 Representation of a 2-DoF fixed-base model standing on a force plate (in grey).

The kinematics of the system is described by the following equations:

$$\underline{v}_0 = \mathbf{0} \quad (\text{A.1})$$

$$\underline{a}_0 = -\underline{g} \quad (\text{A.2})$$

$$\underline{v}_1 = {}^1\mathbf{X}_0\underline{v}_0 + \bar{\mathbf{S}}_1\dot{q}_1 \quad (\text{A.3})$$

$$\underline{v}_{J1} = \bar{\mathbf{S}}_1\dot{q}_1 \quad (\text{A.4})$$

$$\underline{a}_1 = {}^1\mathbf{X}_0\underline{a}_0 + \bar{\mathbf{S}}_1\ddot{q}_1 + \underline{v}_1 \times \underline{v}_{J1} \quad (\text{A.5})$$

$$\underline{v}_2 = {}^2\mathbf{X}_1\underline{v}_1 + \bar{\mathbf{S}}_2\dot{q}_2 \quad (\text{A.6})$$

$$\underline{v}_{J2} = \bar{\mathbf{S}}_2\dot{q}_2 \quad (\text{A.7})$$

$$\underline{a}_2 = {}^2\mathbf{X}_1\underline{a}_1 + \bar{\mathbf{S}}_2\ddot{q}_2 + \underline{v}_2 \times \underline{v}_{J2} \quad (\text{A.8})$$

The common mathematical approach to compute the dynamics addresses to recursively solving the Newton-Euler equations for each link of the body. The recursive algorithm yields to different results depending on the choice of the starting point of the propagation. If the algorithm starts from link 0 going upward to link 2, the recursion is called *bottom-up*. Reversely, from link 2 to link 0, it is a *top-down* recursion. Examine, in the our model specific case, what is the difference of the two approaches.

### Top-Down

$$\underline{f}_2^B = \mathbf{I}_2\underline{a}_2 + \underline{v}_2 \times^* \mathbf{I}_2\underline{v}_2 \quad (\text{A.9})$$

$$\underline{f}_2 = \underline{f}_2^B - \underline{f}_2^x = \underline{f}_2^B \quad (\text{A.10})$$

$$\underline{f}_1^B = \mathbf{I}_1\underline{a}_1 + \underline{v}_1 \times^* \mathbf{I}_1\underline{v}_1 \quad (\text{A.11})$$

$$\underline{f}_1 = \underline{f}_1^B - \underline{f}_1^x + {}^1\mathbf{X}_2^*\underline{f}_2 = \underline{f}_1^B + {}^1\mathbf{X}_2^*\underline{f}_2 \quad (\text{A.12})$$

$$\underline{f}_0^B = \mathbf{I}_0\underline{a}_0 + \underline{v}_0 \times^* \mathbf{I}_0\underline{v}_0 = \mathbf{I}_0\underline{a}_0 \quad (\text{A.13})$$

$$\underline{f}_0 = \underline{f}_0^B - \underline{f}_0^x + {}^0\mathbf{X}_1^*\underline{f}_1 \quad (\text{A.14})$$

Since  $\underline{f}_0 = \mathbf{0}$  and  $\underline{f}_0^x = {}^0\mathbf{X}_{FP}^*\underline{f}_{FP}$ , thus

$$\mathbf{0} = \mathbf{I}_0\underline{a}_0 - {}^0\mathbf{X}_{FP}^*\underline{f}_{FP} + {}^0\mathbf{X}_1^*\underline{f}_1 \quad (\text{A.15})$$

$$\Rightarrow {}^0\mathbf{X}_1^*\underline{f}_1 = \mathbf{I}_0\underline{g} + {}^0\mathbf{X}_{FP}^*\underline{f}_{FP} \quad (\text{A.16})$$

$$\Rightarrow \underline{f}_1 = {}^1\mathbf{X}_0^*(\mathbf{I}_0\underline{g} + {}^0\mathbf{X}_{FP}^*\underline{f}_{FP}) \quad (\text{A.17})$$

The overdeterminacy of the system yields to a physical inconsistency:  $\underline{f}_1$  is defined from both Equations (A.12) and (A.17).

### Bottom-Up

$$\underline{f}_0 = \underline{f}_0^B - \underline{f}_0^x + {}^0\mathbf{X}_1^* \underline{f}_1 \quad (\text{A.18})$$

$$\Rightarrow \underline{f}_1 = {}^1\mathbf{X}_0^* (\mathbf{I}_0 \underline{g} + {}^0\mathbf{X}_{FP}^* \underline{f}_{FP}) \quad (\text{A.19})$$

$$\underline{f}_1 = \underline{f}_1^B + {}^1\mathbf{X}_2^* \underline{f}_2 \quad (\text{A.20})$$

$$\Rightarrow {}^1\mathbf{X}_2^* \underline{f}_2 = \underline{f}_1 - \underline{f}_1^B \quad (\text{A.21})$$

$$\Rightarrow \underline{f}_2 = {}^2\mathbf{X}_1^* (\underline{f}_1 - \underline{f}_1^B) \quad (\text{A.22})$$

$$\underline{f}_2 = \underline{f}_2^B - \underline{f}_2^x = \underline{f}_2^B \quad (\text{A.23})$$

Again, as in the top-down approach, there is a physical inconsistency for the force  $\underline{f}_2$  that is represented by both (A.22) and (A.23).

### Solution Criterion

When an additional measurement (e.g.,  $\underline{f}_{FP}$ ) is added into the computation, the system becomes overdetermined. It is evident at the top-most segment (in the case of bottom-up) or at the bottom-most segment (in the case of top-down) where the physics condition are not satisfied anymore. The solution is obtained by discarding one set of 6 equations (e.g., (A.12) or (A.17) for the top-down, (A.22) or (A.23) for the bottom-up) by strongly conditioning the final result of the computation. An important drawback of this criterion is that all the other variables (both forces and kinematic data) that entered in the discarded set of equations will remain unused in the computation.



## Appendix B

# URDF Human Modelling

The URDF is an XML specification describing the kinematic and dynamic properties of a robot in ROS. It is composed of `link` and `joint` elements. For the `link` several attributes are specified: the name, the inertial properties (mass, CoM origin, inertias), the visual properties (boxes origin and geometry). Hereafter an example for the `RightLowerLeg` element.

```
1 <linkName ="RightLowerLeg">
2   <inertial>
3     <massValue ="RIGHTLOWERLEGMASS"/>
4     <!--COM origin w.r.t. jRightKnee-->
5     <originxyz ="RIGHTLOWERLEG_COM_ORIGIN" rpy ="0 0 0" />
6     <inertia ixx="RIGHTLOWERLEGINERTIAIXX" iyy="
7       RIGHTLOWERLEGINERTIAIYY"
8       izz="RIGHTLOWERLEGINERTIAIZZ" ixy="0" ixz="0" iyz="0"/>
9   </inertial>
10  <visual>
11    <!--box origin w.r.t. jRightKnee-->
12    <origin xyz="RIGHTLOWERLEG_BOX_ORIGIN" rpy="0 0 0" />
13    <geometry>
14      <cylinder length="RIGHTLOWERLEGHEIGHT"
15        radius="RIGHTLOWERLEGRADIUS"/>
16    </geometry>
17  </visual>
18 </link>
```

For the `joint` attributes : the name and the type, the origin, the parent and child link, the axis along which the motion is allowed. Since the URDF does not support spherical joint design, we combine joints of revolute type to obtain a series of joints with a high number of DoFs. The limitation on the `joint` automatically

implied an important modification of the entire structure in the tree. Since the URDF supports only a structure where each link is connected with 1-DoF joint (a condition of two consecutive joints is not supported), thus it had to be necessary the creation of a ‘dummy’ link. Here follow the XML tag for the creation of the dummy link for the RightLowerLeg (see also Figure B.1).

```

1 <link name="RightLowerLeg_f1">
2   <inertial>
3     <mass value="DUMMYMASS"/>
4     <origin xyz="0 0 0" rpy="0 0 0" />
5     <inertia ixx="DUMMYININERTIA" iyy="DUMMYININERTIA"
6       izz="DUMMYININERTIA" ixy="0" ixz="0" iyz="0"/>
7   </inertial>
8 </link>

```

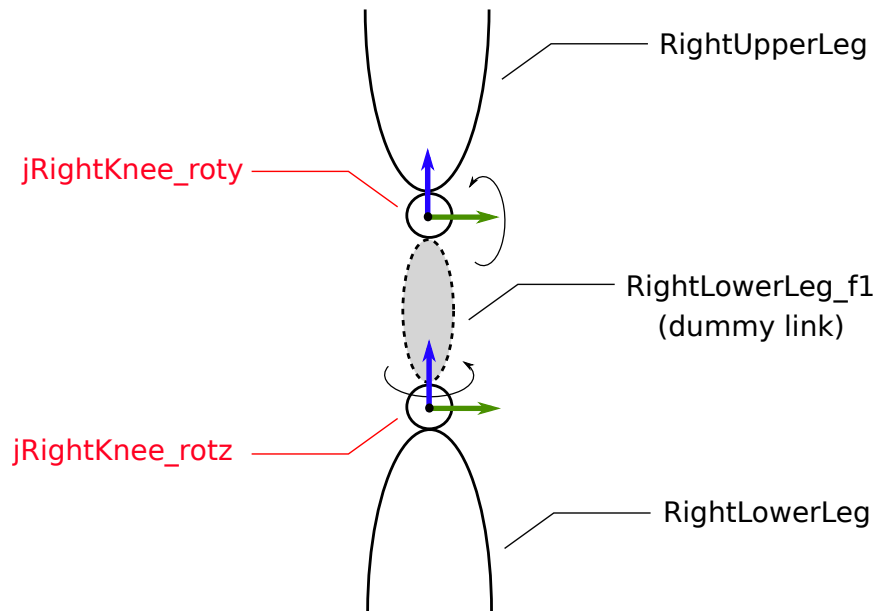


Fig. B.1 The dummy link connects the 1-DoF joint jRightKnee (rotation along  $y$ ) and the 1-DoF joint jRightKnee (rotation along  $z$ ), in order to make possible the creation of a 2-DoF joint.

Hereafter, it is showed the XML tag for defining joint elements. In the specific case of the right knee, it is specified the lower joint limit ( $0^\circ$  for the flexion along  $y$ ,  $-40^\circ$  for the lateral rotation along  $z$ ) and the upper joint limit ( $135^\circ$  for the flexion along  $y$ ,  $30^\circ$  for the lateral rotation along  $z$ ). Note that the limit effort and velocity are safety attributes specific for controllers settings. Their values are not used in the case of human models.

```

1 <joint name="jRightKnee_roty" type="revolute">
2   <origin xyz="jRightKnee_ORIGIN" rpy="0 0 0"/>
3   <parent link="RightUpperLeg"/>
4   <child link="RightLowerLeg_f1"/>
5   <dynamics damping="0.0" friction="0.0"/>
6   <limit effort="30" velocity="1.0" lower="0" upper="2.35619"/>
7   <axis xyz="0 1 0"/>
8 </joint>
9 <joint name="jRightKnee_rotz" type="revolute">
10  <origin xyz="0 0 0" rpy="0 0 0"/>
11  <parent link="RightLowerLeg_f1"/>
12  <child link="RightLowerLeg"/>
13  <dynamics damping="0.0" friction="0.0"/>
14  <limit effort="30" velocity="1.0" lower="-0.698132" upper="
15    0.523599"/>
16  <axis xyz="0 0 1"/>
17 </joint>

```

The final URDF file is a XML list of link and joint elements entirely describing the model. Hereafter are listed, in two different XML windows, all the links and the joints of the 48-DoF URDF template.

```

1 <!--URDF MODEL 48 DoFs-->
2 <robot name="XSensStyleModel_template">
3 <!--LINKS-->
4   <!--Link base (1)-->
5   <link name="Pelvis">
6   <!--Chain from (2) to (7)-->
7   <link name="L5_f1">
8   <link name="L5">
9   <link name="L3_f1">
10  <link name="L3">
11  <link name="T12_f1">
12  <link name="T12">
13  <link name="T8_f1">
14  <link name="T8_f2">
15  <link name="T8">
16  <link name="Neck_f1">
17  <link name="Neck_f2">

```

```

18 <link name="Neck">
19 <link name="Head_f1">
20 <link name="Head">
21 <!--Chain from (8) to (11)-->
22 <link name="RightShoulder">
23 <link name="RightUpperArm_f1">
24 <link name="RightUpperArm_f2">
25 <link name="RightUpperArm">
26 <link name="RightForeArm_f1">
27 <link name="RightForeArm">
28 <link name="RightHand_f1">
29 <link name="RightHand">
30 <!--Chain from (12) to (15)-->
31 <link name="LeftShoulder">
32 <link name="LeftUpperArm_f1">
33 <link name="LeftUpperArm_f2">
34 <link name="LeftUpperArm">
35 <link name="LeftForeArm_f1">
36 <link name="LeftForeArm">
37 <link name="LeftHand_f1">
38 <link name="LeftHand">
39 <!--Chain from (16) to (19)-->
40 <link name="RightUpperLeg_f1">
41 <link name="RightUpperLeg_f2">
42 <link name="RightUpperLeg">
43 <link name="RightLowerLeg_f1">
44 <link name="RightLowerLeg">
45 <link name="RightFoot_f1">
46 <link name="RightFoot_f2">
47 <link name="RightFoot">
48 <link name="RightToe">
49 <!--Chain from (20) to (23)-->
50 <link name="LeftUpperLeg_f1">
51 <link name="LeftUpperLeg_f2">
52 <link name="LeftUpperLeg">
53 <link name="LeftLowerLeg_f1">
54 <link name="LeftLowerLeg">
55 <link name="LeftFoot_f1">
56 <link name="LeftFoot_f2">
57 <link name="LeftFoot">
58 <link name="LeftToe">
59 <!--JOINTS-->
60 <!--Chain from (2) to (7)-->
61 <joint name="jL5S1_rotx" type="revolute">
62 <joint name="jL5S1_roty" type="revolute">
63 <joint name="jL4L3_rotx" type="revolute">
64 <joint name="jL4L3_roty" type="revolute">
65 <joint name="jL1T12_rotx" type="revolute">
66 <joint name="jL1T12_roty" type="revolute">

```

```

67 <joint name="jT9T8_rotx" type="revolute">
68 <joint name="jT9T8_roty" type="revolute">
69 <joint name="jT9T8_rotz" type="revolute">
70 <joint name="jT1C7_rotx" type="revolute">
71 <joint name="jT1C7_roty" type="revolute">
72 <joint name="jT1C7_rotz" type="revolute">
73 <joint name="jC1Head_rotx" type="revolute">
74 <joint name="jC1Head_roty" type="revolute">
75 <!--Chain from (8) to (11)-->
76 <joint name="jRightC7Shoulder_rotx" type="revolute">
77 <joint name="jRightShoulder_rotx" type="revolute">
78 <joint name="jRightShoulder_roty" type="revolute">
79 <joint name="jRightShoulder_rotz" type="revolute">
80 <joint name="jRightElbow_roty" type="revolute">
81 <joint name="jRightElbow_rotz" type="revolute">
82 <joint name="jRightWrist_rotx" type="revolute">
83 <joint name="jRightWrist_rotz" type="revolute">
84 <!--Chain from (12) to (15)-->
85 <joint name="jLeftC7Shoulder_rotx" type="revolute">
86 <joint name="jLeftShoulder_rotx" type="revolute">
87 <joint name="jLeftShoulder_roty" type="revolute">
88 <joint name="jLeftShoulder_rotz" type="revolute">
89 <joint name="jLeftElbow_roty" type="revolute">
90 <joint name="jLeftElbow_rotz" type="revolute">
91 <joint name="jLeftWrist_rotx" type="revolute">
92 <joint name="jLeftWrist_rotz" type="revolute">
93 <!--Chain from (16) to (19)-->
94 <joint name="jRightHip_rotx" type="revolute">
95 <joint name="jRightHip_roty" type="revolute">
96 <joint name="jRightHip_rotz" type="revolute">
97 <joint name="jRightKnee_roty" type="revolute">
98 <joint name="jRightKnee_rotz" type="revolute">
99 <joint name="jRightAnkle_rotx" type="revolute">
100 <joint name="jRightAnkle_roty" type="revolute">
101 <joint name="jRightAnkle_rotz" type="revolute">
102 <joint name="jRightBallFoot_roty" type="revolute">
103 <!--Chain from (20) to (23)-->
104 <joint name="jLeftHip_rotx" type="revolute">
105 <joint name="jLeftHip_roty" type="revolute">
106 <joint name="jLeftHip_rotz" type="revolute">
107 <joint name="jLeftKnee_roty" type="revolute">
108 <joint name="jLeftKnee_rotz" type="revolute">
109 <joint name="jLeftAnkle_rotx" type="revolute">
110 <joint name="jLeftAnkle_roty" type="revolute">
111 <joint name="jLeftAnkle_rotz" type="revolute">
112 <joint name="jLeftBallFoot_roty" type="revolute">

```

The Gazebo simulator is used to visualize the model in Figure B.2. The Graphviz (ROS) visualizer represents the URDF model hierarchy (Figure B.3).

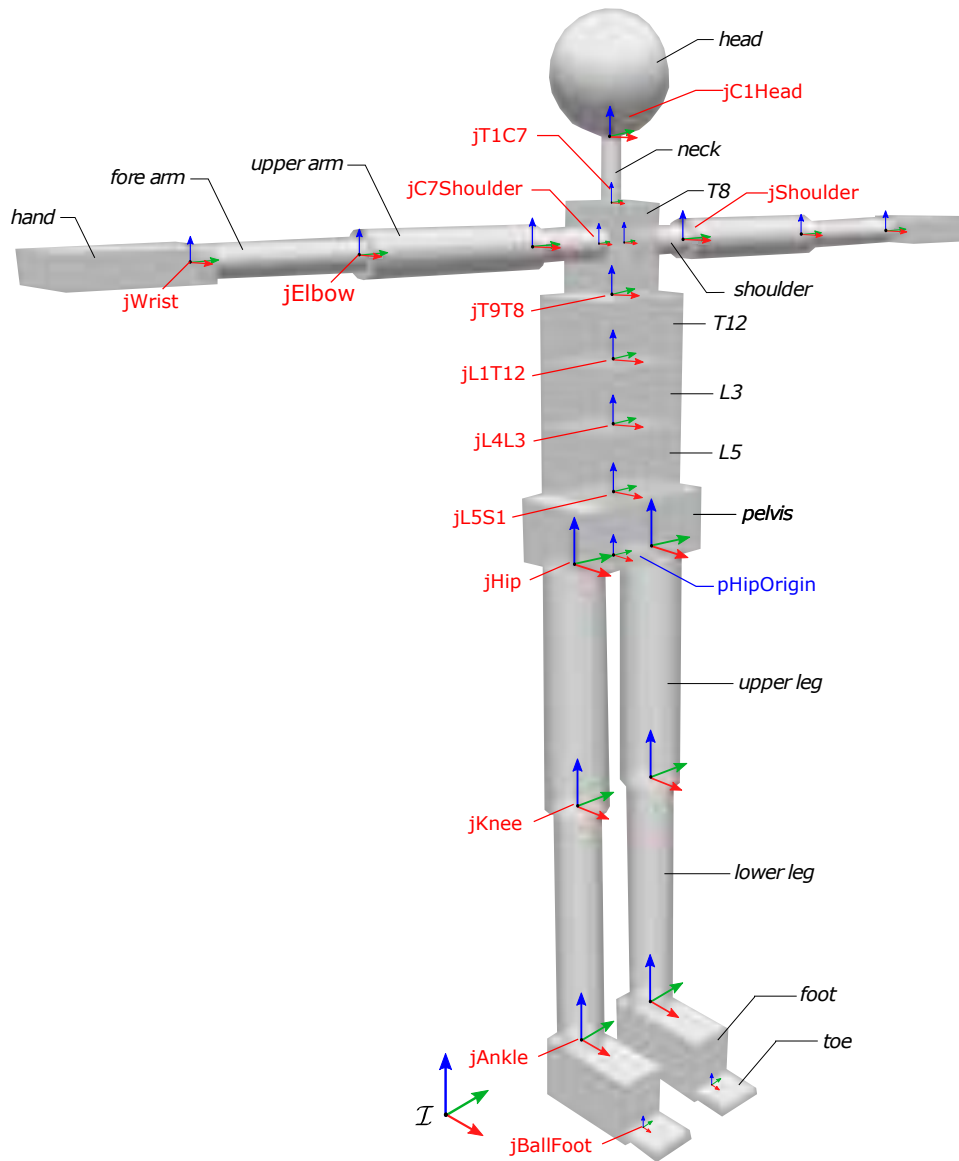


Fig. B.2 URDF human body model with labels for links and joints. The Gazebo simulator is used for the model visualization ( $DUMMYMASS = 0.0001$  kg,  $DUMMYININERTIA = 0.0003$  kg m<sup>2</sup>).

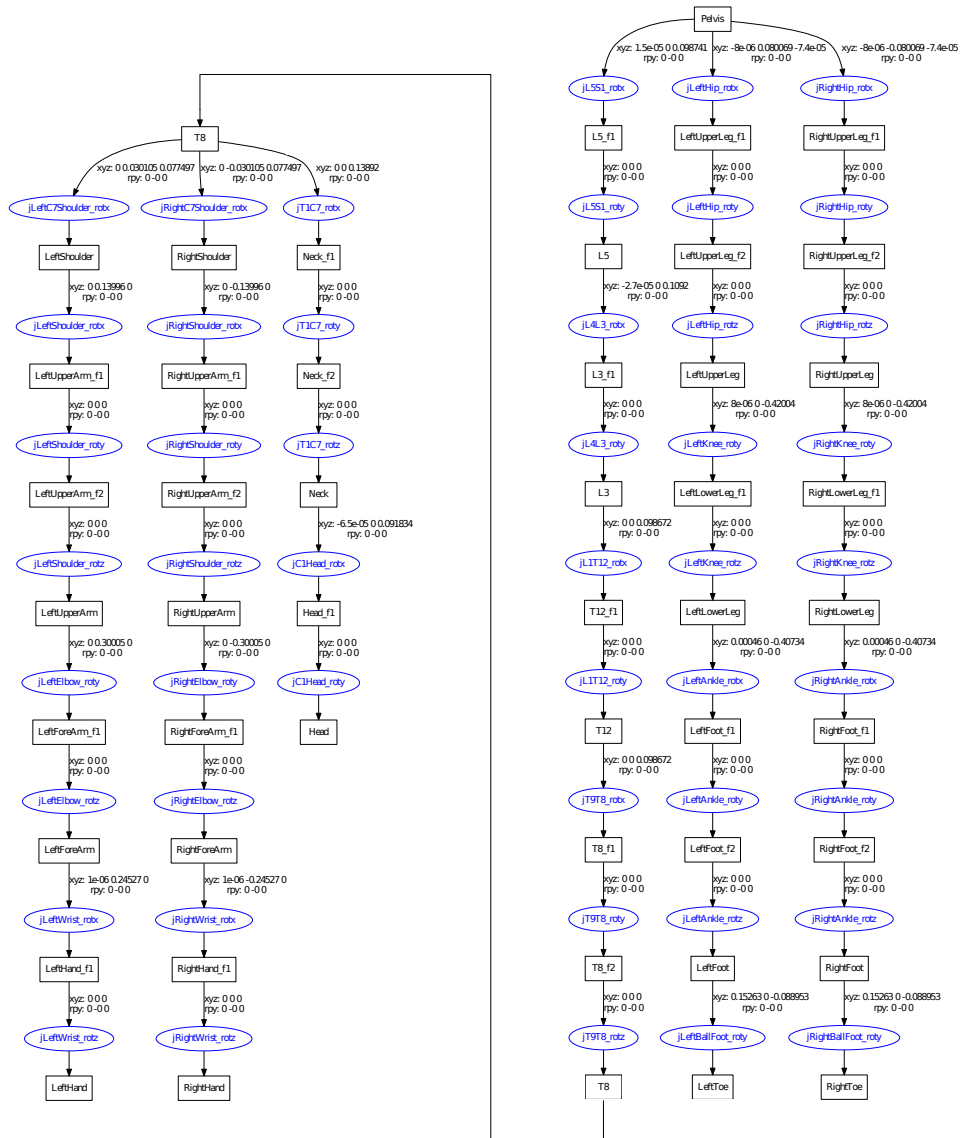


Fig. B.3 Graphviz diagram visualization [ROS] of the URDF model hierarchy. Black boxes are the links, blue shapes are the joints.

## B.1 The Non-Standard URDF Extension

The URDF semantics does not support officially the possibility to insert sensor information on the model. In this thesis it is used a non-standard extension to the format where each sensor is encoded in the XML file as a new type of element `sensor`. For loading sensor information, the name and type of sensor, the link to which each sensor is attached and its position in the link have to be specified. Hereafter an example of XML tag for the sensor attached on the `RightLowerLeg`.

```
1 <!-- Gyroscope-->
2 <sensor name="RightLowerLeg_gyro" type="gyroscope">
3   <parent link="RightLowerLeg"/>
4   <!-- sensor pose w.r.t. RightLowerLeg -->
5   <origin xyz="RIGHTLOWERLEG_S_POS" rpy="RIGHTLOWERLEG_S_RPY"/>
6 </sensor>
7 <!--Accelerometer -->
8 <sensor name="RightLowerLeg_accelerometer" type="accelerometer">
9   <parent link="RightLowerLeg"/>
10  <!-- sensor pose w.r.t. RightLowerLeg -->
11  <origin xyz="RIGHTLOWERLEG_S_POS" rpy="RIGHTLOWERLEG_S_RPY"/>
12 </sensor>
```

The sensors (IMUs) attached to the human body links are shown in the following XML list, extracted from the URDF template:

```
1 <!--SENSORS-->
2   <!-- Sensor 1-->
3   <sensor name="Pelvis_gyro" type="gyroscope">
4   <sensor name="Pelvis_accelerometer" type="accelerometer">
5   <!-- Sensor 2-->
6   <sensor name="T8_gyro" type="gyroscope">
7   <sensor name="T8_accelerometer" type="accelerometer">
8   <!-- Sensor 3-->
9   <sensor name="Head_gyro" type="gyroscope">
10  <sensor name="Head_accelerometer" type="accelerometer">
11  <!-- Sensor 4-->
12  <sensor name="RightShoulder_gyro" type="gyroscope">
13  <sensor name="RightShoulder_accelerometer" type="accelerometer">
14  <!-- Sensor 5-->
15  <sensor name="RightUpperArm_gyro" type="gyroscope">
16  <sensor name="RightUpperArm_accelerometer" type="accelerometer">
17  <!-- Sensor 6-->
18  <sensor name="RightForeArm_gyro" type="gyroscope">
19  <sensor name="RightForeArm_accelerometer" type="accelerometer">
20  <!-- Sensor 7-->
21  <sensor name="RightHand_gyro" type="gyroscope">
```

```
22 <sensor name="RightHand_accelerometer" type="accelerometer">
23 <!-- Sensor 8-->
24 <sensor name="LeftShoulder_gyro" type="gyroscope">
25 <sensor name="LeftShoulder_accelerometer" type="accelerometer">
26 <!-- Sensor 9-->
27 <sensor name="LeftUpperArm_gyro" type="gyroscope">
28 <sensor name="LeftUpperArm_accelerometer" type="accelerometer">
29 <!-- Sensor 10-->
30 <sensor name="LeftForeArm_gyro" type="gyroscope">
31 <sensor name="LeftForeArm_accelerometer" type="accelerometer">
32 <!-- Sensor 11-->
33 <sensor name="LeftHand_gyro" type="gyroscope">
34 <sensor name="LeftHand_accelerometer" type="accelerometer">
35 <!-- Sensor 12-->
36 <sensor name="RightUpperLeg_gyro" type="gyroscope">
37 <sensor name="RightUpperLeg_accelerometer" type="accelerometer">
38 <!-- Sensor 13-->
39 <sensor name="RightLowerLeg_gyro" type="gyroscope">
40 <sensor name="RightLowerLeg_accelerometer" type="accelerometer">
41 <!-- Sensor 14-->
42 <sensor name="RightFoot_gyro" type="gyroscope">
43 <sensor name="RightFoot_accelerometer" type="accelerometer">
44 <!-- Sensor 15-->
45 <sensor name="LeftUpperLeg_gyro" type="gyroscope">
46 <sensor name="LeftUpperLeg_accelerometer" type="accelerometer">
47 <!-- Sensor 16-->
48 <sensor name="LeftLowerLeg_gyro" type="gyroscope">
49 <sensor name="LeftLowerLeg_accelerometer" type="accelerometer">
50 <!-- Sensor 17-->
51 <sensor name="LeftFoot_gyro" type="gyroscope">
52 <sensor name="LeftFoot_accelerometer" type="accelerometer">
```



## Appendix C

# Offline Inverse Kinematics Computation

Within the context of the *offline* algorithm validation (see Chapter 5), the Inverse Kinematics (IK) for the human model has been performed by means of the OpenSim IK toolbox [OpenSim], through an OpenSim API for Matlab. Figure C.1 shows the elements involved in the IK computation.

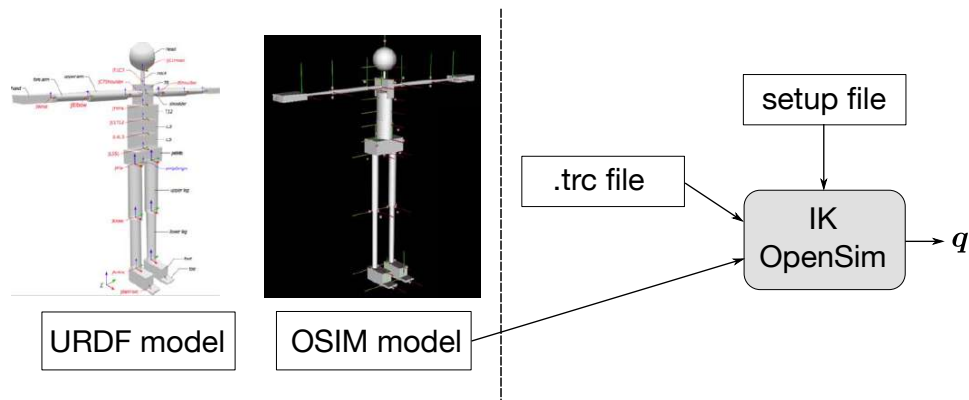
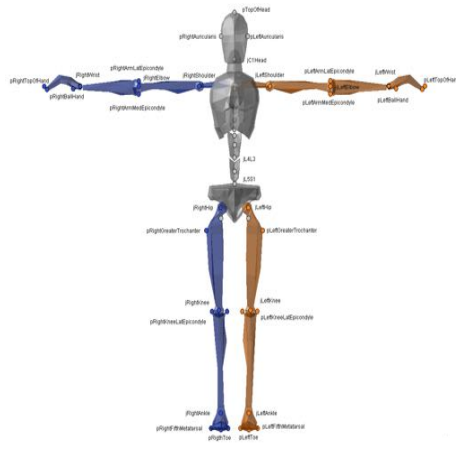


Fig. C.1 Pipeline for the OpenSim IK.

The primary OpenSim IK toolbox inputs are the following files.

- A trajectories (.trc) file containing the experimental marker trial trajectories of the human subject acquired from a motion capture system. In our specific case, trajectories of 64 anatomical bony landmarks have been provided by Xsens, Figure C.2.



1	pHipOrigin	33	pRightTopOfHand
2	pRightASI	34	pRightPinky
3	pLeftASI	35	pRightBallOfHand
4	pRightCSI	36	pLeftTopOfHand
5	pLeftCSI	37	pLeftPinky
6	pRightIschialTub	38	pLeftBallOfHand
7	pLeftIschialTub	39	pRightGreaterTrochanter
8	pSacrum	40	pRightKneeLatEpicondyle
9	pL5SpinalProcess	41	pRightKneeMedEpicondyle
10	pL3SpinalProcess	42	pRightMiddleKneeCap (or pRightPatella)
11	pT12SpinalProcess	43	pLeftGreaterTrochanter
12	pPX	44	pLeftKneeLatEpicondyle
13	pIJ	45	pLeftKneeMedEpicondyle
14	pT4SpinalProcess	46	pLeftMiddleKneeCap (or pLeftPatella)
15	pT8SpinalProcess	47	pRightLatMalleolus
16	pC7SpinalProcess	48	pRightMedMalleolus
17	pTopOfHead	49	pRightTibialTub
18	pRightAuricularis	50	pLeftLatMalleolus
19	pLeftAuricularis	51	pLeftMedMalleolus
20	pBackOfHead	52	pLeftTibialTub
21	pRightAcromion	53	pRightHeelFoot
22	pLeftAcromion	54	pRightFirstMetatarsal
23	pRightArmLatEpicondyle	55	pRightFifthMetatarsal
24	pRightArmMedEpicondyle	56	pRightPivotFoot
25	pLeftArmLatEpicondyle	57	pRightHeelCenter
26	pLeftArmMedEpicondyle	58	pRightToe
27	pRightUlnarStyloid	59	pLeftHeelFoot
28	pRightRadialStyloid	60	pLeftFirstMetatarsal
29	pRightOlecranon	61	pLeftFifthMetatarsal
30	pLeftUlnarStyloid	62	pLeftPivotFoot
31	pLeftRadialStyloid	63	pLeftHeelCenter
32	pLeftOlecranon	64	pLeftToe

Fig. C.2 Xsens anatomical bony landmarks.  
[Source: Xsens, MVN User Manual, 2005.]

- The subject-specific OSIM model created by *i*) matching the same structure of the URDF model (see Appendix B) and *ii*) matching the position of the 64 anatomical markers (provided by Xsens) as listed in Figure C.2. Here following the markers section in a OSIM model.

```

1 <!--OSIM MODEL 48 DoFs-->
2 </OpenSimDocument>
3 <Model name="XSensStyleModel">
4 <!--Markers in the model.-->
5 <MarkerSet>
6 <!--Pelvis markers-->
7 <Marker name="pHipOrigin"></Marker>
8 <Marker name="pRightASI"></Marker>
9 <Marker name="pLeftASI"></Marker>
10 <Marker name="pRightCSI"></Marker>
11 <Marker name="pLeftCSI"></Marker>
12 <Marker name="pRightIschialTub"></Marker>
13 <Marker name="pLeftIschialTub"></Marker>
14 <Marker name="pSacrum"></Marker>
15 <!--L5 markers-->
16 <Marker name="pL5SpinalProcess"></Marker>
17 <!--L3 markers-->
18 <Marker name="pL3SpinalProcess"></Marker>
19 <!--T12 markers-->
20 <Marker name="pT12SpinalProcess"></Marker>
21 <!--T8 markers-->
22 <Marker name="pPX"></Marker>
23 <Marker name="pIJ"></Marker>

```

```

24 <Marker name="pT4SpinalProcess"></Marker>
25 <Marker name="pT8SpinalProcess"></Marker>
26 <Marker name="pC7SpinalProcess"></Marker>
27 <!--Head markers-->
28 <Marker name="pTopOfHead"></Marker>
29 <Marker name="pRightAuricularis"></Marker>
30 <Marker name="pLeftAuricularis"></Marker>
31 <Marker name="pBackOfHead"></Marker>
32 <!--RightShoulder markers-->
33 <Marker name="pRightAcromion"></Marker>
34 <!--RightUpperArm markers-->
35 <Marker name="pRightArmLatEpicondyle"></Marker>
36 <Marker name="pRightArmMedEpicondyle"></Marker>
37 <!--RightForeArm markers-->
38 <Marker name="pRightUlnarStyloid"></Marker>
39 <Marker name="pRightRadialStyloid"></Marker>
40 <Marker name="pRightOlecranon"></Marker>
41 <!--RightHand markers-->
42 <Marker name="pRightTopOfHand"></Marker>
43 <Marker name="pRightPinky"></Marker>
44 <Marker name="pRightBallHand"></Marker>
45 <!--LeftShoulder markers-->
46 <Marker name="pLeftAcromion"></Marker>
47 <!--LeftUpperArm markers-->
48 <Marker name="pLeftArmLatEpicondyle"></Marker>
49 <Marker name="pLeftArmMedEpicondyle"></Marker>
50 <!--LeftForeArm markers-->
51 <Marker name="pLeftUlnarStyloid"></Marker>
52 <Marker name="pLeftRadialStyloid"></Marker>
53 <Marker name="pLeftOlecranon"></Marker>
54 <!--LeftHand markers-->
55 <Marker name="pLeftTopOfHand"></Marker>
56 <Marker name="pLeftPinky"></Marker>
57 <Marker name="pLeftBallHand"></Marker>
58 <!--RightUpperLeg markers-->
59 <Marker name="pRightGreaterTrochanter"></Marker>
60 <Marker name="pRightPatella"></Marker>
61 <!--RightLowerLeg markers-->
62 <Marker name="pRightKneeLatEpicondyle"></Marker>
63 <Marker name="pRightKneeMedEpicondyle"></Marker>
64 <Marker name="pRightLatMalleolus"></Marker>
65 <Marker name="pRightMedMalleolus"></Marker>
66 <Marker name="pRightTibialTub"></Marker>
67 <!--RightFoot markers-->
68 <Marker name="pRightHeelFoot"></Marker>
69 <Marker name="pRightFirstMetatarsal"></Marker>
70 <Marker name="pRightFifthMetatarsal"></Marker>
71 <Marker name="pRightPivotFoot"></Marker>
72 <Marker name="pRightHeelCenter"></Marker>

```

```

73     <!--RightToe markers-->
74     <Marker name="pRightToe"></Marker>
75     <!--LeftUpperLeg markers-->
76     <Marker name="pLeftGreaterTrochanter"></Marker>
77     <Marker name="pLeftPatella"></Marker>
78     <!--LeftLowerLeg markers-->
79     <Marker name="pLeftKneeLatEpicondyle"></Marker>
80     <Marker name="pLeftKneeMedEpicondyle"></Marker>
81     <Marker name="pLeftLatMalleolus"></Marker>
82     <Marker name="pLeftMedMalleolus"></Marker>
83     <Marker name="pLeftTibialTub"></Marker>
84     <!--LeftFoot markers-->
85     <Marker name="pLeftHeelFoot"></Marker>
86     <Marker name="pLeftFirstMetatarsal"></Marker>
87     <Marker name="pLeftFifthMetatarsal"></Marker>
88     <Marker name="pLeftPivotFoot"></Marker>
89     <Marker name="pLeftHeelCenter"></Marker>
90     <!--LeftToe markers-->
91     <Marker name="pLeftToe"></Marker>
92 </MarkerSet>
93 </Model>
94 </OpenSimDocument>

```

- A setup XML file containing all the setting information for the IK computation (including the markers weight, the time range, the acceptable accuracy).

The IK tool solves a weighted least-squares problem by means of a general quadratic programming solver. The solver minimizes, for each timestamp in the task range, the difference between the position of the markers on the model and the experimental data. The Matlab API yields to

```

import org.opensim.modeling.* %
osimModel = Model(filenameOsimModel);
osimModel.initSystem();
ikTool = InverseKinematicsTool(setupFile);
ikTool.setModel(osimModel);
ikTool.setMarkerDataFileName(filenameTrc);
ikTool.setOutputMotionFileName(outputMotionFilename);
ikTool.run();

```

The output of the system is a motion (.mot) file (i.e., outputMotionFilename) containing the joint angles  $q$  of the model.

## Appendix D

# Simultaneous Human Dynamics and State Estimation

Consider the system (4.22) in Chapter 4:

$$\begin{bmatrix} \mathbf{Y}(\mathbf{q}, \dot{\mathbf{q}}) \\ \mathbf{D}(\mathbf{q}, \dot{\mathbf{q}}) \end{bmatrix} \mathbf{d} + \begin{bmatrix} \mathbf{b}_Y(\mathbf{q}, \dot{\mathbf{q}}) \\ \mathbf{b}_D(\mathbf{q}, \dot{\mathbf{q}}) \end{bmatrix} = \begin{bmatrix} \mathbf{y} \\ \mathbf{0} \end{bmatrix}, \quad \text{rank} \left( \begin{bmatrix} \mathbf{Y}(\mathbf{q}, \dot{\mathbf{q}}) \\ \mathbf{D}(\mathbf{q}, \dot{\mathbf{q}}) \end{bmatrix} \right) = d, \quad (\text{D.1})$$

whose MAP Gaussian solution is represented by Equations (4.35), such that

$$\Sigma_{d|y} = \left( \bar{\Sigma}_D^{-1} + \mathbf{Y}^\top \Sigma_{y|d}^{-1} \mathbf{Y} \right)^{-1}, \quad (\text{D.2a})$$

$$\mathbf{d} = \Sigma_{d|y} \left[ \mathbf{Y}^\top \Sigma_{y|d}^{-1} (\mathbf{y} - \mathbf{b}_Y) + \bar{\Sigma}_D^{-1} \bar{\boldsymbol{\mu}}_D \right]. \quad (\text{D.2b})$$

The solution (D.2b) is obtained by assuming the  $\mathbf{q}$  and  $\dot{\mathbf{q}}$  without uncertainty. It is well-known that in practical acquisitions, the state is affected by statistical noise and other inaccuracies. Thus, this Appendix deals with the way to include the state  $\mathbf{x} = (\mathbf{q}, \dot{\mathbf{q}})$  in the estimation problem. This is not a trivial task and complications arise from the fact that (D.1) is not linear in  $\mathbf{x}$ . If  $\bar{\mathbf{d}}$  and  $\bar{\mathbf{x}}$  are the mean on the vector  $\mathbf{d}$  and  $\mathbf{x}$ , respectively, thus the first order approximation around these quantities of (D.1) is such that

$$\begin{bmatrix} \mathbf{b}_Y(\bar{\mathbf{x}}) \\ \mathbf{b}_D(\bar{\mathbf{x}}) \end{bmatrix} + \begin{bmatrix} \mathbf{Y}(\bar{\mathbf{x}}) \\ \mathbf{D}(\bar{\mathbf{x}}) \end{bmatrix} \mathbf{d} + \begin{bmatrix} \partial \mathbf{b}_Y(\bar{\mathbf{d}}, \bar{\mathbf{x}}) \\ \partial \mathbf{b}_D(\bar{\mathbf{d}}, \bar{\mathbf{x}}) \end{bmatrix} (\mathbf{x} - \bar{\mathbf{x}}) = \begin{bmatrix} \mathbf{y} \\ \mathbf{0} \end{bmatrix}, \quad (\text{D.3})$$

where

$$\mathbf{b}_Y(\bar{\mathbf{x}}) = \left. \frac{\partial}{\partial \mathbf{x}} \mathbf{b}_Y(\mathbf{x}) \right|_{\mathbf{x}=\bar{\mathbf{x}}}, \quad (\text{D.4})$$

$$\mathbf{b}_D(\bar{\mathbf{x}}) = \left. \frac{\partial}{\partial \mathbf{x}} \mathbf{b}_D(\mathbf{x}) \right|_{\mathbf{x}=\bar{\mathbf{x}}}, \quad (\text{D.5})$$

$$\mathbf{Y}(\bar{\mathbf{x}}) = \left. \frac{\partial}{\partial \mathbf{x}} \mathbf{Y}(\mathbf{x}) \right|_{\mathbf{x}=\bar{\mathbf{x}}}, \quad (\text{D.6})$$

$$\mathbf{D}(\bar{\mathbf{x}}) = \left. \frac{\partial}{\partial \mathbf{x}} \mathbf{D}(\mathbf{x}) \right|_{\mathbf{x}=\bar{\mathbf{x}}}, \quad (\text{D.7})$$

$$\partial \mathbf{b}_Y(\bar{\mathbf{d}}, \bar{\mathbf{x}}) = \left. \frac{\partial}{\partial \mathbf{x}} [\mathbf{Y}(\mathbf{x}) \bar{\mathbf{d}} + \mathbf{b}_Y(\mathbf{x})] \right|_{\mathbf{x}=\bar{\mathbf{x}}}, \quad (\text{D.8})$$

$$\partial \mathbf{b}_D(\bar{\mathbf{d}}, \bar{\mathbf{x}}) = \left. \frac{\partial}{\partial \mathbf{x}} [\mathbf{D}(\mathbf{x}) \bar{\mathbf{d}} + \mathbf{b}_D(\mathbf{x})] \right|_{\mathbf{x}=\bar{\mathbf{x}}}. \quad (\text{D.9})$$

The system (D.3) could be rearranged in the same structure of system (D.1):

$$\begin{bmatrix} \mathbf{Y}(\bar{\mathbf{x}}) & \partial \mathbf{b}_Y(\bar{\mathbf{d}}, \bar{\mathbf{x}}) \\ \mathbf{D}(\bar{\mathbf{x}}) & \partial \mathbf{b}_D(\bar{\mathbf{d}}, \bar{\mathbf{x}}) \end{bmatrix} \begin{bmatrix} \bar{\mathbf{d}} \\ \mathbf{x} \end{bmatrix} + \begin{bmatrix} \mathbf{b}_Y(\bar{\mathbf{x}}) - \partial \mathbf{b}_Y(\bar{\mathbf{d}}, \bar{\mathbf{x}}) \bar{\mathbf{x}} \\ \mathbf{b}_D(\bar{\mathbf{x}}) - \partial \mathbf{b}_D(\bar{\mathbf{d}}, \bar{\mathbf{x}}) \bar{\mathbf{x}} \end{bmatrix} = \begin{bmatrix} \mathbf{y} \\ \mathbf{0} \end{bmatrix}. \quad (\text{D.10})$$

The system (D.10) becomes the new system to be solved in the MAP domain. The mean and the covariance of the PDF  $p(\bar{\mathbf{d}}, \mathbf{x}|\mathbf{y})$  can be obtained as in (4.35) by replacing

$$\begin{aligned} \mathbf{Y}(\mathbf{q}, \dot{\mathbf{q}}) &\leftrightarrow [\mathbf{Y}(\bar{\mathbf{x}}) \quad \partial \mathbf{b}_Y(\bar{\mathbf{d}}, \bar{\mathbf{x}})], \\ \mathbf{D}(\mathbf{q}, \dot{\mathbf{q}}) &\leftrightarrow [\mathbf{D}(\bar{\mathbf{x}}) \quad \partial \mathbf{b}_D(\bar{\mathbf{d}}, \bar{\mathbf{x}})], \\ \mathbf{b}_Y(\mathbf{q}, \dot{\mathbf{q}}) &\leftrightarrow [\mathbf{b}_Y(\bar{\mathbf{x}}) - \partial \mathbf{b}_Y(\bar{\mathbf{d}}, \bar{\mathbf{x}}) \bar{\mathbf{x}}], \\ \mathbf{b}_D(\mathbf{q}, \dot{\mathbf{q}}) &\leftrightarrow [\mathbf{b}_D(\bar{\mathbf{x}}) - \partial \mathbf{b}_D(\bar{\mathbf{d}}, \bar{\mathbf{x}}) \bar{\mathbf{x}}], \\ \boldsymbol{\mu}_d &\leftrightarrow [\boldsymbol{\mu}_d \quad \boldsymbol{\mu}_x]^T, \\ \boldsymbol{\Sigma}_d &\leftrightarrow \begin{bmatrix} \boldsymbol{\Sigma}_d & \mathbf{0} \\ \mathbf{0} & \boldsymbol{\Sigma}_x \end{bmatrix}, \end{aligned}$$

being  $\mathbf{x} \sim \mathcal{N}(\boldsymbol{\mu}_x, \boldsymbol{\Sigma}_x)$  the Gaussian distribution for the state  $\mathbf{x}$ . Details on how to compute (D.8) and (D.9) derivatives are shown in Section 5A of [Nori et al., 2015].





# Bibliography

- H. Ben Amor, G. Neumann, S. Kamthe, O. Kroemer, and J. Peters. Interaction primitives for human-robot cooperation tasks. In *2014 IEEE International Conference on Robotics and Automation (ICRA)*, pages 2831–2837, May 2014.
- An.Dy. Advancing anticipatory behaviors in dyadic human-robot collaboration, h2020 project. Jan 2017. URL <http://andy-project.eu>.
- Vincent Bonnet, Claudia Mazzà, Philippe Fraise, and Aurelio Cappelletti. Real-time estimate of body kinematics during a planar squat task using a single inertial measurement unit. *IEEE Trans. Biomed. Engineering*, 60:1920–1926, 2013.
- Júlia Borràs, Christian Mandery, and Tamim Asfour. A whole-body support pose taxonomy for multi-contact humanoid robot motions. *Science Robotics*, 2(13), 2017.
- M. Do N. Vahrenkamp C. Mandery, O. Terlemez and T. Asfour. The kit whole-body human motion database. In *International Conference on Advanced Robotics (ICAR)*, pages 329–336, July 2015.
- Violaine Cahouët, Martin Luc, and Amarantini David. Static optimal estimation of joint accelerations for inverse dynamics problem solution. *Journal of Biomechanics*, 35(11):1507–1513, 11 2002. doi: [http://dx.doi.org/10.1016/S0021-9290\(02\)00176-8](http://dx.doi.org/10.1016/S0021-9290(02)00176-8). URL <http://www.sciencedirect.com/science/article/pii/S0021929002001768>.
- Aurelio Cappelletti, Tommaso Leo, and Antonio Pedotti. A general computing method for the analysis of human locomotion. *Journal of Biomechanics*, 8(5): 307–320, 2017/11/10 1975. doi: [10.1016/0021-9290\(75\)90083-4](https://doi.org/10.1016/0021-9290(75)90083-4). URL [http://dx.doi.org/10.1016/0021-9290\(75\)90083-4](http://dx.doi.org/10.1016/0021-9290(75)90083-4).
- John H. Challis and David G. Kerwin. Quantification of the uncertainties in resultant joint moments computed in a dynamic activity. *Journal of Sports Sciences*, 14(3):219–231, 1996. doi: [10.1080/02640419608727706](https://doi.org/10.1080/02640419608727706). URL <http://dx.doi.org/10.1080/02640419608727706>. PMID: 8809714.

- J. Chen, A. Bandoni, and J.A. Romagnoli. Robust estimation of measurement error variance/covariance from process sampling data. *Computers and Chemical Engineering*, 21(6):593 – 600, 1997. ISSN 0098-1354. doi: [http://dx.doi.org/10.1016/S0098-1354\(96\)00295-5](http://dx.doi.org/10.1016/S0098-1354(96)00295-5). URL <http://www.sciencedirect.com/science/article/pii/S0098135496002955>.
- S. L. Delp, F. C. Anderson, A. S. Arnold, P. Loan, A. Habib, C. T. John, E. Guendelman, and D. G. Thelen. Opensim: Open-source software to create and analyze dynamic simulations of movement. *IEEE Transactions on Biomedical Engineering*, Nov 2007.
- Emel Demircan, Dana Kulic, Denny Oetomo, and Mitsuhiro Hayashibe. Human movement understanding [tc spotlight]. *IEEE Robot. Automat. Mag.*, 22:22–24, 2015.
- J. Denavit and R. S. Hartenberg. A kinematic notation for lower-pair mechanisms based on matrices. *Trans. of the ASME. Journal of Applied Mechanics*, 22:215–221, 1955.
- R Drillis, R Contini, and M Bluestein. Body segment parameters; a survey of measurement techniques. *Artificial limbs*, 25, 1964. URL [http://www.oandplibrary.org/al/pdf/1964\\_01\\_044.pdf](http://www.oandplibrary.org/al/pdf/1964_01_044.pdf).
- Włodzimierz Stefan Erdmann. Geometry and inertia of the human body - review of research. *Acta of Bioengineering and biomechanics*, 1(1), 1999. URL <http://www.actabio.pwr.wroc.pl/Vol1No1/3.pdf>.
- Roy Featherstone. *Rigid Body Dynamics Algorithms*. Springer-Verlag New York, Inc., Secaucus, NJ, USA, 2007. ISBN 0387743146.
- T Flash and N Hogan. The coordination of arm movements: an experimentally confirmed mathematical model. *Journal of Neuroscience*, 5(7):1688–1703, 1985.
- J. A. Gallego, E. Rocon, J. Ibáñez, J. L. Dideriksen, A. D. Koutsou, R. Paradiso, M. B. Popovic, J. M. Belda-Lois, F. Gianfelici, D. Farina, D. B. Popovic, M. Manto, T. D’Alessio, and J. L. Pons. A soft wearable robot for tremor assessment and suppression. In *Robotics and Automation (ICRA), 2011 IEEE International Conference on*, pages 2249–2254. IEEE, May 2011.
- Gazebo. Simulator. URL <http://gazebo.org>.
- Gene H. Golub and Charles F. Van Loan. *Matrix Computations (3rd Ed.)*. Johns Hopkins University Press, Baltimore, MD, USA, 1996. ISBN 0-8018-5414-8.
- Michael A. Goodrich and Alan C. Schultz. Human-robot interaction: A survey. *Found. Trends Hum.-Comput. Interact.*, 1(3):203–275, January 2007. ISSN 1551-3955. doi: 10.1561/11000000005. URL <http://dx.doi.org/10.1561/11000000005>.

- G. Guerra-Filho and A. Biswas. The human motion database: A cognitive and parametric sampling of human motion. In *Face and Gesture 2011*, pages 103–110, March 2011.
- E. P. Hanavan. A mathematical model of human body. Technical report, Air force aerospace medical research lab Wright-Patterson AFB OH, 1964.
- H. Hatze. A mathematical model for the computational determination of parameter values of anthropomorphic segments. *Journal of Biomechanics*, 13(10):833–843, 1980. doi: [http://dx.doi.org/10.1016/0021-9290\(80\)90171-2](http://dx.doi.org/10.1016/0021-9290(80)90171-2). URL [http://dx.doi.org/10.1016/0021-9290\(80\)90171-2](http://dx.doi.org/10.1016/0021-9290(80)90171-2).
- HDE. Github repository for human dynamics estimation. 2017. URL <https://github.com/robotology/human-dynamics-estimation>.
- I. P. Herman. *Physics of the human body*, chapter Terminology, the standard human, and scaling. Springer, 2007.
- Vladimir Joukov, Vincent Bonnet, Michelle Karg, Gentiane Venture, and Dana Kulic. Rhythmic extended kalman filter for gait rehabilitation motion estimation and segmentation. *IEEE transactions on neural systems and rehabilitation engineering : a publication of the IEEE Engineering in Medicine and Biology Society*, 2017.
- Hyeong Ryeol Kam, Sung-Ho Lee, Taejung Park, and Chang-Hun Kim. Rviz: a toolkit for real domain data visualization. *Telecommunication Systems*, 60(2):337–345, 2015. doi: 10.1007/s11235-015-0034-5. URL <http://dx.doi.org/10.1007/s11235-015-0034-5>.
- J.Y. Keller, M. Zasadzinski, and M. Darouach. Analytical estimator of measurement error variances in data reconciliation. *Computers and Chemical Engineering*, 16(3):185 – 188, 1992. ISSN 0098-1354. doi: [http://dx.doi.org/10.1016/0098-1354\(92\)85005-S](http://dx.doi.org/10.1016/0098-1354(92)85005-S). URL <http://www.sciencedirect.com/science/article/pii/009813549285005S>.
- Kinect. Microsoft kinect. URL <https://developer.microsoft.com/en-us/windows/kinect>.
- H. Kuehne, H. Jhuang, E. Garrote, T. Poggio, and T. Serre. Hmdb: A large video database for human motion recognition. In *2011 International Conference on Computer Vision*, pages 2556–2563, Nov 2011.
- S. B. Kulathinal, Kari Kuulasmaa, and Dario Gasbarra. Estimation of an errors-in-variables regression model when the variances of the measurement errors vary between the observations. *Statistics in Medicine*, 21(8):1089–1101, 2002.
- A.D. Kuo. A least-squares estimation approach to improving the precision of inverse dynamics computations. *J. Biomech. Eng.*, 120:pp. 148–159, 1998.

- Claudia Latella, Naveen Kuppaswamy, Francesco Romano, Silvio Traversaro, and Francesco Nori. Whole-body human inverse dynamics with distributed micro-accelerometers, gyros and force sensing. *Sensors*, 16(5):727, 2016. ISSN 1424-8220. doi: 10.3390/s16050727. URL <http://www.mdpi.com/1424-8220/16/5/727>.
- Tine Lefebvre, Herman Bruyninckx, and Joris De Schutter. Kalman filters for non-linear systems: a comparison of performance. *International Journal of Control*, 77(7):639–653, 2004. doi: 10.1080/00207170410001704998. URL <https://doi.org/10.1080/00207170410001704998>.
- Jonathan F S Lin and Dana Kulić. Human pose recovery using wireless inertial measurement units. *Physiological Measurement*, 33(12):2099, 2012. URL <http://stacks.iop.org/0967-3334/33/i=12/a=2099>.
- Y. Maeda, T. Hara, and T. Arai. Human-robot cooperative manipulation with motion estimation. In *Intelligent Robots and Systems, 2001. Proceedings. 2001 IEEE/RSJ International Conference on*, volume 4, pages 2240–2245, 2001.
- C. Mandery, Ö. Terlemez, M. Do, N. Vahrenkamp, and T. Asfour. Unifying representations and large-scale whole-body motion databases for studying human motion. *IEEE Transactions on Robotics*, 32(4):796–809, Aug 2016.
- MAPest. Github repository for human map offline estimation. 2016. URL <https://github.com/claudia-lat/MAPest>.
- Luis A. Mateos, Jesús Ortiz, Stefano Toxiri, Jorge Fernandez, Jawad Masood, and Darwin G. Caldwell. Exoshoe: A sensory system to measure foot pressure in industrial exoskeleton. In *BioRob*, pages 99–105. IEEE, 2016.
- Yiğit Mengüç, Yong-Lae Park, Ernesto Martinez-Villalpando, Patrick Aubin, Miriam Zisook, Leia Stirling, Robert J Wood, and Conor J Walsh. Soft wearable motion sensing suit for lower limb biomechanics measurements. In *Robotics and Automation (ICRA), 2013 IEEE International Conference on*, pages 5309–5316. IEEE, May 2013.
- Yiğit Mengüç, Yong-Lae Park, Hao Pei, Daniel Vogt, Patrick M Aubin, Ethan Winchell, Lowell Fluke, Leia Stirling, Robert J Wood, and Conor J Walsh. Wearable soft sensing suit for human gait measurement. *International Journal of Robotics Research*, 2014.
- Giorgio Metta, Paul Fitzpatrick, and Lorenzo Natale. Yarp: Yet another robot platform. *International Journal of Advanced Robotic Systems*, 3(1):8, 2006.
- Giorgio Metta, Lorenzo Natale, Francesco Nori, Giulio Sandini, David Vernon, Luciano Fadiga, Claes von Hofsten, Kerstin Rosander, Manuel Lopes, José Santos-Victor, Alexandre Bernardino, and Luis Montesano. The icub humanoid

robot: An open-systems platform for research in cognitive development. *Neural Networks*, 23(8–9):1125 – 1134, 2010. ISSN 0893-6080. doi: <http://dx.doi.org/10.1016/j.neunet.2010.08.010>. URL <http://www.sciencedirect.com/science/article/pii/S0893608010001619>. Social Cognition: From Babies to Robots.

S. Miossec and A. Kheddar. Human motion in cooperative tasks: Moving object case study. In *Robotics and Biomimetics, 2008. ROBIO 2008. IEEE International Conference on*, pages 1509–1514, Feb 2009.

Moticon. Foot dynamics. URL <http://www.moticon.de>.

MotionAnalysis. URL <https://www.motionanalysis.com>.

Noraxon. URL <https://www.noraxon.com>.

F. Nori, N. Kuppaswamy, and S. Traversaro. Simultaneous state and dynamics estimation in articulated structures. In *Intelligent Robots and Systems (IROS), 2015 IEEE/RSJ International Conference on*, pages 3380–3386, Sept. 2015.

Francesco Nori, Silvio Traversaro, Jorhabib Eljaik, Francesco Romano, Andrea Del Prete, and Daniele Pucci. icub whole-body control through force regulation on rigid non-coplanar contacts. *Frontiers in Robotics and AI*, 2015b.

R. Nowak. Bayesian square error estimators. Lecture note, 2011.

OpenSim. URL <https://www.opensim.stanford.edu>.

Alan V. Oppenheim and George C. Verghese. Estimation with minimum mean square error. Lecture note, 2010.

A.V. Oppenheim, G.C. Verghese, and Pearson Education. *Signals, Systems and Inference, Global Edition*. Pearson Education, Limited, 2016. ISBN 9781292156200. URL [https://books.google.ca/books?id=vV1o\\_jwEACAAJ](https://books.google.ca/books?id=vV1o_jwEACAAJ).

R. Paradiso and D. De Rossi. Advances in textile technologies for unobtrusive monitoring of vital parameters and movements. In *Engineering in Medicine and Biology Society, 2006. EMBS '06. 28th Annual International Conference of the IEEE*, pages 392–395, Aug 2006.

K.B. Petersen and M.S. Pedersen. *The Matrix Cookbook*. Technical University of Denmark, November 2012.

Raziel Riemer and Elizabeth T. Hsiao-Wecksler. Improving joint torque calculations: Optimization-based inverse dynamics to reduce the effect of motion errors. *Journal of Biomechanics*, 41(7):1503 – 1509, 2008. ISSN 0021-9290. doi: <http://dx.doi.org/10.1016/j.jbiomech.2008.02.011>.

URL <http://www.sciencedirect.com/science/article/pii/S0021929008000699>.

T. Robert, P. Leborgne, M. Abid, V. Bonnet, G. Venture, and R. Dumas. Whole body segment inertia parameters estimation from movement and ground reaction forces: a feasibility study. *Computer Methods in Biomechanics and Biomedical Engineering*, 20(sup1):175–176, 2017. doi: 10.1080/10255842.2017.1382919. URL <https://doi.org/10.1080/10255842.2017.1382919>. PMID: 29088683.

Gordon Robertson, Graham Caldwell, Joseph Hamill, Gary Kamen, and Saunders Whittlesey. *Research Methods in Biomechanics-2nd Edition*. Human Kinetics, 2014.

William S. P. Robertson. A modern take on the theoretical modelling of inertial properties of a human body for biomechanical simulations. In *20th International Congress on Modelling and Simulation, Adelaide, Australia, 1–6 December 2013*, 2013. URL <https://www.mssanz.org.au/modsim2013/C4/robertson.pdf>.

Daniel Roetenberg, Henk Luinge, and Per Slycke. Xsens mvn: full 6dof human motion tracking using miniature inertial sensors. Technical report, Xsens Motion Technologies BV, 2009. URL <http://human.kyst.com.tw/upload/downloadfs46130703234558070.pdf>.

José A. Romagnoli and Mabel Cristina Sánchez. 10 estimation of measurement error variances from process data. 2(Supplement C):183 – 197, 1999. ISSN 1874-5970. doi: [https://doi.org/10.1016/S1874-5970\(00\)80025-9](https://doi.org/10.1016/S1874-5970(00)80025-9). URL <http://www.sciencedirect.com/science/article/pii/S1874597000800259>.

Francesco Romano, Gabriele Nava, Morteza Azad, Jernej Camernik, Stefano Daffarra, Oriane Dermay, Claudia Latella, Maria Lazzaroni, Ryan Lober, Marta Lorenzini, Daniele Pucci, Olivier Sigaud, Silvio Traversaro, Jan Babic, Serena Ivaldi, Michael Mistry, Vincent Padois, and Francesco Nori. The codyco project achievements and beyond: Towards human aware whole-body controllers for physical human robot interaction. *IEEE Robotics and Automation Letters*, 3:516–523, November 2017. doi: 10.1109/LRA.2017.2768126. URL <http://ieeexplore.ieee.org/document/8093992>.

ROS. Urdf tutorial. URL <http://wiki.ros.org/urdf/XML/model>.

Nicholas Rotella, Sean Mason, Stefan Schaal, and Ludovic Righetti. Inertial sensor-based humanoid joint state estimation. *CoRR*, abs/1602.05134, 2016.

RTbiomechanics. Github repository for real-time biomechanics. URL <https://github.com/RealTimeBiomechanics>.

- Abraham. Savitzky and M. J. E. Golay. Smoothing and differentiation of data by simplified least squares procedures. *Analytical Chemistry*, 36(8):1627–1639, 1964. doi: 10.1021/ac60214a047. URL <http://dx.doi.org/10.1021/ac60214a047>.
- Stefan Schaal, Auke Ijspeert, and Aude Billard. Computational approaches to motor learning by imitation. *Philosophical Transactions of the Royal Society B: Biological Sciences*, 358(1431):537–547, 03 2003. doi: 10.1098/rstb.2002.1258. URL <http://www.ncbi.nlm.nih.gov/pmc/articles/PMC1693137/>.
- H. Martin Schepers, H. F. J. M. Koopman, and Peter H. Veltink. Ambulatory assessment of ankle and foot dynamics. *IEEE Trans. Biomed. Engineering*, 54(5):895–902, 2007. URL <http://dx.doi.org/10.1109/TBME.2006.889769>.
- Ajay Seth, Michael Sherman, Peter Eastman, and Scott Delp. Minimal formulation of joint motion for biomechanisms. *Nonlinear dynamics*, 62(1-2):291–303, 2010.
- Bruno Siciliano and Oussama Khatib. *Springer Handbook of Robotics*. Springer-Verlag New York, Inc., 2007.
- Bruno Siciliano, Lorenzo Sciavicco, Luigi Villani, and Giuseppe Oriolo. *Robotics: Modelling, Planning and Control*. Springer Publishing Company, Incorporated, 1st edition, 2008. ISBN 1846286417, 9781846286414.
- Tekscan. URL <https://www.tekscan.com>.
- Ö. Terlemez, S. Ulbrich, C. Mandery, M. Do, N. Vahrenkamp, and T. Asfour. Master motor map (mmm) - framework and toolkit for capturing, representing, and reproducing human motion on humanoid robots. In *2014 IEEE-RAS International Conference on Humanoid Robots*, pages 894–901, Nov 2014.
- Antonie J. van den Bogert and Anne Su. A weighted least squares method for inverse dynamic analysis. *Computer Methods in Biomechanics and Biomedical Engineering*, 11(1):3–9, 2008. doi: 10.1080/10255840701550865. URL <http://dx.doi.org/10.1080/10255840701550865>. PMID: 17943488.
- Antonie J van den Bogert, Thomas Geijtenbeek, Oshri Even-Zohar, Frans Steenbrink, and Elizabeth C Hardin. A real-time system for biomechanical analysis of human movement and muscle function. *Medical and Biological Engineering and Computing*, 51(10):1069–1077, 2013. doi: 10.1007/s11517-013-1076-z. URL <http://www.ncbi.nlm.nih.gov/pmc/articles/PMC3751375/>.

G. Venture, K. Ayusawa, and Y. Nakamura. Real-time identification and visualization of human segment parameters. In *2009 Annual International Conference of the IEEE Engineering in Medicine and Biology Society*, pages 3983–3986, Sept 2009. doi: 10.1109/IEMBS.2009.5333620.

Vicon. Motion capture. URL <https://www.vicon.com>.

Xiaolin Wei and Jinxiang Chai. Videomocap: Modeling physically realistic human motion from monocular video sequences. In *ACM SIGGRAPH 2010 Papers, SIGGRAPH '10*, pages 42:1–42:10, New York, NY, USA, 2010. ACM. ISBN 978-1-4503-0210-4. doi: 10.1145/1833349.1778779. URL <http://doi.acm.org/10.1145/1833349.1778779>.

David A. Winter. *Biomechanics and motor control of human movement*, chapter Anthropometry. Wiley, 1990.

J. Wojtuszczyk and O. von Stryk. Humod - a versatile and open database for the investigation, modeling and simulation of human motion dynamics on actuation level. In *2015 IEEE-RAS 15th International Conference on Humanoid Robots (Humanoids)*, pages 74–79, Nov 2015.

Xsens. Xsens technologies. URL <https://www.xsens.com>.

YARP. Yet another robot platform. URL <http://www.yarp.it>.

Peizhao Zhang, Kristin Siu, Jianjie Zhang, C. Karen Liu, and Jinxiang Chai. Leveraging depth cameras and wearable pressure sensors for full-body kinematics and dynamics capture. *ACM Trans. Graph.*, 33(6):221:1–221:14, November 2014. ISSN 0730-0301. doi: 10.1145/2661229.2661286. URL <http://doi.acm.org/10.1145/2661229.2661286>.

Z. Zhang. Microsoft kinect sensor and its effect. *IEEE MultiMedia*, 19(2):4–10, Feb 2012.

*The man who doesn't read good books has no advantage over the man who can't read them.*

Mark Twain